Development of electron tomography on liquid suspensions using environmental scanning electron microscopy

Juan Xiao

N°d'ordre NNT : 2017LYSEI050

THESE de DOCTORAT DE L'UNIVERSITE DE LYON
opérée au sein de
l'INSA LYON

Ecole Doctorale N° EDA034
(Ecole Doctorale Matériaux de Lyon)

Spécialité de doctorat : Matériaux

Soutenue publiquement/à huis clos le 13/06/2017, par :
(Juan XIAO)

Development of electron tomography on liquid suspensions using Environmental Scanning Electron Microscopy

Devant le jury composé de :

ERSEN Ovidiu	*Professeur des universités, Université de Strasbourg*	Rapporteur
PODOR Renaud	*Habilité à Diriger des Recherches, Institut de Chimie Séparative de Marcoule*	Rapporteur
PUTAUX Jean-Luc	*Directeur de Recherche, CNRS*	Examinateur
PECKYS Diana	*Chercheur, Universität des Saariandes*	Examinateur
MASENELLI-VARLOT Karine	*Professeur des Universités INSA-LYON*	Directrice de thèse
FORAY Geneviève	*Habilité à Diriger des Recherches INSA Lyon*	Co-directrice de thèse
ROIBAN Lucian	*Maître de Conférences INSA-LYON*	Invité

Acknowledgements

First of all, I would like to express my deepest gratitude to my supervisor Karine Masenelli-Varlot. This PhD work on microscopy is new field for me, she taught me patiently from zero, spent so much time doing experiments and analyzing data together with me. I appreciated a lot our discussions, which gave me much new inspiration and encouragement. I am extraordinarily glad to have worked with her and grateful for her care and help to my personal life.

I'm grateful to my co-supervisor Geneviève Foray for helping me analyzing her experimental materials and working carefully on my dissertation, and Lucian Roiban for teaching me data processing for tomography and giving me useful advice for my work.

I would like to express my gratitude to the members of jury: Ovidiu Ersen, Renaud Podor, Jean-Luc Putaux, and Diana Peckys. It was very generous of all members to take so much time in judging my work and to participate the jury. Your suggestions have been invaluable to improve obviously the quality of this thesis.

I appreciated all the people providing help on my work. In particular, my colleagues José Ferreira and his team for helping me develop the 3D stage, Annie Malchère for her training on ESEM, Siddardha Koneti for his advice on tomography, Anouk Perret for her help in samples preparation and Sylvie Descartes (LaMCoS), Xavier Jaurand (CTμ) and Pierre Alcouffe (IMP) for their work in cryo-SEM experiments.

Prof. Jérôme Chevalier is acknlowdged for welcoming me in Matériaux: Ingénierie et Science (Mateis) laboratory. I would like to acknowledge at the same time secretarial support from Alexandra Podgourskaia, Antonia Riccobene, Sandrine Gonnet. It was my honor to work in group SNMS with these nice colleagues: Philippe Steyer, Thierry Epicier, Berangère Lesaint, Florent Dalmas, Cyril Langlois, Thierry Douillard, Sophie Cazottes, Lucile Joly-Pottuz, Erkka Frankberg, Yangdi Li, Sergiu Curelea, Clément Lafond and all the other ones. And I haven't forgotten the help from my ex-colleagues Mohamed-Hedi Jomaa and Inas Issa.

I also want to thank Yizhen Sun, Xi Zhen, Xiaofang Wang, Xiaomin Xie, Xiuhua Tang and other friends for our time shared together in France. And at last, I would like to express my gratitude to my family, their care and understanding support greatly my work and life in Lyon.

China Scholarship Council (CSC) and Institut Universitaire de France are kindly acknolwdeged for financial support, and Consortium Lyon-Saint Etienne de Microscopie (CLYM) and Centre Technologique des Microstructures (CTμ) for the access to the microscopes.

Juan XIAO

Lyon, April 2017

Abstract

ESEM (Environmental Scanning Electron Microscopy) allows the observation of liquids under specific conditions of pressure and temperature. When working in the transmission mode, i.e. in STEM (Scanning Transmission Electron Microscopy), nano-objects can even be analyzed inside the liquid ("wet-STEM" mode). Moreover, *in situ* evaporation of water can be performed to study the materials evolution from the wet to the dry state. When studying concentrated solutions, the arrangement of the solute may change from the wet to the dry state and 3D characterization could bring interesting information. This work aims at developing electron tomography on liquid suspensions using STEM-in-ESEM, to obtain the 3D structure of nano-objects dispersed in a liquid.

In a first part, Monte Carlo simulations and 2D wet-STEM experimental images are combined to study the contrast of nanoparticles in water film. Two kinds of nano-materials in liquid are chosen: spherical gold particles (diameter around 40 nm) dispersed in water; aqueous suspension of latex SBA-PMMA, a copolymer derived from styrene and metacrylic acid esters, with 3% PMMA included as steric surfactant. The comparison between simulated and experimental results helps to determine how water can affect the contrast between water and the nano-materials. Besides, twelve nanoparticles of different compositions are simulated to determine the minimum size of a particle above which it can be detected (for a given water film thickness).

In a second part, tomography experiments are performed on dry polyurethane films containing ungrafted or grafted carbon multiwalled nanotubes, using a previously developed home-made tomography device, and the volume is well reconstructed. However, when performing tomography on latex SBA-PMMA suspensions, limitations are found on the temperature control of samples. We propose an optimization of the device with new observation conditions to better control water evaporation and condensation of liquid samples.

In a third part, we show a full 3D analysis on a SBA-PMMA latex suspension, with different concentrations - from the dilute state to a very concentrated one - obtained with optimized

conditions. The arrangement of the latex particles is compared with models from the literature and with experiments on frozen bulk samples observed by cryo-SEM. In can be concluded that the volume obtained are representative from the bulk. A further study is presented in presence of a surfactant. The surfactant layer can efficiently be evidenced from the encouraging reconstruction and segmentation results. This suggests that the resolution in the tomogram reaches at least 15 nm, which is better than the value calculated using Fourier Shell Correlation.

As a conclusion in this dissertation, we summarize the potentialities of wet-STEM tomography for the characterization of both solid and liquid nano-materials. Prospects are proposed to further study the potentialities and limitations of wet-STEM tomography in ESEM.

Résumé

La Microscopie Electronique à Balayage Environnementale (ESEM) permet l'observation de liquides dans certaines conditions de pression et température. En travaillant en transmission, i.e. en mode STEM (Scanning Transmission Electron Microscopy), des nano-objets présents au sein du liquide peuvent même être analysés (mode « Wet-STEM »). En outre, l'eau liquide peut être évaporée *in situ*, ce qui rend possible l'étude de l'évolution des matériaux de la suspension liquide jusqu'à l'état sec, et ouvre des opportunités de caractérisation inédites pour la formulation de composites architecturés. Dans les solutions concentrées, l'arrangement du soluté peut changer entre l'état humide et l'état sec, et la caractérisation 3D peut apporter des informations intéressantes et lever des verrous dans de nombreuses applications ou le matériau initial est liquide et le produit final un solide. Dans ce contexte, le but de ce travail est de développer la tomographie électronique sur des suspensions liquides en utilisant le mode STEM en ESEM, de manière à obtenir la structure 3D de nano-objets dispersés en suspension diluée ou très dense.

Dans une première partie, le contraste entre des nanoparticules et le film d'eau traversé est étudié en combinant des micrographies expérimentales Wet-STEM (en 2D) et des simulations Monte Carlo. Deux types de nano-matériaux dispersés dans de l'eau, sont choisis : des nanoparticules d'or sphériques, de diamètre environ 40 nm, un latex SBA-PMMA, de diamètre centré sur 200 nm. Ce copolymère est dérivé du styrène et d'ester acide métacrylique, et contient 3% de PMMA tensioactif stérique. La comparaison entre les résultats simulés et expérimentaux permet d'estimer comment le contraste entre l'eau et les nanomatériaux est affecté par l'épaisseur du film d'eau. En outre, douze nanoparticules de compositions différentes sont simulées afin de déterminer la taille minimum d'une particule au-delà de laquelle elle peut être détectée, ceci pour une épaisseur de film d'eau donnée.

Dans une seconde partie, des expériences de tomographie sont réalisées en utilisant une platine développée précédemment au laboratoire sur un matériau sec composite et sur le latex SBA-PMMA. Les films de polyuréthane étudiés sont chargés et contiennent des nanotubes de carbone multiparois greffés ou non, Le volume est reconstruit correctement à partir des

acquisitions réalisée, et les charges sont nettement observées. Le volume de latex en suspension n'est lui pas correctement caractérisé. Nous montrons que pour une acquisition 3D sur des suspensions de latex SBA-PMMA, le contrôle de la température de l'échantillon est encore insuffisant. Nous proposons une amélioration à la fois de la platine et des conditions d'observations permettant de finement contrôler l'évaporation et la condensation de l'eau sur des échantillons liquides chargés.

La troisième partie est dévolue à une analyse approfondie d'une suspension de latex SBA-PMMA, de différentes concentrations (d'un état dilué à très concentré), les acquisitions étant effectuées avec les conditions optimisées. L'arrangement des particules de latex est comparé d'une part à des modèles issus de la littérature, et d'autre part à des résultats expérimentaux4 obtenus par cryo-SEM sur suspensions congelées. Le volume ainsi obtenu peut être considéré comme étant représentatif du matériau polymère massif. Nous présentons pour conclure une étude du même latex en présence de tensioactif amphiphile pour nous rapprocher des problématiques de formulation industrielle. La couche de tensioactif est très clairement mise en évidence dans les volumes reconstruits et segmentés. Ceci suggère que la résolution dans le tomogramme est au moins égale à 15 nm, valeur plus faible que ce qui est calculé à partir de la méthode Fourier Shell Correlation, et ouvre des perspectives intéressantes pour formuler des composites.

En conclusion de ce mémoire de thèse, nous résumons les potentialités de la tomographie wet-STEM pour la caractérisation de nanomatériaux composite en voie liquides diluées ou denses, mais aussi en voie solide. Des perspectives sont proposées pour continuer dans l'exploration de ces potentialités mais aussi mieux appréhender les limites de cette technique d'imagerie et de caractérisation.

Table of Contents

General Introduction

Several kinds of materials contain water or are dispersed in water during their process, and the water phase is often the key to reach the targeted functional properties. For instance, biological cells include a high fraction of water; latex suspensions are composed of polymer particles dispersed in water; some ceramics are dispersed in liquids using surfactants to reach high density bulk ceramics; nanoparticles may be synthesized directly in liquids. In all cases, a complete knowledge of the dispersion in the suspension is useful to understand the materials' properties. Several techniques are accessible to observe the liquid samples, and nanometer resolution can be realized by using dedicated specimen holders either in standard electron microscopes (either in transmission (TEM) or scanning ones (SEM)), or with dedicated microscopes (ESEM).

A two-dimensional (2D) projection illustrates the information only on one single plane, it thus may not allow a precise interpretation of the object internal structures, especially if their microstructure is complex along the sample thickness. Occasionally, a 2D projection may even lead to a misinterpretation of structural information such as distance, localization, connectivity, and distribution of heterogeneities in the sample. Therefore, three-dimensional (3D) characterization, combining the information from different orientations of the samples, has become more and more important to understand the elaboration and assembly of materials. Moreover, the physical and chemical properties could be further studied with the precise microstructure information acquired from tomography.

Among different tomography techniques, electron tomography in TEM or in ESEM are of concern to study piled-up nano-particles in liquid samples. Sealed liquid cells used for TEM tomography allow the observation with a good stability (no evaporation or condensation), and a relatively controlled water film thickness. However, the electrons have to pass through an increasing thickness of silicon nitride membranes in addition to the increasing thickness of the water film when the sample rotates at high angles. The thick support, surrounding the electron transparent window, may also hide the region of interest when tilting the sealed cell.

Therefore, tomography in ESEM may be the best choice to analyze liquid specimens in 3D with nanometer resolution. This PhD work deals with the development of electron tomography on liquid suspensions using this specific technique. Several issues first need to be solved to achieve our goal. First, the thickness of the water film can be tuned *in situ* by controlling the environment pressure and the sample temperature. This is undoubtedly an advantage since water can be condensed or evaporated *in situ*, but it is also a drawback as the thickness of the water film remains unknown and its variations may lead to contrast inversions. Second, the equilibrium state might be difficult to keep for a time long enough to acquire a series of images for tomography. Indeed, water may condense or evaporate, and irradiation damage may occur.

In this dissertation, we will try to address these issues in details through five chapters:

Chapter 1 presents a bibliographic work on different microscopy techniques used for the observation of liquid materials, and several tomographic techniques with different resolution abilities. In light of this review, we explain why we focused on the 3D characterization of liquid suspensions using ESEM.

Chapter 2 gives details of the selected model materials used in this work: a latex SBA-PMMA suspension eventually with a high molecular weight surfactant, a gold nanoparticles suspension, and PU-carbon nanotubes nanocomposites. The two first material are dilute or dense suspension based on spherical nano-particles, while the last one is a dry composite including carbon nanotubes. The analysis techniques are also briefly explained: 2D analysis methods including wet-STEM and GSED mode in ESEM, cryo-SEM, as well as Monte Carlo simulations; our home-made 3D device using wet-STEM mode in ESEM, as well as 3D data processing methods.

Chapter 3 studies the relationships between contrast and water film thickness, by combining 2D wet-STEM experimental characterizations and some Monte-Carlo simulations on two kinds of liquid nano-materials: spherical gold nano-particles (diameter of 40 nm) suspension and latex SBA-PMMA (diameter of 200 nm) suspension. Besides, twelve nanoparticles of interest were simulated so as to determine the minimum size of a particle which can be detected (for a given water film thickness).

Chapter 4 first presents a nice tomography result on dry polyurethane films containing carbon nanotubes, using a previously developed home-made tomography device. This dry polymer composite is well characterized, qualitative and quantitative information are gathered on matrix and carbon nanotube arrangement. But the reconstruction on latex suspension is found some deficiency, mainly due to an unrefined control of samples temperature. Thus an optimization of the device is proposed so as to perform tomography properly on liquid sensitive materials.

Chapter 5 shows a full 3D analysis on SBA-PMMA latex from dilute suspension to very concentrated one performed with optimized experimental conditions, and a further study in presence of a surfactant to open toward real industrial application in material formulation. The particles arrangement is modeled and successfully compared with first some literature results and second some cryo-SEM analysis results.

Finally, a general conclusion is drawn and perspectives are proposed to further develop this technique and gain some knowledge on governing limitations.

Chapter 1: Introduction

1.1 Context

Several kinds of materials contain or are dispersed in water during their process, with water phase being the key vault that ensures reaching the functional properties target. For instance, biological cells include a high fraction of water. Latex suspensions, composed of polymer particles dispersed in water, are used for numerous applications, among which paints, concrete, glues or as binders for super-insulators. Some mineral nano or micro powders have to be dispersed in liquids, eventually using surfactants, and processed to reach high density bulk ceramics *[P. Yu et al. (2008)]*, *[G. Foray et al. (2012)]*, *[G. Spina et al. (2012)]*. A last example involves nanoparticles synthesized directly in liquids, via chemical or physical processes, such as precipitated silica or aerogels. In all cases, a complete understanding of the dispersion in the suspension at the nanoscale is useful to understand the materials' properties.

For some complex samples, two dimensions (2D) images from microscopy could not offer the right structure information *[J. P. Y. Tan, et al. (2011)]*. Tomography is able to reconstruct the material volume in three dimensions (3D), which allows a better description of the microstructure within the materials, and thus provide some qualitative information. It also provide some valuable quantitative information of the specimens with resulting reconstructed volume *[J. Park et al. (2015)]*.

1.2 Observation of liquid materials

The observation of liquid materials from micrometer to nanometers is playing an increasing role especially in life science. Several techniques accessible to observe the liquid samples are introduced in the following. Each one of the currently available methods has specific advantages and drawbacks that makes it suitable for some specific applications.

1.2.1 Optical Microscopy

Optical microscopy is probably the oldest microscopy method. It uses visible light and a system of lenses to magnify the small samples. The important features for an optical microscopy include light source, eyepieces (oculars), lenses and camera. After the magnification by the lenses, the images are generated with light-sensitive cameras, originally photographic film, but modern charge-coupled device (CCD) cameras permit the acquisition of digital images. Purely digital microscopes are now available to display the resulting image directly on a computer screen using a CCD camera.

1.2.1.1 Conventional optical microscopy

Basic optical microscopy can be very simple with only one lens for magnification. In order to improve resolution and contrast, optical microscopy has developed greatly by adding some complex designs. One of the vast developments of modern optical microscopy is the compound microscope that enhances the magnification by using several lenses. In the compound microscope, the lens near the sample (objective lens) is used to form a real image, which then magnified by another lens or group of lenses (eyepiece). Usually several exchangeable objective lenses are available in the compound microscope so that the magnification could be adjusted conveniently *[I. M. Watt, (1997)]*. Today many special designs have already been used in optical microscopy, which extends its use in many fields, especially for hydrated biology samples.

However, one of the main limitations for optical microscopy is its resolution ($R= \lambda/2NA$). It is affected by both the wavelength of light (λ) and the numerical aperture (NA), a measure of the light gathering capabilities of an objective lens ($NA = n \sin \alpha$, where n is the index of refraction of the medium in which the lens is working, and α is the maximal half-angle of the cone of light that can enter or exit the lens). Assuming a usual wavelength of 550 nm (corresponding to green light) and the highest practical NA of 0.95 with air as the external medium, the resolution obtained with conventional lenses is about 200 nm. Recently, some new techniques have developed to improve greatly the resolution of optical microscopy *[V. Protasenko et al. (2005)], [E. G. van Putten et al. (2011)], [M. J. Booth, (2014)]*. In 2014, E.

Betzig, W. E. Moerner and S. W. Hell awarded the Nobel Prize in Chemistry for the development of super-resolved fluorescence microscopy, which brings optical microscopy into the nano-dimension. Recently, J. Enderlein reported that optical microscopy could go subnanometer resolution with DNA-PAINT *[J. Enderlein. (2016)]*. In spite of much significant progress in the last decade, the techniques for improving resolution remain limited and specialized. Besides, the low depth of field is also a limitation for optical microscopy when comparing with other microscopy methods.

1.2.1.2 Confocal microscopy

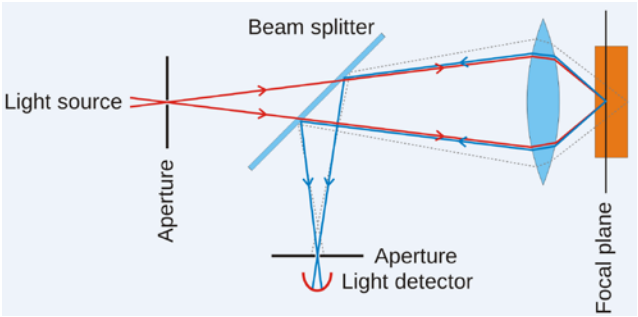

Figure 1. Diagram of confocal principle

Confocal microscopy, most frequently confocal laser scanning microscopy, is an optical imaging technique which uses a scanning laser to illuminate a sample for fluorescence. A spatial pinhole is added in the confocal plane of the lens to eliminate out-of-focus light *[J. B. Pawley, (2006)]*, which increases the optical resolution and the contrast in the images, especially for thick samples. Whereas in conventional optical microscopy the images rely on the penetration of light, the confocal microscopy images depend on a controlled and highly limited depth of focus, which makes it unique in depth discrimination *[J. Tan and F. Wang, (2002)]*.

Due to the arrangement of diaphragms in confocal microscopy, the optically conjugated points act as a point of source and as a point of detector respectively, as shown in the diagram of confocal principle (see Figure 1). Therefore, the rays from out of focus are suppressed by the detection pinhole, which means the images include no information of the structures out of

focus. This confocal effect depends on the size of the detection pinhole, as a wider one will reduce the confocal effect. The wavelength of light, the depth of the focal plane is also determined by the numerical aperture of the objective and the diameter of the diaphragm. The image point is moved across the sample by mirror scanners to acquire a full image. The emitted/reflected light passing through the detector pinhole is transformed into electrical signals by a photomultiplier and displayed on a computer monitor screen *[C. L. Smith, (1997)]*.

In comparison with conventional optical microscopy, confocal microscopy suppresses the light rays from outside the focal plane, removes the blurring due to defocus and minimizes the stray light thanks to the small dimension of the illuminating light spot in the focal plane, which improves the resolution and contrast of the resulting images. Furthermore, it scans the specimens not only in the x/y-directions but also in the z-direction (along the optical axis), which allows the observation of the objects from all sides. This technique has gained popularity in the scientific and industrial communities, typically for biological application. Recently, achievements have been made to improve image quality, in particular resolution *[S. Lee and D.-G. Gweon, (2008)]*. Results have been reported where the resolution has been achieved decades of nanometers *[V. Westphal et al. (2003)], [M. Dyba and S. Hell, (2002)]*.

Although breakthroughs have been achieved for some special use in optical microscopy, the resolution and depth of field are still limited by the wavelength of light and the optical lenses in most cases. Considering its simple and convenient operations, especially regarding sample preparation, and almost no damage in the sensitive specimens, optical microscopy still plays an essential role in the study of the microstructure.

1.2.2 X-ray microscopy

X-ray microscopy is a collection of methods to produce magnified images of objects using X-ray radiation. There are two main principles of microscopes to be distinguished: conventional transmission X-ray microscopy (TXM) and scanning transmission X-ray microscopy (STXM). In TXM, an objective lens is placed after a condenser, and produces a magnified image of a sample in the detection plane. TXM images the whole field of view to a detector plane at the same time, so it often referred to as field-of-view or full field X-ray microscopes. In a STXM,

an objective lens focuses an X-ray beam onto a small-sized spot on the sample, the sample is raster-scanned, and the transmitted X-ray intensity is recorded as a function of the sample position.

Both TXM and STXM own their special advantages. The main advantage of TXM lies on its high data acquisition rate. The typical exposure time to get a TXM image is several seconds, while several minutes are needed for STXM. A short exposure time decreases problems like beam instability, vibration, and thermal drift, may practically result in a higher spatial resolution. As a kind of scanning instrument, STXM allows the simultaneous detection of various signals with the use of different detectors. It is possible to record both X-ray images and fluorescence emission photons *[V. V. Lider, (2017)]*.

The resolution of X-ray microscopy lies between that of the conventional optical microscope and the electron microscope. The wavelength of X-rays is much shorter than that of visible light, so the limit of the optical resolution (caused by diffraction) of X-ray microscopes is far below the diffraction limit of optical microscopes. In comparison with conventional electron microscopy (although with a high image resolution), X-ray microscopy images the sample with high contrasts provided by density changes in the specimen. It is thereby possible to avoid long specimen preparation, such as fixation and staining, and permits the observation of thicker specimens without sample preparation or alteration *[Y. Yamamoto and K. Shinohara, (2002)]*.

With the development of new X-ray sources, high resolution X-ray microscopy is becoming possible. X-ray microscopy is applied increasingly along with optical and electron microscopies in different areas, such as biology *[J. C. Andrews et al. (2011)]*, materials science *[Lawrence J R et al. (2016)]*, and environment *[T. H. Yoon (2009)]*. It is noteworthy that the high resolution studies are carried out on synchrotron beamlines, where the X-ray beam is very intense.

1.2.3 SEM (Scanning Electron Microscopy)

SEM (scanning electron microscopy) begins its use in the 1930s and becomes commercially available in 1965. Thanks to the short wavelengths of electrons and their ability to be focused by electrostatic and electromagnetic lenses, SEM images the samples at the microscopic and even nanoscopic level with high resolution and large depth of field. Additionally, the strong interaction between electrons and matter generates a wide variety of useful signals that offer the microstructure, composition and properties information of bulk materials.

In general, SEM is mainly composed of an electron gun for the production of the primary electron beam; a column with several condenser lenses to focus the primary electron beam; coils to scan the sample surface pixel-by-pixel; a chamber with a sample stage to hold the specimen; vacuum pumps to control the system pressure; detectors to collect the electrons generated from the interactions between the electron beam and the specimen; an image processing system to display the final image on a monitor.

In the SEM, the principal signals generated from the interaction between the incident electron beam and the specimen are illustrated in Figure 2. The SEM images are usually formed by collecting the following signals from the surface or near-surface of bulk materials: backscattered electrons (BSE), secondary electrons (SE), or X-rays *[J. Goldstein et al. (2003)]*. The usual thickness of the sample for SEM analysis is several millimeters, and the length or diameter could be up to several centimeters. Thus SEM avoids the difficulties of preparing thin samples as for TEM (transmission electron microscopes). The electrons transmitted through thin samples can also be collected in SEM. This mode is often called “STEM-in-SEM” in order to distinguish from the traditional scanning transmission electron microscope (STEM) in TEM. In this manuscript, this latter mode will be called “STEM-in-TEM”.

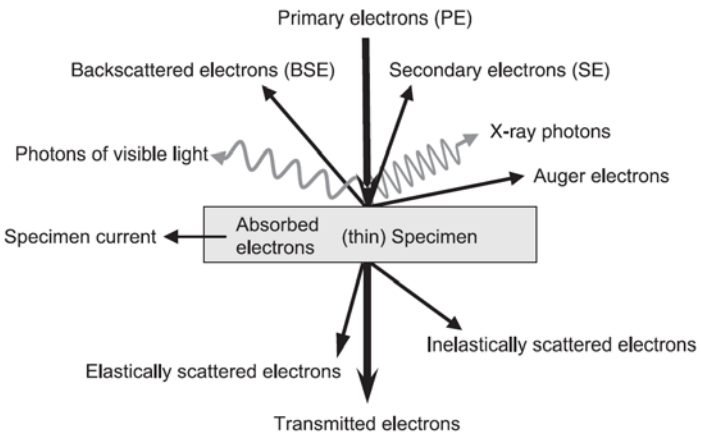

Figure 2. Scheme showing a range of signals in SEM. For bulk specimens, these include backscattered and secondary electrons, various photons such as X-rays and visible light and Auger electrons. For thin specimens, transmitted and scattered electrons provide information from the degree and nature of scattering [D. J. Stokes, (2013)]

The most straightforward materials for SEM are metals, principally because they are less prone to the effects of charging and damage under electron irradiation in high vacuum. For poorly conducting materials, such as polymers and ceramics, the charging effects could be decreased by increasing the conductivity for instance by coating the surface with conductive materials (usually gold deposited by sputtering). Aqueous and hydrated samples are traditionally not suitable for the conditions in the SEM, mainly because the SEM column and sample chamber have to be kept under vacuum. A first solution could be the use of a sealed cell (QuantomiX WETSEM®), where the liquid is confined in a capsule fitting into a standard SEM sample chamber. Any liquid can be used and kept at atmospheric pressure. The images are then obtained using backscattered electrons or x-rays and are representative of the objects placed just below the cell top membrane.

In the following sections, we describe two other methods based on SEM which can be used to analyze an unconfined liquid sample. The first one (cryo-SEM) involves a specific sample preparation and observation mode, whereas the second one (ESEM, for Environmental Scanning Electron Microscopy) implies a specific microscope design.

1.2.3.1 Cryo-SEM

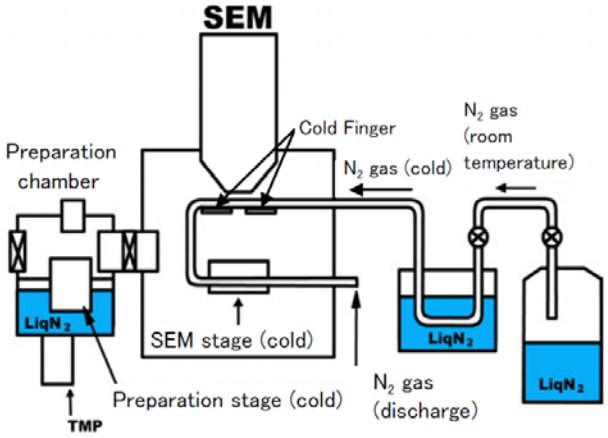

Figure 3. A cryo transfer system ALTO 2500 (Gatan UK) used for field emission SEM (installed in JIB-4600F from JEOL)

The technique called “Cryo-SEM” refers to a SEM equipped with a cryo transfer system. It allows the direct observation of frozen samples and is considered to be the best way to observe biological materials as close as possible to their native state *[P. Walter, (2008)]*. Typically, a cryo system consists of two parts: a cryo (preparation) chamber and a cold stage. Figure 3 illustrates a cryo system model ALTO 2500 from Gatan, where gaseous nitrogen is used as a coolant chilled with liquid nitrogen. Gaseous nitrogen circulates through a tube inside the SEM specimen chamber. It thus cools down the cold trap fin, the stage and the specimen. The preparation chamber is pumped by a single turbo molecular pump (TMP). The ultimate temperature in this system, -190°C, could be achieved quickly in about 15 min.

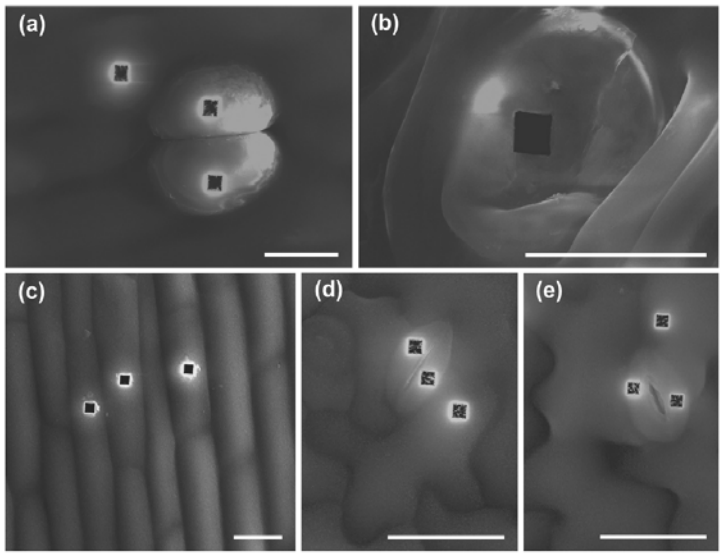

Figure 4. Cryo-SEM images after ion milling. (a−c) Sphagnum subnitens. (d,e) Arabidopsis. (a) Swollen fully hydrated capsule wall. (b) Shrunken stoma after 50–60% water loss. (c) Hydrated elongated capitulum. (d) Closed stoma from a wilted plant. (e) Open stoma. Bars, 20 μm [J. G. Duckett et al. (2009)]

The specimen preparation for cryo-SEM exhibits several advantages over conventional techniques, such as a critical point drying *[N. Roos, A. J. Morgan, (1990)]*: chemical fixation followed by dehydration and drying is omitted. High quality freezing of hydrated samples produces minimal dimensional changes, such as shrinkage and distortion resulting from drying *[M. Psenicka et al. (2010)]*. Furthermore, rapid specimen preparation allows the study of dynamic events as well. Signal strength may be considerably improved with the reduced charging of the materials surface, thus cryo-SEM could achieve a high resolution even at a low accelerating voltages *[S. N. Gorb et al. (2007)]*. Interesting examples are shown in Figure 4. Microstructure changes in hydrated biological specimens could be observed clearly with cryo-SEM.

1.2.3.2 ESEM (Environmental Scanning Electron Microscopy)

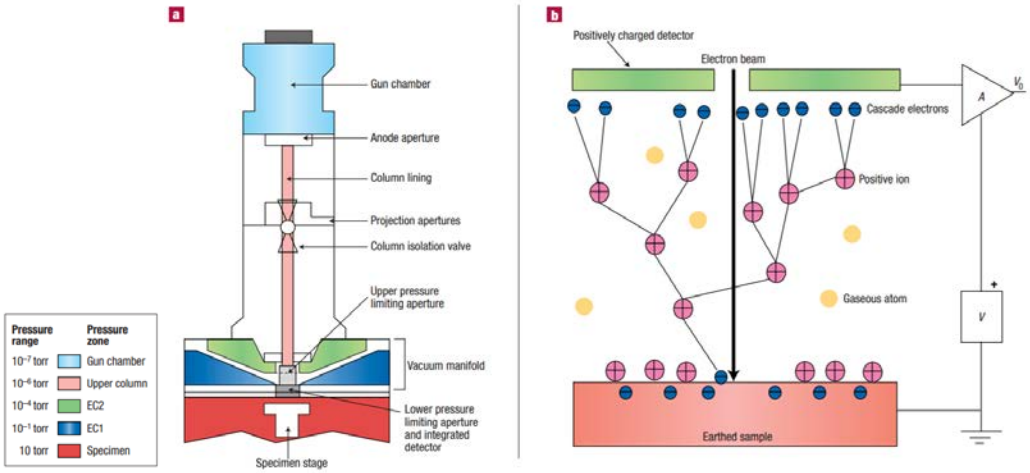

Figure 5. Schematic of ESEM: a. the different pressure zones in the ESEM column. b. the cascade amplification process [A. M. Donald, (2003)]

ESEM (environmental scanning electron microscopy) can also be used to study liquid suspensions. Thanks to a system of differential pumping- and pressure-limiting apertures, the gun chamber can be maintained under high vacuum, while the pressure in sample chamber can reach a few Torr (1 Torr = 133 Pa), as shown in Figure 5a. Several kinds of gas could be introduced into the specimen chamber, such as water vapor, oxygen, nitrogen, hydrogen. The presence of gas within the sample chamber causes the occurrence of a cascade amplification process, represented in Figure 5b, where the gas molecules are ionized by the electrons emitted from the sample. A daughter electron, generated during each ionizing collision, is accelerated towards the positively charged detector, and further collisions can occur *en route* to the detector. During this process, positive ions drift back towards the sample surface, which increases the conductivity of insulating materials surface *[A. M. Donald, (2003)]*. The amplification ability of several gases has been studied and water vapor has turned out to have excellent amplification characteristics *[A. L. Fletcher et al. (1997)]*.

The use of a Peltier stage offers the possibility to control the temperature of the sample. According to the dew curve of the water phase diagram, ESEM allows the observation of wet objects in fully hydrated states by simultaneously controlling the water vapor pressure in the

sample chamber and the sample temperature *[D. Stokes, (2008)]*. Figure 6 gives the example of a secondary electron ESEM image of gypsum with 100% relative humidity *[D. J. Stokes, (2012)]*. Besides, the ability to control water condensation and evaporation enable *in situ* studies of suspensions. For instance, film-formation processes from latex suspensions could be observed using ESEM.

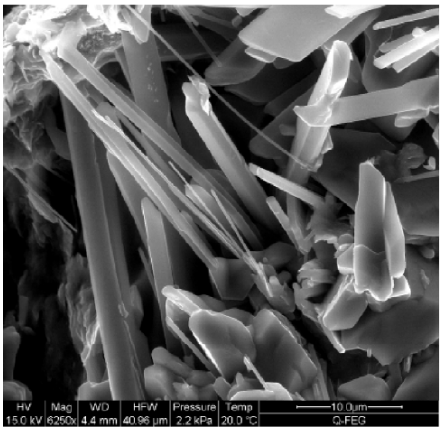

Figure 6. Secondary electron ESEM image of gypsum under conditions of high pressure: 2.2 kPa (16.5 torr) water vapor and specimen temperature of 20°C. These conditions ensure ~100% relative humidity. By E. Baken [D. J. Stokes, (2012)]

Even though it is possible to observe wet objects and liquids in ESEM, the technique suffers from several drawbacks. First, it is necessary to use a relatively high accelerating voltage to ensure a high enough amplification by the gas. Second, the resolution in the images can be significantly decreased as the primary electron beam is broadened due to interactions of the primary electrons with gas molecules. This phenomenon, known as the “skirt effect”, increase when increasing the gas pressure. The third drawback implies the detection mode: secondary electron images give information about the sample surface. In the case of a suspension (objects dispersed in liquid), the objects inside will mainly remain invisible. The “wet-STEM” mode has therefore been developed to solve this issue.

1.2.3.3 Wet-STEM in ESEM

Wet-STEM has been developed for the characterization of suspensions in ESEM. It is based on the scanning transmission mode (STEM-in-SEM). In STEM, a focused electron beam scans a thin specimen 'point-by-point'. A detector placed below the specimen collects the electron transmitted through or scattered by the sample. Nano objects in a liquid phase could therefore be observed thanks to the high resolution of STEM images.

Although the accelerating voltage in SEM is quite low (typically with a maximum value of 30 kV), there may still be a significant fraction of electrons transmitted through thin samples of thickness up to a few microns, depending on the density of the specimen. When working in the environmental mode, wet-STEM images with high resolution can be obtained by collecting electrons with a detector placed below the wet objects *[A. Bogner et al. (2005)]*. Indeed, good contrasts arise from the detection of the scattered electrons, even on low atomic number materials. The procedure has been optimized for the detection of gold nanoparticles attached to surface membrane proteins of whole fixed cells, resulting in a resolution of 3 nm *[D. B. Peckys et al. (2009)], [D. B. Peckys et al. (2013)]*.

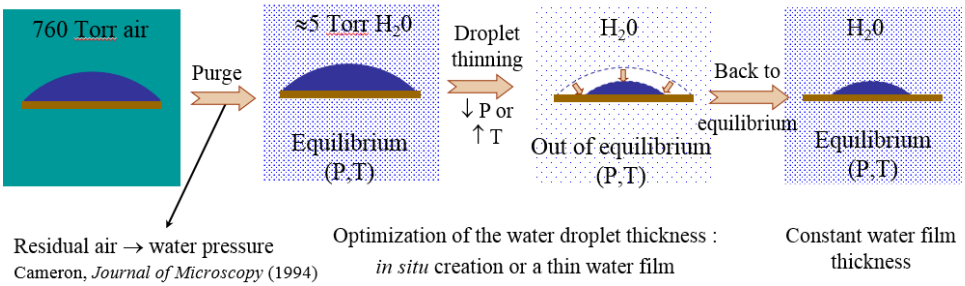

Figure 7. The thinning process of a liquid droplet during ESEM experiment

At the beginning of a wet-STEM experiment carried out on a liquid suspension, it often happens that the liquid droplet is too thick. In this case, no signal can be detected in STEM. Thanks to the controllable water vapor pressure in ESEM chamber and sample temperature by the Peltier stage, the droplet could be thinned so as to a thickness suitable for imaging in STEM mode, as can be found from Figure 7. If required, the dynamic evolution can also be followed *in situ*, when evaporation occurs for example, which constitutes an advantage of wet-

STEM in ESEM. This observation mode has successfully been applied to several suspensions or emulsions (not only in water) *[A. Bogner et al. (2007)]* and has also been used to reveal the surfactant outcome during water evaporation and film formation from latex suspensions *[J. Faucheu et al. (2009)]*.

However, its main drawback lies also in the fact that the thickness of the water film can be changed by controlling evaporation and condensation of water, but the absolute value of this thickness remains unknown. Yet, the water thickness affects the contrast of the object in suspension state, and even contrast inversions may occur. Therefore, estimating the thickness of the water film is of prime importance.

1.2.3 TEM (Transmission Electron Microscopy)

TEM, operating at high accelerating voltage, has the ability to form images with very high resolution. As conventional TEM operate under vacuum, wet objects cannot be observed without any preparation. They can either be frozen, as in cryo-SEM (mode called cryo-TEM) or confined into a sealed liquid cell.

1.2.3.1 Cryo-TEM

Cryo-TEM is a technique well suited for the observation of thin vitrified aqueous films at liquid nitrogen temperature in TEM *[J. Dubochet et al. (1988)]*. For the preparation of a thin electron-transparent sample, the solution is first deposited to a microscopy grid so as to form a very thin aqueous film. It is then is plunged into a cooling medium, such as ethane just above its freezing point, where the film can vitrify very rapidly, without crystallisation. Afterwards, the vitrified film on the grid is transferred to TEM, and imaged at liquid nitrogen temperature.

During the process of cryo-TEM sample preparation, no artefact due to conventional staining or drying procedures is introduced, no dehydration during observation owing to the structures are captured in the vitrified film, and minimum perturbation of the original sample structure thanks to rapid cooling rate. Therefore, cryo-TEM is an ideal technique suited for imaging delicate and dynamic structures, such as those formed by lipids and surfactants, and has been

extensively used in biology *[A. Al-Amoudi et al. (2004)]*. However, this sample preparation method at the same time brings the problems such as varying film thicknesses, as well as sorting mechanisms, which makes quantitative measurements difficult *[M. Almgren et al. (2000)]*.

1.2.3.2 Wet-STEM in TEM

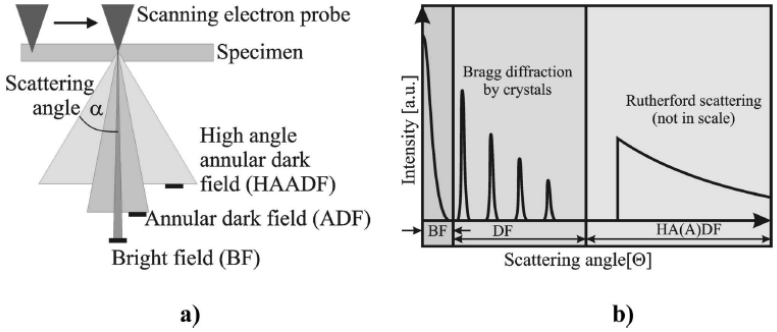

Figure 8. (a) Ray diagram indicating the scanning probe, the scattering angles and the respective detectors collecting the scattered electrons. (b) Qualitative representation of scattering ranges [J. Loos, et al. (2009)]

A major step forward for imaging wet objects with high resolution has been made by the development of specific sample holders in STEM mode. A typical one, sealed liquid cell, is made up of two silicon microchips with electron transparent windows sealed together with epoxy, as shown in Figure 9. Thin membranes made of silicon nitride enclose the liquid. Nanoparticles are located on the silicon nitride window at the beam entrance side of the liquid enclosure.

When using a liquid cell in TEM, the STEM mode is usually used to obtain high resolution images. This means that the focused electron beam passes through this cell towards the detector, and the image is formed by scanning the electron beam over the sample *[N. de Jonge & F. M. Ross (2011)]*. In STEM, transmitted electrons are scattered at various angles due to the different beam-specimen interactions, and can be collected by different detectors placed below the sample depending on the scattering angles (Figure 8). In particular, the High Angle Annular Dark Field (HAADF) detector collects electrons scattered at high angle. These

electrons do not carry diffraction information and the contrast in the image is mass-thickness dependent. STEM is operated in in-focus conditions so that less imaging artifacts are created and image interpretation is more straightforward. Furthermore, the resolution in STEM is determined at the illumination side (that is before the specimen) where electrons have an energy spread below 1 eV, thus it is affected by chromatic aberration less than the conventional TEM *[J. Loos, et al. (2009)]*.

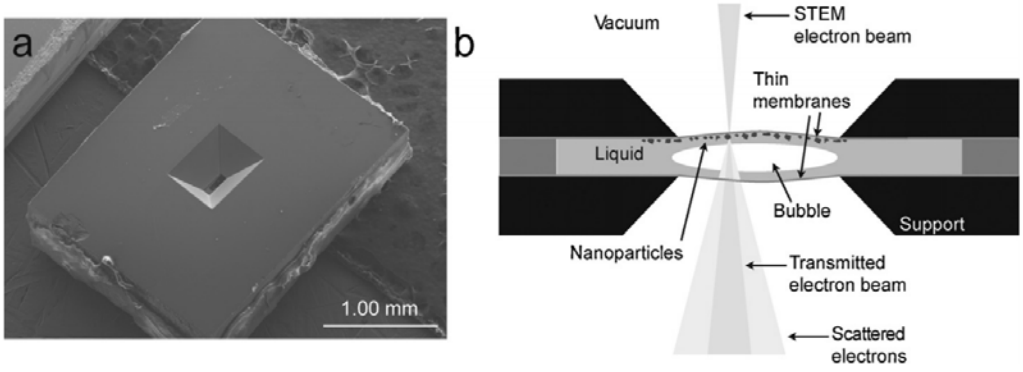

Figure 9. Enclosure for liquid samples used in STEM mode. (a) Scanning electron microscopy image of the liquid enclosure, recorded at 10 kV (S4700 Hitachi). (b) Side-view cross section schematic of the liquid enclosure. Note the bowing of the membranes, and possible formation of a water vapor bubble [E. A. Ring & N. de Jonge (2012)]

With such microscopes or sample holders, *in situ* experiments can be carried out in TEM. One can cite studies of nanoparticle motion in liquids *[H. Zheng et al. (2009)]*, *[E. A. Ring & N. de Jonge (2012)]*, *[Q. Chen et al. (2013)]*, investigations of nanoparticle growth from solutions *[J. E. Evans et al. (2011)]*, *[D. Alloyeau et al. (2015)]* or direct visualization of electrochemical processes *[J. Y. Huang et al. (2010)]*, *[X. Chen et al. (2012)]*. F. M. Ross recently published a review of the advances and challenges of liquid cell sample holders for TEM *[F. M. Ross, (2015)]*, *[F. M. Ross, (2016)]*.

However, due to the high energy of incident electron beam, serious radiolysis may occur in this liquid cell during the experiment. As ionizing radiation passes through the liquid cell, energy is transferred from the fast-moving electrons to the irradiated medium *[N. M. Schneider, M. M. Norton, (2014)]*. As a sensitive suspending medium, the water in hydrated samples is

prone to be excited by the energy, generating a lot of chemical species, such as H_2, O_2, H_2O_2 and hydrated electrons. The radiation-induced species can cause reduction and precipitation of cations from solution, dissolution of metals, and nucleation and growth of bubbles *[J. M. Grogan et al. (2012)], [J. M. Grogan et al. (2014)]*.

Table 1. Comparison of different microscopy techniques used for liquid materials

	Sample preparation	Resolution	Damage	*In situ* study
Optical microscopy	Simple	Low	No	Yes
X-ray microscopy	Simple	Medium	No	Yes
Cryo-SEM	Complicated	Medium	No	No
ESEM	Simple	Medium	Yes	Yes
Wet-STEM in ESEM	Simple	High	Yes	Yes
Cryo-TEM	Complicated	High	Yes	No
Wet-STEM in TEM	Simple	High	Yes	Yes

In conclusion, each technique has its advantages and disadvantages. Table 1 gives a simple comparison in terms of sample preparation, resolution, damage and *in situ* studies. For concentrated liquid specimens, 2D images may give limited, even incorrect information, thus 3D characterization is required. The different techniques used to obtain 3D information are introduced in the next section.

1.3 Tomography in materials science

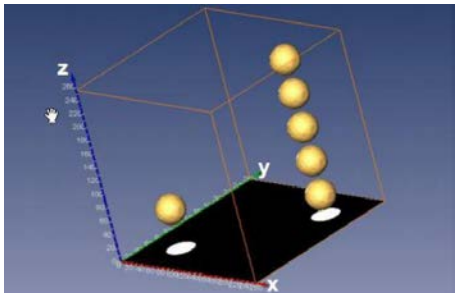

Figure 10. Projection of a volume containing spheres, showing 2D projection results in errors [Benlekbir2009, thesis]

Nowadays, several different tomography techniques, like X-ray tomography, electron tomography and atom probe tomography, could be chosen to perform 3D characterization. Tomography includes destructive and non-destructive methods. Destructive methods are based on serial sections such as focused-ion beam (FIB) tomography, and non-destructive methods are based on the reconstruction from projections as in electron tomography or X-ray tomography *[G. Möbus, B.J. Inkson, (2007)]*. The choice of the technique for 3D characterization depends on several different parameters such as materials properties, field of view, required resolution and possible constraints on sample preparation. Figure 11 displays the several tomography techniques as a function of the field of view and spatial resolution. Typically, the size of the analyzed volume decreases as the spatial resolution improves.

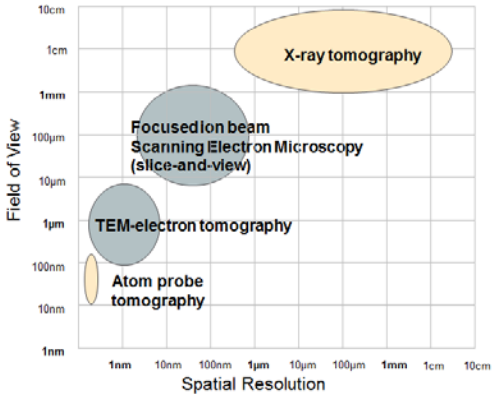

Figure 11. Several tomography techniques used for different field of view and spatial resolution in materials science

According to observation scale, tomography techniques are available with the accessible resolution ranging from the millimeter to the nanometer, and even sub-nanometer *[H. Kano, et al. (2002)]*. Generally speaking, for a specimen with the scale range from 500 nm to 1 mm, X-rays tomography is a suiTable tool *[E. Maire et al. (2001)]*. TEM tomography *[A. J. Koster et al. (2000)]* or atom probe tomography *[D. Blavette et al. (1993)]* are used for the specimens that higher resolutions, at several nanometers or even sub-nanometer, are required. SEM-based techniques, such as focused ion beam (FIB) *[A. J. Kubis et al. (2004)]* or serial block face SEM *[J. J. Mancuso, (2012)]*, are used for intermediate resolutions, between 10 nm and 500 nm.

1.3.1 X-ray tomography

X-ray tomography has the ability to image the sample with a large size range, from the human body to micrometric samples. Unlimited by the analyzing size as other tomography which only allows reconstruction for small parts of a large sample *[G. Möbus, B.J. Inkson, (2007)] [R. Leary, et al. (2012)]*, X-ray tomography is a technique that offers three-dimensional imaging on large materials without destroying the samples *[L. Salvo, et al. (2003)]*. As a matter of fact, it is the first technique performed for tomography, used in medicine with a typical resolution of 300 micrometers for decades of years. It has now been widely used in the field of materials characterization to investigate the microstructure and the deformation mechanisms of various structural materials, from foams and alloys to high performance composites. X-ray tomography is used to reveal the interior microstructural features of the samples, like cracks, inclusions, pores, etc.

The setup of an X-ray tomograph mainly consists of three parts: an X-ray source, a rotation stage, on which the object is fixed, and an X-ray detector, usually a CCD camera. Spatial resolution is one of the crucial consideration for the use of X-rays in materials science, which mainly depends on the X-ray source *[P.J. Withers (2007)]*.

A cone-beam system with a classical microfocus X-ray tube as the source limits the resolution to 8 μm, which is usually medium resolution for X-ray tomography. In this case, the magnification could be adjusted only by changing the distance between the sample and the source due to the diverging geometry of the X-ray beam, as shown in Figure 12a. The size of the microfocus largely determines the resolution of the X-ray tomogram: the smaller the focus size, the better resolution. At the same time, the focus size highly depends on the delivered X-ray power, a lower power delivered by the X-ray tube being the key for a better focus size. By considering at the same time some other factors, like an acceptable acquisition time, realistic conditions should be a compromise between the focus size and the delivered X-ray power. Moreover, a polychromatic beam is usually used in laboratory setups. However, with this kind of X-ray source, beam hardening could bring artifacts and impossibility for quantitative reconstruction of the absorption coefficient without prior calibration.

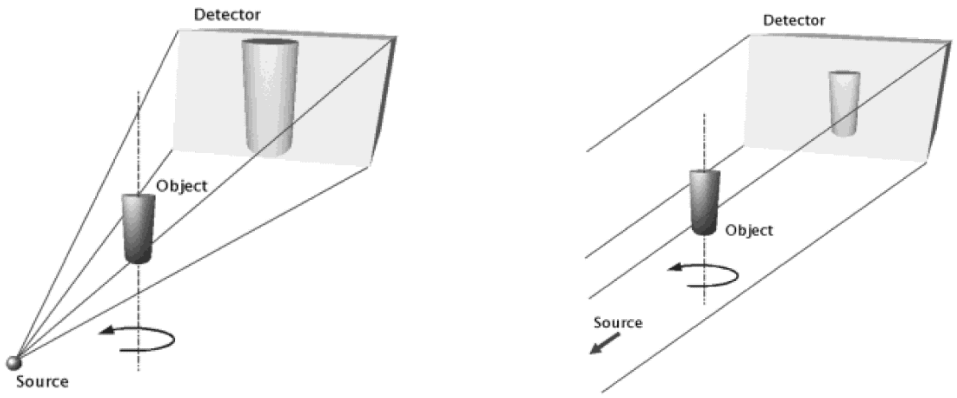

a) *b)*

Figure 12. Scheme of the tomography technique with different X-ray source: a) classical microfocus X-ray tube; and b) synchrotron radiation [E. Maire et al. (2001)]

Another possible X-ray source is the synchrotron radiation produced by ultra-relativistic electrons in a storage ring when they are accelerated by a magnetic field. This kind of X-rays beam, assumed to be parallel *[L. Salvo et al. (2003)]* as shown in Figure 12b, increases the signal-to-noise ratio and spatial resolution in the images. This may be attributed to its very high intensity and monochromatic character of the beam. These good features solve the problems of beam hardening effect and make quantitative reconstructions available.

A dedicated tomographic equipment using synchrotron radiation as X-ray source can be found at European Synchrotron Radiation Facility (ESRF) in Grenoble. It combines a mechanical sample stage with a fast, high-resolution detector system. The rotation and translation of the sample on the stage could be controlled with high precision. The detector system is composed of a fluorescent screen (YAG: Ce), which transforms the X-rays into visible light, and microscope optics to project the image on a cooled 1024^2 CCD camera, with a dynamic range of 14 bits, a fast readout (0.22 s/frame), and low-noise electronics (3 e^-/s). This combination improves the resolution of X-ray tomography. Furthermore, this synchrotron facility could host a nano-imaging end station *[G. Martinez-Criado, et al. (2012)]*, which improves the resolution of X-ray tomography to even sub-100 nm *[J. Villanova, et al. (2014)]*, *[C. Rau, et al. (2007)]*, *[D. Roussel, et al. (2016)]*. Moreover, in situ microstructural evolution for some materials under load could be realized coupled with a tensile stage. S. Dezecot et al. studied

in situ damage initiation and growth in a cast $AlSi_7Cu_3Mg$ aluminum alloy during cyclic mechanical loading at temperatures relevant for service conditions using this X-ray synchrotron tomography. 3D renderings of the development of damage inside the specimen without mechanical loading and after 20 cycles are compared in Figure 13. The analysis of the 3D images reveals the micro-mechanisms of crack initiation and propagation *[S. Dezecot et al. (2016)]*.

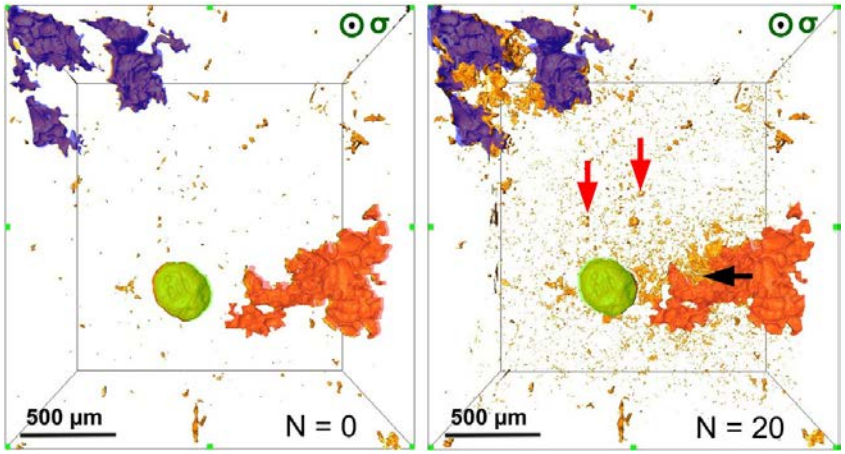

a) *b)*

Figure 13. 3D rendering of the development of damage inside the specimen: a) without mechanical loading; b) after mechanical loading of 20 cycles. The horizontal arrow shows the location of the crack visible in 2D slice. Vertical arrows point at the cracks observed at the level of Si particles. Purple, green and orange areas correspond to initial pores

X-ray tomography is principally used to study the microstructure and damage mechanisms in the materials with specifications for the resolution of micrometer, which are required for materials science applications. In recent years, the resolution has largely improved with the development of synchrotron beam lines. X-ray tomography has successfully performed to investigate the initial microstructure like inclusions, pores, and grains at a suitable resolution on varied materials, such as alloys, a metallic foam and particular metal matrix composites *[E. Maire, et al. (2007)]*, *[J. Adrien, et al. (2007)]*. Especially, the evolution of internal structure during the deformation could be studied as well when combined with *in situ* tensile or compression experiments *[G. Schmid, et al. (2016)]*.

1.3.2 SEM-based tomography

In comparison with the classical tomography methods X-ray tomography for the specimen range from millimeter to micrometer, and transmission microscopy tomography with nanometer resolution, SEM-based techniques fills the tomography resolution gap, as the resolution ranges between about 10 nm and 500 nm. Conventional SEM images the surface of a bulk sample with information from secondary electrons or backscattered electrons, which is insufficient to reconstruct a 3D microstructure. Therefore, SEM is generally not concerned as a possible technique for tomography. However, by combining some special techniques, 3D characterization could still be carried out based on SEM. One can cite for example, focused ion beam (FIB/SEM) tomography *[A. J. Kubis et al. (2004)]*, serial block face SEM *[J. J. Mancuso, (2012)]* or tomography in STEM-in-SEM using a specific rotating stage.

1.3.2.1 SEM surface tomography

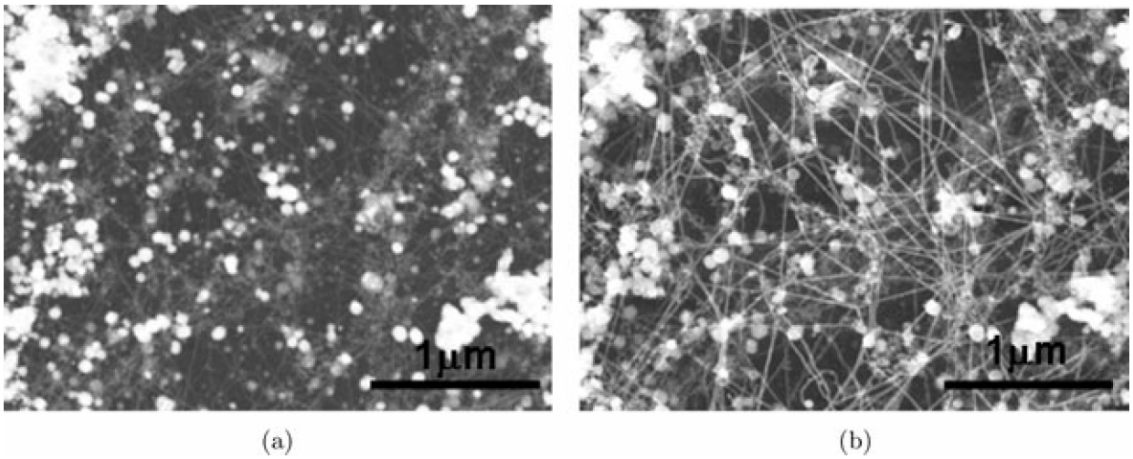

Figure 14. STEM dark field and SEM secondary electron images taken from the same intracellular location. (a) STEM dark field image at 30 kV. (b) SEM image at 30 kV [S. Lück et al. (2010)]

In some cases, the volume-dependent transmission electron signal yields rather low contrast in comparison to the surface-dependent secondary electron signal. An example is illustrated in Figure 14, which shows STEM and SE images on intermediate filament (IF) network in pancreatic cancer cells at the same acceleration voltage of 30 kV. STEM images provide a rather low signal of IFs in comparison to the strong signal of non-IF cytoplasmic leftovers

after extraction of the cells, while secondary electron imaging enhance the signal of IFs *[S. Lück et al. (2010)]*.

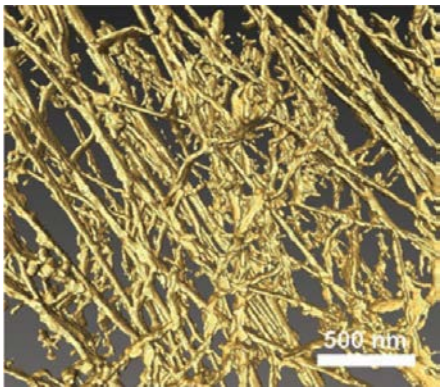

Figure 15. Reconstruction of SEM tilt series on intermediate filament network in pancreatic cancer cells. [S. Lück et al. (2010)]

As the single filaments show good contrast in secondary electron images under most tilt angles, surface tomography has been performed with a Hitachi S-5200 in-lens SEM (Tokyo, Japan) at an acceleration voltage of 5 kV using the secondary electron signal. An experimental limitation was due to the maximum tilt of 40° for the SEM stage, thus the samples were mounted on a pretilted (35°) holder. Firstly, the tilt series was acquired from + 60° to 0°. Then, after rotation of the sample by 180°, the second part of the tilt series (from 0° to - 60°) was then obtained. SEM tomograms (see Figure 15) were reconstructed by weighted back projection (WBP) with the IMOD software. The 3D structure of filaments seems to be well reproduced in this secondary electron tomogram.

A similar SEM tomography on an Argentine ant has been performed by J. D. Woodward et al. *[J. D. Woodward et al. (2010)]* in a LEO S440 SEM. This biological sample was first freeze-dried at -90°C for two hours, and then coated with Gold-Palladium at room temperature. After the acquisition of fifty micrographs from the surface of the glued ant with a 7.2° increment for a full rotation (360°), the stage with sample then was tilted in its plane, and a further fifty micrographs were obtained by rotation. This corresponds to the conical tomography geometry represented in Figure 16b *[S. Lanzavecchia et al. (2005)]*.

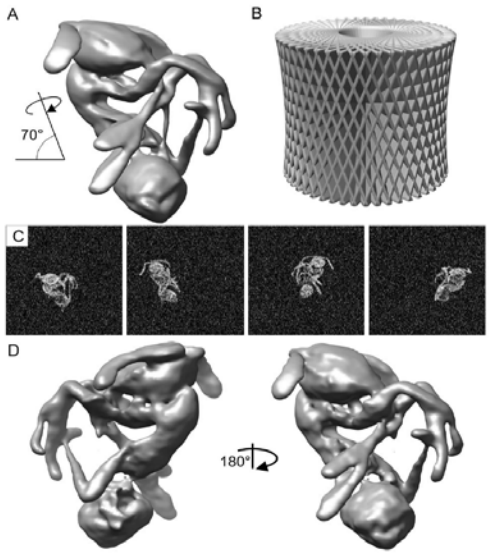

Figure 16.SEM tomography on an Argentine ant. (A). the reconstruction derived from the complete dataset, the second series was acquired with a stage rotation by approximately 70° from the horizontal. (B). representation of conical tilt geometry, the Fourier transform of each image represents a central section perpendicular to the viewing direction. The ‘‘missing cone’’ is the empty region at either end, the presence of which limits the achievable resolution. By increasing the tilt angle to 70° this region is greatly diminished. (C). the images used in the reconstruction were low-pass Fourier filtered to 5 pixels and noise was added using Matlab v6.5 (Mathworks Inc). (D). the reconstruction results. The second (rotated) image is in the same orientation as (A), with the same basic geometry [S. Lanzavecchia et al. (2005)]

When comparing this technique with other nondestructive tomography methods, the sample preparation for SEM surface tomography is not so difficult. Indeed, no requirement is needed for thin samples which could be transmitted by the electron beam. Moreover, because the series are acquired on the sample surface, a full rotation (360°) of the sample of appropriate geometry seems to be possible. On the contrary, there are some limitations for the same reason: the resulting tomogram cannot reveal internal details, unless the structures of interest lie close enough to the surface of this sample *[J.D. Woodward et al. (2009)]*.

1.3.2.2 FIB/SEM tomography

3D imaging in this range could also be performed by FIB tomography *[A. J. Kubis, et al. (2004)]*. Focused Ion Beam instrument was first used for device machining or specific sample

preparations at a micrometer or sub-micrometer scale *[C. G. Talbot, (1996)] [K. Gamo, (1996)]*, then adapted for producing thin sections of the samples for TEM observations. During the last decade, FIB enriched its use to imaging by combining its ion beam with the electron beam of SEM, which is called dual-beam or double-column system. FIB tomography could be carried out using this FIB/SEM system *[R. Krueger, (1999)] [R. K. Bansal, et al. (2006)] [N. Jeanvoine, et al. (2008)]* by the visualization of slices. The ion beam mills the region of interest slice by slice. Images are recorded after each slice milling, as in conventional SEM. At the end, the volume is directly obtained from all the images, after alignment.

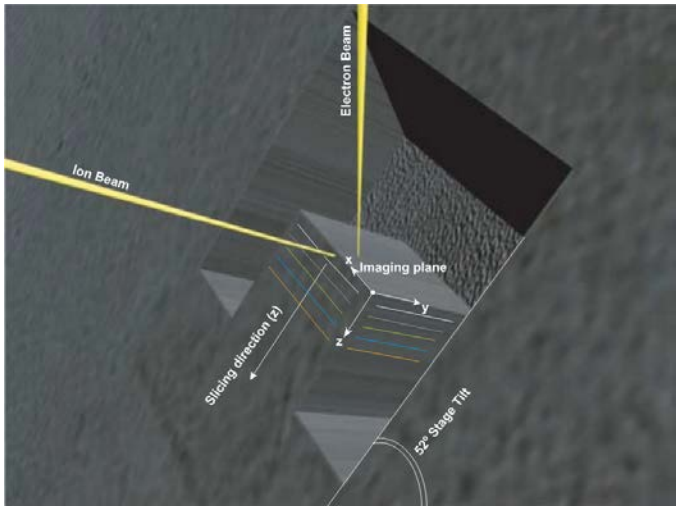

Figure 17. Illustration of the sample cube geometry, optimized for FIB serial sectioning with a dual beam FIB/SEM machine [L. Holzer et al. (2004)]

The detailed set-up is given in Figure 17. The sample stage should first be tilted by 52°, which is the angular difference between the ion beam and the electron beam. This angle could be slightly different, depending on the microscope geometry. With this inclination, the surface of the sample (x-z plane) could be perpendicular to the direction of the incident ion beam, which allows the ion beam to mill a thin slice parallel to the imaging plane of the sample. After each milling, the fresh imaging plane could be polished with ion current lower than what is used for rough milling, which insures a smooth imaging plane for electron beam.

For conventional SEM imaging, the electron beam should be perpendicular to the surface of the sample. However for FIB/SEM tomography, the sample is tilted by 52° so as to be well

oriented with respect to the ion beam, therefore the incident electron beam makes an angle of 38° with the imaging plane. Thus the SEM images have to be corrected. Besides, the focus in each image changes with the variation of working distance WD after the milling of each slice. In practice, the system could actualize automatically the WD according to the known thickness of the layer erased during the milling process.

In FIB tomography, one slice corresponding to one image could be considered as being composed of a certain number of voxels (*i.e.* volume pixels). A regular stack of images being produced by serial sectioning, it can directly be transformed into a voxel-based volume. Ideally, the thickness of eroded layers should have dimensions similar to the pixel resolution in the x-y plane (also called lateral resolution, linked to the magnification / numerical resolution of the SEM images, approximately equal to 10 nm). Generally, the lateral resolution is smaller than the depth resolution in the slicing direction, which is defined by the expected constant thickness of the erased slices.

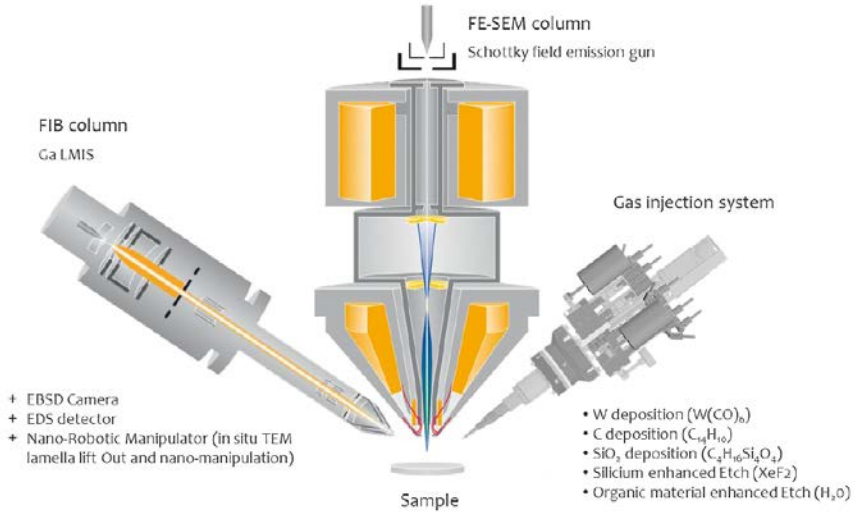

Figure 18. The configuration of Zeiss NVision 40 FIB/SEM at CLYM

In addition, modern FIB tomography with different detection modes has the ability to simultaneously acquire microstructural (BSE), chemical (EDX) and crystallographic (EBSD) information from the same sample. These 3D-imaging abilities offer new approaches for microstructural characterizations in the field of materials, environmental, geographic and life

sciences. Figure 18 displays the general configuration of the Zeiss NVision40 FIB/SEM installed at Consortium Lyon-Saint Etienne de Microscopie (CLYM). Besides the main parts, FE (field emission) – SEM electron column, FIB ion column with liquid metal ion source (LMIS), this machine is equipped with a EDX detector for chemical analysis and a EBSD camera for crystallographic characterization as well. Various gases can also be introduced with a gas injection system (GIS) for some *in situ* experiments. Two nano-robotic manipulators are available for some special operations, such as TEM specimen preparation, nano-machining.

An advantage for FIB tomography lies in the fact that there is theoretically almost no volume restriction except the real size of the sample, as the length in the slicing direction is not really limited *[M. Kato et al. (2007)]*. However, this tomography technique itself has already required long acquisition times, a dozen hours per sample generally, with longer times needed for the acquisition of large volumes. Moreover, preparing a long isolated zone of interest may also need a significant amount of time. During this long process (up to several days) of image acquisition, various problems may occur: loss of focus, drift of the sample, environmental issues (electromagnetic stray fields) *[L. Holzer et al. (2006)]*, which may affect the image stack. Consequently, post-processing as realignment is required for a nice reconstruction. Besides, during the process of FIB serial sectioning, artifacts related to amorphisation or redeposition of the material may occur. In this case, the tomography results could not precisely present the structure of the analyzed material *[L. Holzer, M. Cantoni (2012)]*. Good examples of this limitation are solid oxide fuel cells (SOFC) or solid oxide electrolysis cells (SOEC) which have a complex multilayered, multi-phase structure since they are made of various highly absorbing ceramic and metal materials *[N. H. Menzler, et al. (2010)]*.

When comparing FIB/SEM with other tomography techniques, FIB tomography combines relatively well the requirements for the target resolution and volume size. Although this destructive tomography technique still suffers from a few limitations, such as time-consuming stack acquisition, 3D-data processing, it opens new possibilities for 3D microstructural investigations in different fields with the synchronous acquisition of different analytical information (BSE, EDX, EBSD).

1.3.2.3 Serial block-face SEM

Another SEM-based technique is serial block-face scanning electron microscopy (SBFSEM). This technique is convenient, especially to determine the 3D geometry of cellular structures in biological fields. Serial block-face SEM provides a streamlined and automated 3D data acquisition process, where the surface of the sample is cut *in situ* by a microtome equipped with a diamond knife. This completely automated technique gains the advantage over serial sectioning by ultramicrotomy. Indeed, serial sectioning using ultramicrotomy followed by TEM observations requires to cut sections manually, and then to gather data. It is thus seriously time-consuming and prone to human error *[K. M. Harris (1999)]*, *[J. G. White et al. (1986)]*, *[G. E. Soto et al. (1994)]*. Serial block-face imaging avoids not only the risk of losing sections, but also the acquisition of distorted image sections due to alignment problems *[W. Denk, H. Horstmann. (2004)]*. Furthermore, it could also be used in some other surface-imaging techniques, such as in multi-photon microcopy *[W. Denk et al. (1990)]*, in light microscopy *[A. Odgaard et al. (1990)]*, *[A. J. Ewald et al. (2002)]*.

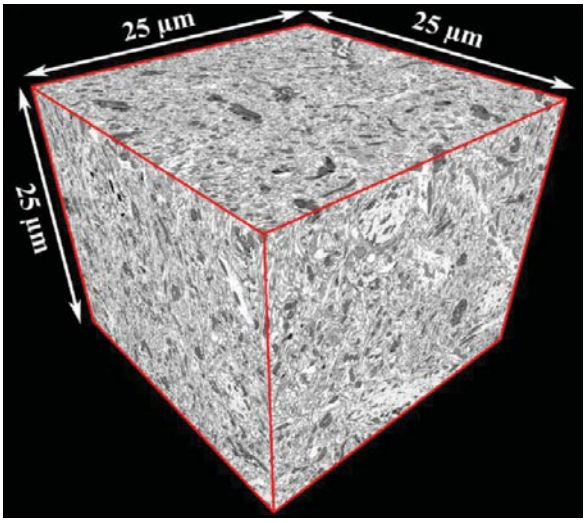

Figure 19. A 15,625µm³ volumetric data set containing 500 serial images of mouse brain [J. J. Mancuso, (2012)]

Recently, serial block-face SEM has greatly improved: the thickness of one slice could be as low as 2.5 nm for material samples such as aluminum alloys, and 7 nm for plastic embedded biological samples *[J. J. Mancuso, (2012)]*. Thinner sections require operating at lower

acceleration voltages, which decreases the charging effect, and further improves the quality of the SEM images. Figure 19 shows an example of serial block-face SEM reconstruction volume on mouse brain using 3View® installed on a FEI Quanta™ 200 FEG SEM *[J. J. Mancuso, (2012)]*.

This SEM-based tomography technique is practical for large volume acquisitions, thanks to its large field of view having a wide span on dimension ranges from a millimeter (10^{-3} m) to the nanometer (10^{-9} m). When imaging from secondary electrons or backscattered electrons, SEM provides high contrast image series with excellent signal-to-noise ratio (SNR), and further results in nice tomograms. Therefore, this SEM-based tomography is attractive especially for biological samples. Nevertheless, in materials science, it can only be applied on the materials which can be cut with a diamond knife, at room temperature.

1.3.2.4 Tomo-STEM

Although FIB/SEM tomography has successfully been used for studying the microstructure of bulk materials, this destructive and time-consuming technique still has much limitation in many cases. Moreover, as seen in the previous section, SBFSEM can be applied on materials which can be cut at room temperature. A tomography approach on STEM-in-SEM may overcome the limitations of FIB/SEM tomography and SBFSEM.

The acceleration voltage in a SEM, much lower than that in a TEM with typically 30 keV at maximum, is generally thought to be too low to allow the penetration of electrons over large thicknesses. Even so, low-voltage STEM or STEM-in-SEM *[P. Merli et al. (2003)]* is still possible. There is thus a good probability that STEM tomography could also be performed in SEM.

It has recently been reported that STEM tomography in an ESEM (FEI XL30), equipped with a transmitted electrons detector placed below the sample, could provide 3D microstructure information on large volumes with high resolution *[P. Jornsanoh et al. (2011)]*. This new electron tomography technique based on the combination of STEM and ESEM was called ‘‘tomo-STEM®’’.

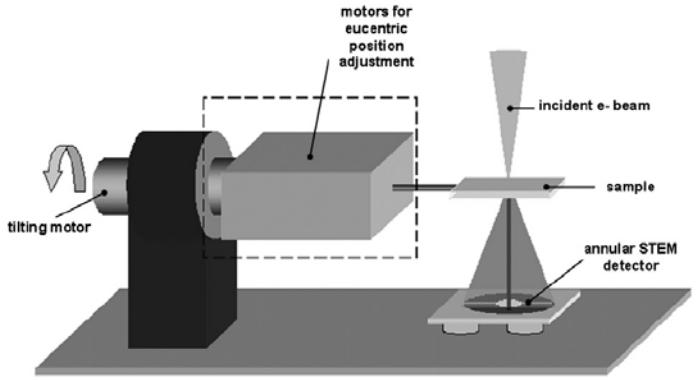

Figure 20. Tomo-STEM® stage for the electron tomography technique combining STEM and ESEM [P. Jornsanoh et al. (2011)]

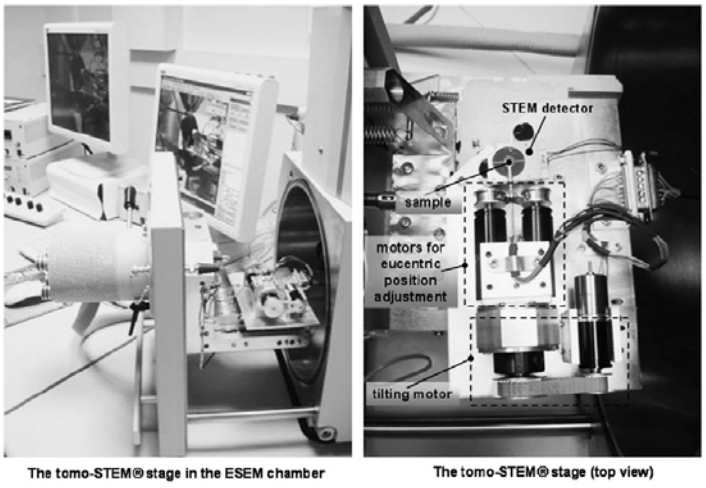

Figure 21. Different views of the tomo-STEM® stage in ESEM chamber [P. Jornsanoh et al. (2011)]

This tomo-STEM experiments could be performed mainly thanks to a special home-made device shown in Figure 20. The transmission imaging mode benefited from a previous work, the so-called 'wet-STEM' in ESEM *[A. Bogner et al. (2005)]* with an annular STEM detector below the sample to collect the scattered electrons. In order to obtain images at different angles, a tilting motor is introduced, which allows the sample rotation around the horizontal axis up to 360° with a theoretical accuracy better than 0.1°. Besides, two motors are used to place the sample at the eucentric position and therefore to maintain the area of interest in the field of view during the tilting process. Figure 21 presents different views of this first prototype installed in the ESEM, thanks to the large sample chamber.

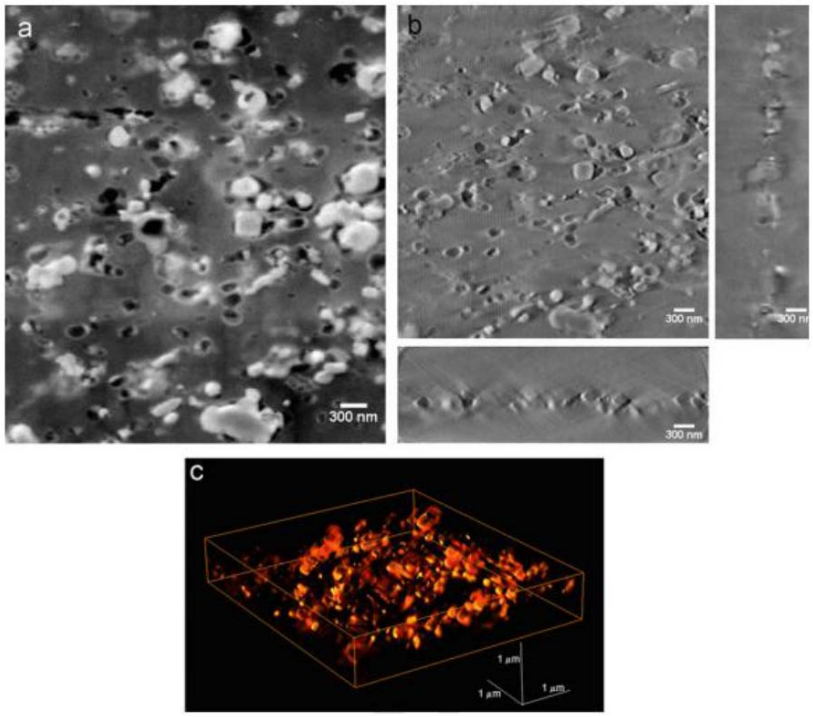

Figure 22. a) STEM image at 0°; b) tomogram XY, XZ and YZ slices and c) reconstructed volume (4.2 × 4.8 × 0.8 µm^3) of impact-resistant poly (vinylchloride) [P. Jornsanoh et al. (2011)]

Performing the experiments in an ESEM chamber enables the characterization of non-conductive specimens and low-atomic number materials, like polymers, with a good contrast. Figure 22 gives the example of a tomographic reconstruction from tilted images series from -67° to + 67° with an increment of 1°. The specimens is a 500 nm thick polymer composite, which consists of a unstained PVC (poly (vinylchloride)) matrix filled by a variety of micronic and sub-micronic $CaCO_3$, TiO_2 and shock modifiers particles.

Tomo-STEM opens a new window for tomography on large volumes with high resolution without destroying the samples. When working in ESEM mode, some materials like polymers can be satisfied even for a relatively thick sample, up to several hundreds of nanometers. However, limited by the geometry of the TEM grid, the samples supported by the grid usually only tilt with the range of ± 70°. These missing projections can lead to artifacts in the reconstruction results. This could be overcome when working on needle-shaped samples, as shown by P. Jornsanoh *et al. [P. Jornsanoh et al. (2011)]*.

A new prototype, based on piezoelectric elements, has been built afterwards. This new system also contains two Peltier stages which can cool down the sample. First experiments have demonstrated the ability to condense water on the sample and to acquire tilted image series in the wet state. However, some evaporation was observed during the acquisition and was attributed to irradiation damage or temperature instability. Therefore, the series contained only a few images and specific algorithms had to be used *[K. Masenelli-Varlot et al. (2014)]*.

1.3.3 TEM tomography

TEM tomography, carried out in a transmission electron microscopy with spatial resolution in the nanometer range, is the most conventional electron-based means to study the 3D structure of samples in both materials science *[C. Baldock et al. (2002)]*, *[H. Jinnai, and R. J. Spontak (2009)]* and life science *[R. I. Koning, and A. J. Koster (2009)]*, *[K. Aoyama et al. (2008)]*. The 3D image data is acquired from tomographic reconstruction of transmission images series with samples tilting over an as large as possible angular range at as small as possible tilt increments *[W. Baumeister et al. (1999)]*, *[P. A. Midgley, and M. Weyland (2003)]*.

Conventional TEM (CTEM) tomography is performed with a set of bright-field (BF) images. Bright-field images are formed with the transmitted beam, with most of the scattered electrons being blocked by an objective aperture. In the case of amorphous materials, dark areas in the resulting image are representative of a higher density or thicker region than bright areas. In crystalline samples, the dark areas correspond to the regions which give rise to diffraction. The so-called “bright field” means that the brightest areas correspond to the regions where there is no specimen. CTEM tomography has been used widely on biological specimens. In this case, BF images could be formed either from stained sections, where amplitude contrast is dominant, or unstained sections where phase contrast is presiding. On the contrary in materials science, BF images often contain unwanted diffraction contrast and Fresnel contrast that will result in artifacts in the reconstruction *[M. Weyland, et al. (2006)]*. Thus it may be applied to amorphous materials if Fresnel diffraction is not too important *[C. Baldock, et al. (2002)]*, but it is not suiTable to crystalline materials.

One alternative technique to overcome the limitation of conventional BF images is energy-filtered transmission electron microscopy (EFTEM) tomography, which forms images nearly without diffraction contrast and Fresnel contrast. An imaging filter is used to select only either elastic scattering electrons to increase the contrast of BF images, or inelastic scattering to produce elementary mapping. In both cases, the contrast exhibits roughly a monotonic mass-thickness relationship *[R. D. Leapman, et al. (2004)]*, *[P. A. Midgley, M. Weyland. (2003)]*.

Another alternative to CTEM tomography is 3D imaging in the STEM mode. As explained before, depending on the scattered angles, the transmitted electrons could be collected by different detectors below the specimens: bright field (BF), annular dark field (ADF), high angle annular dark field (HAADF). This give rise to several STEM tomography modes *[J. Loos, et al. (2009)]*, *[H. Friedrich et al. (2005)]*. Furthermore, high-resolution STEM could be combined with nano-diffraction, atomic resolution electron energy loss spectroscopy (EELS) and nanometer resolution X-ray energy dispersive (EDX) spectroscopy *[S. Utsunomiya and R. C. Ewing (2003)]*, *[Liu J. (2005)]*.

In STEM, the transmitted electrons with scattering angles close to zero could be collected by a bright field detector. The resulting image is similar to that of the BF image in CTEM. Thanks to the absence of imaging lenses after the specimen, STEM tomography can be performed even on thick specimens (a few micrometers) without the deleterious effect of chromatic aberration, which results in a blurring of the micrograph and loss of resolution in CTEM. As an example, a 3D reconstruction on micrometer-thick sections of beta cells from mouse pancreatic islet has been performed with optimized axial bight-field detector in STEM by A. A. Sousa *et al. [A. A. Sousa, et al. (2011)]*. The quality of these resulting tomograms is comparable to that obtained on much thinner (300 nm) sections in CTEM tomography. This STEM tomography mode overcomes the thickness limitation in CTEM (300-400 nm), and thus enables the 3D characterization on more complex and larger structures, while maintaining adequate resolution and signal-to-noise ratio (SNR) in the resulting tomograms.

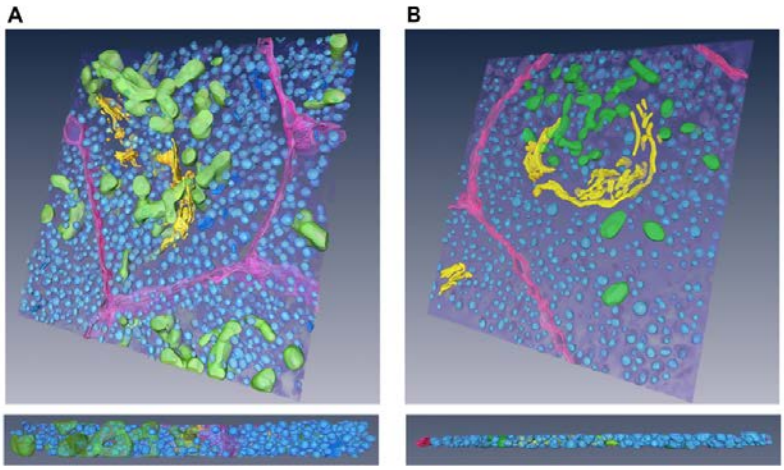

Figure 23. 3-D tomographic models from thin and thick sections of pancreatic beta cells. (A) Surface-rendered model derived from axial STEM reconstruction of 1-µm thick section. (B) Model derived from conventional ET reconstruction of 300-nm thick section. Insulin granules are rendered blue; Golgi complex, yellow; mitochondria, green; and plasma membrane, purple [A. A. Sousa, et al. (2011)]

An annular dark field (ADF) detector in STEM mode could be used to only collect electrons scattered above a certain angle. ADF-STEM imaging offers several advantages for tomography over bright field images in CTEM. The ADF-STEM signal intensity varies monotonically with the specimen mass-thickness, thus fulfilling the so-called "projection criterion" *[C. Kübel, et al. (2005)]*. The ADF-STEM images contains no more artifacts inherent to coherent imaging (e.g., Fresnel fringes, contrast reversal, or weak contrast at low spatial frequency) *[E. Sourty, et al. (2009)]*. ADF-STEM tomography is better suited for the analysis of low electron scattering materials like polymers, and especially for multiphase structures such as block copolymers, polymer blends or polymer composites filled with carbon nano-fillers (e.g., carbon black, carbon nanotubes, or graphene). Recently, reconstructed volumes obtained with BF-CTEM tomography and ADF-STEM tomography have been compared on a well-defined carbon black (CB) filled polymer nanocomposite with a known CB volume concentration. Both imaging methods provide a good contrast between the CB particles and the surrounding polymer matrix. However, the CB volume concentration measured in BF-CTEM tomograms exceeds by about 40% the concentration actually used to synthesize the composite, whereas the one measured in ADF-STEM tomograms gives a good

approximation. ADF-STEM tomography seems therefore more reliable for volume quantification like filler concentration and distribution in polymer nanocomposite systems *[K. Lu, et al. (2010)]*.

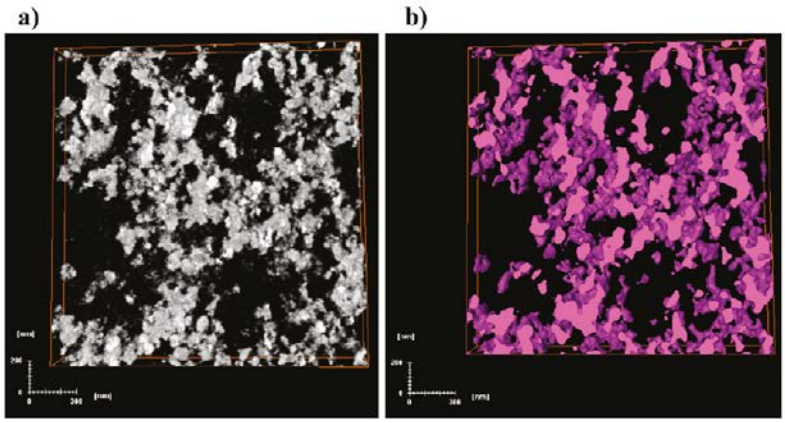

Figure 24. a) ADF-STEM tomography volume reconstruction showing the CB particles only and b) the corresponding surface rendering of the CB phase [K. Lu, et al. (2010)]

An incoherent STEM image could also be obtained by collecting electrons scattered between high angles with a high-angle annular dark field (HAADF) detector, which has an inner radius ideally beyond Bragg scattering angles and so collects principally incoherent scattered electrons. HAADF-STEM imaging has some advantages on further 3D characterization of polymer systems like high signal-to-noise ratio. It is also insensitive to differences in crystallinity within the polymer phase and is less prone to artifacts due to defocus effects *[J. C. Hindson et al. (2011)]*. Staining is not needed because the contrast is already sufficient for tomography, thus avoiding the artifacts from staining. The images formed in HAADF-STEM have a sufficient contrast on different polymer systems, such as polymer solar cell, rubber blend, carbon black filled conductive nanocomposite, semicrystalline polyethylene *[J. Loos, et al. (2009)]*.

In conclusion, tomography in Transmission Electron Microscopy has already been proved to be an efficient tool to investigate the interior structure at high resolution for both material, such as polymers, and biological specimens. However, it is only applicable to relative thin samples (≤1000 nm even in STEM mode), and this thickness restriction contradicts the requirement of larger volumes. For heterogeneous materials, the reconstructed volume in thin

sections may not be representative of the average internal structure. Besides, the 2D projections should ideally be obtained with a rotation amplitude of 180° and a tilt step of 1° or even 0.5°, but it is not always possible due to the limitation in the practical experimental conditions and the requirement for short irradiation times, especially for soft materials such as polymers and PNCs. Then the missing tilt range could lead to blurred reconstruction results.

1.3.4 Atom probe tomography

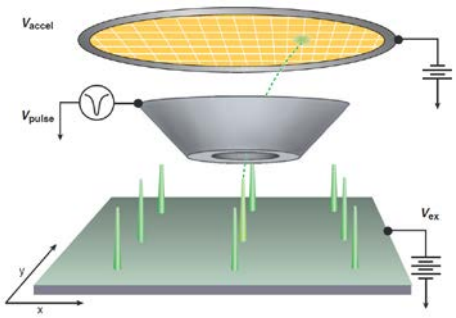

Figure 25. Scheme of a 3-D local-electrode atom-probe (LEAP) tomography. The substrate is maintained at a positive potential, V_{ex}, which supports the specimen; the substrate can be translated in the x-y plane to scan from specimen to specimen. The local electrode is pulsed with a negative voltage, V_{pulse}, to increase the electric field (E) at a specimen to the requisite value to field evaporate atoms as ions [D. N. Seidman, (2007)]

Atom probe tomography (APT) satisfies the requirement for 3D materials characterization with the best spatial resolution (at the atomic level). APT permits to reconstruct the atom positions of a crystalline specimen in three dimensions along with their chemical identities.

The atom probe produces a sequence of the atomic coordinates and the mass-to-charge state, m/n, of each ion collected. The experiment data is then reconstructed into a truncated cone, reconstructed volume, in which the radius increases during the experiment due to the taper angle of the needle-shaped specimen. The first atom probe was conceived as a field ion microscope (FIM) equipped with a time-of-flight mass spectrometer. In this way the observed surface atoms could individually be chemically identified *[E.W. Müller, (1951)]*, *[E.W. Müller, et al. (1968)]*. Recently, local-electrode atom-probe (LEAP) was developed and commercially introduced featuring a local electrode in close proximity to the specimen *[T. F. Kelly, M. K.*

Miller, (2007)], *[D. N. Seidman, (2007)]*. With LEAP tomography, the results could be obtained in significantly shorter times with larger volumes, which represents a great improvement over conventional APT.

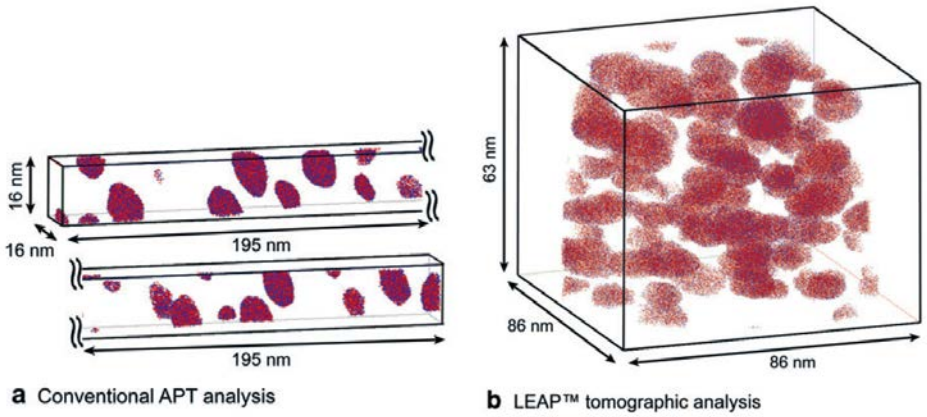

Figure 26. Specimens of Ni–5.2 Al at. %–14.2 Cr at. % aged at 873 K for 256 h were analyzed with (a) conventional APT and (b) LEAP^{TM} tomography. The 16×16×195 nm^3 (4.99×10^4 nm^3) and 86×86×63 nm^3 (4.66×10^5 nm^3) volumes contain approximately 1.8×10^6 and 9.8×10^6 atoms, respectively. Only Al (red) and Cr (blue) atoms within γ'-precipitates are displayed for the sake of clarity. Each dot represents a single atom [C. K. Sudbrack et al. (2006)]

Figure 26 compares the reconstructed volumes between classical APT analysis and LEAP tomography in a model Ni-Al-Cr superalloy *[C. K. Sudbrack et al. (2006)]*. The analyzed volume from LEAP may be greater than 200×200×200 nm^3 or 8 ×10^6 nm^3. On the contrary, the typical analyzed volume with conventional APT is limited to 15×15×100 nm^3 or 22,500 nm^3.

The traditional method for the preparation of the needle-shaped atom probe specimens involves electropolishing techniques *[M. K. Miller, (2000)]*, which are unfortunately not effective for most non-metallic materials. Recently, FIB-based methods have been developed to expand the applications of APT from structural metals and alloys to thin multilayer films on planar substrates, dielectric films, semiconducting structures and devices, and ceramic materials. *[M. K. Miller et al. (2007)]*.

Tomography techniques of all types are needed, but among these methods, atom probe tomography is uniquely positioned to fulfill a crucial need at the finest scale at the atomic scale with high analytical sensitivity. These years, APT has developed fantastically with new hardware configurations that greatly simplify the technique and improve the rate of data acquisition. However, all analytical techniques have their limitations. APT is still be limited by the reduced analyzed volume. The largest field of view in spatial units is only about 200 nm. Besides, up-to-date APT could not detect all atoms, but commonly sees only about 60%. Specimen fracture in the areas with a weak link is easily caused by high mechanical stress, which results in bad data acquisition. Specimen preparation techniques still need to be improved to obtain mirotips rapidly and automatically.

Table 2. Comparison of different tomography techniques

	Resolution	Field of view	Destructive technique	Analyzing liquid samples
X-ray tomography	> 500 nm	> 1 mm	No	No
SEM surface tomography	10 nm-500 nm	10 µm-1mm	No	No
FIB/SEM tomography	10 nm-500 nm	10 µm-1mm	Yes	No
Serial block-face SEM	10 nm-500 nm	10 µm-1mm	Yes	No
Tomo-STEM in ESEM	1 nm-500 nm	500 nm-10 µm	No	Yes
TEM tomography	0.5 nm-10 nm	100 nm-10 µm	No	Yes
Atom probe tomography	<1 nm	10 nm-200 nm	Yes	No

As a conclusion, Table 2 gives a simple comparison of different tomography techniques as destructive/non-destructive and in terms of resolution, field of view. The study of liquid samples is also evaluated.

1.4 This PHD work

The observation of liquid materials with nanometer resolution can be realized using dedicated specimen holders either in TEM or SEM, or with dedicated microscopes (ESEM). Thanks to the transmission mode, the information in the image is not limited anymore to the smooth surface of the colloidal solution or to some particles emerging from this liquid phase. On the contrary, it is possible to analyze objects deep inside a liquid layer. However, it is very difficult to understand the images in the case of piled-up particles. In this case, volume information from tomography is required.

Sealed liquid cells has become predominant for TEM observations on liquid materials, since they allow *in situ* studies, with a good stability (no evaporation or condensation), and a relatively controlled water film thickness. Indeed, the electrons have to pass through an increasing thickness of silicon nitride membranes in addition to the increasing thickness of the water film when the sample rotate at high angles. The thick support, surrounding the electron transparent window, may also hide the region of interest when tilting the sealed cell.

Therefore, wet-STEM in ESEM may be the best choice to analyze liquid specimens in 3D with nanometer resolution. This PhD work deals with the development of electron tomography on liquid suspensions using wet-STEM in ESEM. For this purpose, we will focus on aqueous suspensions.

Several issues first need to be solved to achieve this goal. First, the thickness of the water film can be tuned *in situ* by controlling the environment pressure and sample temperature. This is undoubtedly an advantage since water can be condensed or evaporated in situ, but it is also a drawback as the thickness of the water film remains unknown and its variations may lead to contrast inversions. Second, the equilibrium state might be difficult to keep for a time long enough to acquire a series of images for tomography. Indeed, water may condense or evaporate, and irradiation damage may occur.

In the following chapters, we will try to address these issues in details. After having described the materials and techniques used in this PhD work (chapter 2), we will study the relationships

between contrast and water film thickness, by combining 2D experimental images and Monte-Carlo simulations (chapter 3). Then in chapter 4, we will present our first results gained on the existing 3D stage. By analyzing the images and volumes, we will propose several improvements of the device and of the experimental protocol. Finally in chapter 5, we will use the optimized set-up and conditions to carry out a study of the 3D arrangement of latex particles in water. Our tomography results will be compared with images obtained by other techniques.

References

A. Al-Amoudi, L. P.O. Norlen, and J. Dubocheta. Cryo-electron microscopy of vitreous sections of native biological cells and tissues. Journal of Structural Biology 148, (2004), 131-135

A. A. Sousa, A. A. Azari, G. Zhang, R. D. Leapman. Dual-axis electron tomography of biological specimens: Extending the limits of specimen thickness with bright-field STEM imaging. Journal of Structural Biology 174, (2011), 107-114

A. Bogner, G. Thollet, D. Basset, P.-H. Jouneau, C. Gauthier. Wet STEM: A new development in environmental SEM for imaging nano-objects included in a liquid phase. Ultramicroscopy 104, (2005), 290-301

A. Bogner, P.-H. Jouneau, G. Thollet, D. Basset, C. Gauthier. A history of scanning electron microscopy developments: Towards ‘‘wet-STEM’’ imaging. Micron 38, (2007), 390-401

A. J. Ewald, H. McBride, M. Reddington, S. E. Fraser, R. Kerschmann. Surface imaging microscopy, an automated method for visualizing whole embryo samples in three dimensions at high resolution. Dev Dyn 225, (2002), 369-375

A. J. Koster, U. Ziese, A. J. Verkleij, A. H. Janssen, and de K. P. Jong. Three-Dimensional Transmission Electron Microscopy: A Novel Imaging and Characterization Technique with Nanometer Scale Resolution for Materials Science. J. Phys. Chem. B 104, (2000), 9368-9370

A. J. Kubis, G. J. Shiflet, D. N. Dunn, R. Hull. Focused ion-beam tomography. Metall Mater Trans A 35A, (2004), 1935-1943

A. L. Fletcher, B. L. Thiel and A. M. Donald. Amplification measurements of alternative imaging gases in environmental SEM. J. Phys. D: Appl. Phys. 30, (1997), 2249-2257

A. M. Donald. The use of environmental scanning electron microscopy for imaging wet and insulating materials. Nature Materials 2, (2003), 511-516

A. Odgaard, K. Andersen, F. Melsen, H. J. G. Gundersen. A direct method for fast 3-dimensional serial reconstruction. J. Microsc. 159, (1990), 335-342

C. Baldock, C. J. Gilpin, A. J. Koster, U. Ziese, K. E. Kadler, C. M. Kielty, D. F. Holmes. Three-dimensional reconstructions of extracellular matrix polymers using automated electron tomography. Journal of Structural Biology, 138, (2002), 130-136

C. G. Talbot. A new application-specific FIB system architecture. Microelectronic Engineering 30, (1996), 597-602

C. K. Sudbrack, K. E. Yoon, R. D. Noebe, D. N. Seidman. Temporal evolution of the nanostructure and phase compositions in a model Ni-Al-Cr superalloy. Acta Mater. 54, (2006), 3199-210

C. Kübel, A. Voigt, R. Schoenmakers, M. Otten, D. Su, T. C. Lee, A. Carlsson, J. Bradley. Recent Advances in Electron Tomography: TEM and HAADF-STEM Tomography for Materials Science and Semiconductor Applications. Microsc. Microanal. 11, (2005), 378-400

C. L. Smith. Basic Confocal Microscopy. Current Protocols in Neuroscience, (1997), 2.2.1-2.2.13

C. Rau, V. Crecea, W. Liu, C.-P. Richter, K. M. Peterson, P. R. Jemian, U. Neuhäusler, G. Schneider, X. Yu, P. V. Braun, T.-C. Chiang, I. K. Robinson. Synchrotron-based imaging and tomography with hard X-rays. Nuclear Instruments and Methods in Physics Research Section B: Beam Interactions with Materials and Atoms 261, (2007), 850-854

D. Alloyeau, W. Dachraoui, Y. Javed, H. Belkahla, G. Wang, H. Lecoq, S. Ammar, O. Ersen, A. Wisnet, F. Gazeau & C. Ricolleau. Unravelling kinetic and thermodynamic effects on the growth of gold nanoplates by liquid transmission electron microscopy. Nano Lett. 15, (2015), 2574-2581

D. B. Peckys, G. M. Veith, D. C. Joy & N. de Jonge. Nanoscale imaging of whole cells using a liquid enclosure and a scanning transmission electron microscope. PLOS one 4 (12) e8214, (2009)

D. B. Peckys, J. P. Baudoin, M. Eder, U. Werner & N. de Jonge. Epidermal growth factor receptor subunit locations determined in hydrated cells with environmental scanning electron microscopy. Scientific Reports 3, (2013), 2626

D. J. Stokes, B. L. Thiel & A. M. Donald. Direct observation of water-oil emulsion systems in the liquid state by environmental scanning electron microscopy. Langmuir 14, (1998), 4402-4408

D. J. Stokes. Environmental scanning electron microscopy (ESEM): principles and applications to food microstructures. Woodhead Publishing Limited, (2013)

D. J. Stokes. Progress in imaging in a gaseous environment: *in situ* techniques and applications using environmental SEM (ESEM). Microsc. Microanal. 18, (2012), 1070-1071

D. N. Seidman. Three-Dimensional Atom-Probe Tomography: Advances and Applications. Annu. Rev. Mater. Res. 37, (2007), 127-158

D. Roussel, A. Lichtner, D. Jauffrès, J. Villanova, R. K. Bordia, C. L. Martin. Strength of hierarchically porous ceramics: Discrete simulations on X-ray nanotomography images. Scripta Materialia 113, (2016), 250-253

D. Stokes. Principles and practice of variable pressure: environmental scanning electron microscopy (VP-ESEM). Wiley-Blackwell, (2008)

E. A. Ring, & N. de Jonge. Video-frequency scanning transmission electron microscopy of moving gold nanoparticles in liquid. Micron 43, (2012), 1078-1084

E. G. van Putten, D. Akbulut, J. Bertolotti, W. L. Vos, A. Lagendijk, and A. P. Mosk. Scattering Lens Resolves Sub-100 nm Structures with Visible Light. Physical review letters 106, (2011), 193905

E. Maire, J. Y. Buffière, L. Salvo, J. J. Blandin, W. Ludwig, and J. M. Létang. On the Application of X-ray Microtomography in the Field of Materials Science. Advanced Engineering Materials 3, (2001), 539-546

E. Maire, P. Colombo, J. Adrien, L. Babout, and L. Biasetto. Characterization of the morphology of cellular ceramics by 3D image processing of X-ray tomography. Journal of the European Ceramic Society 27, (2007), 1973-1981

E. P. W. Ward, T. J. V. Yates, J.-J. Fernández, D. E. W. Vaughan, and P. A. Midgley. Three-Dimensional Nanoparticle Distribution and Local Curvature of Heterogeneous Catalysts Revealed by Electron Tomography. J. Phys. Chem. C 111, (2007), 11501-11505

E. Sourty, S. van Bavel, K. Lu, R. Guerra, G. Bar, J. Loos. High-Angle Annular Dark Field Scanning Transmission Electron Microscopy on Carbon-Based Functional Polymer Systems. Microsc. Microanal. 15, (2009), 251-258

E. W. Müller, J. P. Panitz, S.B. McClane. The atom probe field ion microscope. Rev Sci Instrum 39, (1968), 83-6

E. W. Müller. The field ion microscope. Z Phys 131, (1951), 136-42

F. M. Ross. Opportunities and challenges in liquid cell electron microscopy. Science 350, (2015), 6267

F. M. Ross. Liquid Cell Electron Microscopy. Cambridge University Press, (2016)

G. E. Soto, S. J. Young, M. E. Martone, T. J. Deerinck, S. Lamont, et al. Serial section electron tomography: A method for three-dimensional reconstruction of large structures. Neuroimage 1, (1994), 230-243

G. Foray, S. Cardinal, A. Malchère & J. M. Pelletier. Mechanical Spectroscopy, a Tool to Characterize Cement Latex Composites. Solid State Phenomena 184, (2012), 399-404

G. Martinez-Criado, R. Tucoulou, P. Cloetens, P. Bleuet, S. Bohic, J. Cauzid, I. Kieffer, E. Kosior, S. Laboure, S. Petitgirard, A. Rack, J.A. Sans, J. Segura-Ruiz, H. Suhonen, Susini, J. Villanova. Status of the hard X-ray microprobe beamline Id22 of the European Synchrotron Radiation Facility. J. Synchrotron Rad 19, (2012), 10-18.

G. Möbus, B. J. Inkson. Nanoscale tomography in materials science. Mater Today 10, (2007), 18-25

G. Schmid, M. Obst, J. Wu, A. Hitchcock. 3D Chemical Imaging of Nanoscale Biological, Environmental, and Synthetic Materials by Soft X-Ray STXM Spectrotomography. DOI: 10.1007/978-3-662-48606-1_2, (2016), 43-94

G. Spina, G. Bonnefont, P. Palmero, G. Fantozzi, J. Chevalier, & L. Montanaro. Transparent YAG obtained by spark plasma sintering of co-precipitated powder. Influence of dispersion route and sintering parameters on optical and microstructural characteristics. Journal of the European Ceramic Society 32, (2012), 2957-2964

H. Friedrich, M. R. McCartney, and P. R. Buseck. Comparison of intensity distributions in tomograms from BF TEM, ADF STEM, HAADF STEM, and calculated tilt series. Ultramicroscopy 106, (2005), 18-27

H. Jinnai, and R. J. Spontak. Transmission electron microtomography in polymer research. Polymer 50, (2009), 1067-1087

H. Kano, S. Jakobs, M. Nagorni, and S.W. Hell. Dual-color 4Pi-confocal microscopy with 3D-resolution in the 100 nm range. Ultramicroscopy 90, (2002), 207-213

H. Zheng, S. A. Claridge, A. M. Minor, A. P. Alivisatos & U. Dahmen. Nanocrystal diffusion in a liquid thin film observed by in situ transmission electron microscopy. Nano Lett. 9, (2009), 2460-2465

I. M. Watt. The Principles and Practice of Electron Microscopy (2 ed.). Cambridge University Press, (1997)

J. Adrien, E. Maire, N. Gimenez, and V. Sauvant-Moynot. Experimental study of the compression behaviour of syntactic foams by in situ X-ray tomography. Acta Materialia 55, (2007), 1667-1679

J. B. Pawley. Handbook of Biological Confocal Microscopy (3rd ed.). Berlin: Springer, (2006)

J. C. Andrews, F. Meirer, Y. Liu, Z. Mester, P. Pianetta. Transmission X-ray microscopy for full-field nano imaging of biomaterials. Microsc. Res. Tech. 74, (2011), 671-681

J. C. Hindson, Z. Saghi, J.-C. Hernandez-Garrido, P. A. Midgley, and N. C. Greenham. Morphological Study of Nanoparticle-Polymer Solar Cells Using High-Angle Annular Dark-Field Electron Tomography. Nano Lett. 11, (2011), 904-909

J. Dubochet, M. Adrian, J.J. Chang, J.C. Homo, J. Lepault, A.W. McDowall, P. Schultz. Cryo-electron microscopy of vitrified specimens. Quarterly Review of Biophysics 21, (1988), 129-228

J. D. Woodward, and B. T. Sewell. Tomography of asymmetric bulk specimens imaged by scanning electron microscopy. Ultramicroscopy 110, (2010), 170-175

J. D. Woodward, R. Wepf, B. T. Sewell. Three-dimensional reconstruction of biological macromolecular complexes from in-lens scanning electron micro-graphs. J. Microsc. 234, (2009), 287-292

J. E. Evans, K. L. Jungjohann, N. D. Browning & I. Arslan. Controlled growth of nanoparticles from solution with in situ liquid transmission electron microscopy. Nano. Lett. 11, (2011), 2809-2813

J. Enderlein. Super-resolution optical microscopy: Seeing the smaller picture. Nature Nanotechnology 11, (2016), 737-738

J. Faucheu, L. Chazeau, C. Gauthier, J. Y. Cavaillé, M. Goikoetxea, R. Minari & J. M. Asua. Latex imaging by Environmental STEM: application to the study of the surfactant outcome in hybrid alkyd/acrylate systems. Langmuir 25, (2009), 10251-10258

J. G. Duckett, S. Pressel, K. M. Y. P'ng and K. S. Renzaglia. Exploding a myth: the capsule dehiscence mechanism and the function of pseudostomata in *Sphagnum.* New Phytologist 183, (2009), 1053-1063

J. Goldstein, D. Newbury, D. Joy, C. Lyman, P. Echlin et al. Scanning Electron Microscopy and X-Ray Microanalysis, 3rd edition, New York , (2003)

J. G. White, E. Southgate, J.N. Thomson, S. Brenner. The structure of the nervous system of the nematode *Caenorhabditis elegans*. Philos Trans R Soc Lond A 314, (1986), 1-340

J. J. Mancuso. Large volumes at high resolution using serial block face imaging in the SEM. Microsc Microanal 18(S2), (2012), 104-105

J. Liu. Scanning transmission electron microscopy and its application to the study of nanoparticles and nanoparticle systems. J. Electron Microsc (Tokyo) 54, (2005), 251-278

J. Loos, E. Sourty, K. Lu, G. de With, and S. v. Bavel. Imaging Polymer Systems with High-Angle Annular Dark Field Scanning Transmission Electron Microscopy (HAADF−STEM). Macromolecules 42, (2009), 2581-2586

J. M. Grogan, N. M. Schneider, F. M. Ross, H. H. Bau. The Nanoaquarium: a New Paradigm in Electron Microscopy. J. Indian Inst. Sci. 92, (2012), 295-308

J. M. Grogan, N. M. Schneider, F. M. Ross, H. H. Bau. Bubble and Pattern Formation in Liquid Induced by an Electron Beam. Nano Lett. 14, (2014), 359-364

J. Park, H. Elmlund, P. Ercius, J. M. Yuk, D. T. Limmer, Q. Chen, K. Kim, S. H. Han, D. A. Weitz, A. Zettl, A. P. Alivisatos. 3D structure of individual nanocrystals in solution by electron microscopy. Science 349, (2015), 290-295

J. P. Y. Tan, H. R. Tan, C. Boothroyd, Y. L. Foo, C. B. He, and M. Lin. Three-Dimensional Structure of CeO2 Nanocrystals. J. Phys. Chem. C 115, (2011), 3544-3551

J. R. Lawrence, G. D. W. Swerhone, J. J. Dynes, D. R. Korber & A. P. Hitchcock. Soft X-ray spectromicroscopy for speciation, quantitation and nano-eco-toxicology of nanomaterials. J. Microsc. 261, (2016), 130-147

J. Tan and F. Wang. Theoretical analysis and property study of optical focus detection based on differential confocal microscopy. Meas. Sci. Technol. 13, (2002), 1289-1293

J. Villanova, P. Cloetens, H. Suhonen, J. Laurencin, F. Usseglio-Viretta, E. Lay, G. Delette, P. Bleuet, D. Jauffrès, D. Roussel, A. Z. Lichtner, C. L. Martin. Multi-scale 3D imaging of absorbing porous materials for solid oxide fuel cells. J. Mater. Sci. 49, (2014), 5626-5634

J. Y. Huang, L. Zhong, C. M. Wang, J. P. Sullivan, W. Xu, L. Q. Zang, S. X. Mao, N.S. Hudak, X. H. Liu, A. Subramanian, H. Fan, L. Qi, A. Kushima & J. Li. In situ observation of the electrochemical lithiation of a single SnO_2 nanowire electrode. Science 330, (2010), 1515-1520

K. Aoyama, T. Takagi, A. Hirase, and A. Miyazawa. STEM tomography for thick biological specimens. Ultramicroscopy 109, (2008), 70-80

K. Gamo. Nanofabrication by FIB. Microelectronic Engineering 32, (1996), 159-171

K. Lu, E. Sourty, R. Guerra, G. Bar, and J. Loos. Critical Comparison of Volume Data Obtained by Different Electron Tomography Techniques. Macromolecules 43, (2010), 1444-1448

K. M. Harris. Structure, development, and plasticity of dendritic spines. Curr Opin Neurobiol 9, (1999), 343-348

K. Masenelli-Varlot, A**.** Malchère, **J.** Ferreira, H**.** H**.** Mezerji, S**.** Bals, C**.** Messaoudi and S**.** M**.** Garrido. Wet-STEM Tomography: Principles, Potentialities and Limitations**.** Microscopy and Microanalysis 20, (2014), 366-375

L. Holzer, B. Muench, M. Wegmann, P. Gasser, and R. J. Flatt. FIB-Nanotomography of Particulate Systems—Part I: Particle Shape and Topology of Interfaces. Journal of the American Ceramic Society 89, (2006), 2577-2585

L. Holzer, F. Indutnyi, P. H. Gasser, B. Münch, and M. Wegmann. Three-dimensional analysis of porous BaTiO3 ceramics using FIB nanotomography. J. Microsc 2016, (2004), 84-95

L. Holzer, M. Cantoni. Nanofabrication using focused ion and electrons beams: principles and applications, Chap. 11, Review of FIB- tomography. Oxford University Press, New York, (2012), 410-435

L. Salvo, P. Cloetens, E. Maire, S. Zabler, J. J. Blandin, J. Y. Buffière, W. Ludwig, E. Boller, D. Bellet, and C. Josserond. X-ray micro-tomography an attractive characterisation technique in materials science. Nuclear Instruments and Methods in Physics Research Section B: Beam Interactions with Materials and Atoms 200, (2003), 273-286

M. Almgren, K. Edwards, G. Karlsson. Cryo transmission electron microscopy of liposomes and related structures. Colloids and Surfaces A: Physicochemical and Engineering Aspects 174, (2000), 3-21

M. Dyba and S. Hell. Focal spots of size λ/23 open up far-field florescence microscopy at 33 nm axial resolution. Phys. Rev. Lett. 88, (2002), 163901

M. J. Booth. Adaptive optical microscopy: the ongoing quest for a perfect image. Light: Science & Applications 3, (2014), 1-7

M. Kato, T. Ito, Y. Aoyama, K. Sawa, T. Kaneko, N. Kawase, and H. Jinnai. Three-dimensional structural analysis of a block copolymer by scanning electron microscopy combined with a focused ion beam. Journal of Polymer Science Part B: Polymer Physics 45, (2007), 677-683

M. K. Miller. Atom probe tomography. New York, NY: Springer, (2000)

M. K. Miller, K. F. Russell, K. Thompson, R. Alvis, D. J. Larson. Review of atom probe FIB-based specimen preparation methods. Microsc Microanal 13, (2007), 428-36

M. Psenicka, M. Tesarova, J. Tesitel, J. Nebesarova. Size determination of *Acipenser ruthenus* spermatozoa in different types of electron microscopy. Micron 41, (2010), 455-460

M. Weyland, T.J.V. Yates, R.E. Dunin-Borkowski, L. Laffont, and P.A. Midgley. Nanoscale analysis of three-dimensional structures by electron tomography. Scripta Materialia 55, (2006), 29-33

N. de Jonge & F. M. Ross. Electron microscopy of specimens in liquid. Nature Nanotechnology 6, (2011), 695-704

N. H. Menzler, F. Tietz, S. Uhlenbruck, H. P. Buchkremer, D. Stöver. Materials and manufacturing technologies for solid oxide fuel cells. J. Mater Sci 45, (2010), 3109-3135

N. Jeanvoine, C. Holzapfel, F. Soldera, and F. Mücklich. Microstructure Characterisation of Electrical Discharge Craters using FIB/SEM Dual Beam Techniques. Advanced Engineering Materials 10, (2008), 973-977

N. M. Schneider, M. M. Norton. Electron-Water Interactions and Implications for Liquid Cell Electron Microscopy. J. Phys. Chem. C. 118, (2014), 22373-22382

N. Roos, A. J. Morgan. Cryopreservation of Thin Biological Specimen for Electron Microscopy: Methods and Applications. Oxford Science Publications, (1990)

P. A. Midgley, M. Weyland. 3D electron microscopy in the physical sciences: the development of Z-contrast and EFTEM tomography. Ultramicroscopy 96, (2003), 413-431

P. Jornsanoh, G. Thollet, J. Ferreira, K. Masenelli-Varlot, C. Gauthier, and A. Bogner. Electron tomography combining ESEM and STEM: A new 3D imaging technique. Ultramicroscopy 111, (2011), 1247-1254

P. J. Withers. Review: X-ray nanotomography. Mater Today 10, (2007), 26-34

P. Merli, V. Morandi, and F. Corticelli. Backscattered electron imaging and scanning transmission electron microscopy imaging of multi-layers. Ultramicroscopy 94, (2003), 89-98

P. Walter. High-resolution cryoscanning electron microscopy of biological samples. Biological Low-Voltage Scanning Electron Microscopy. Springer, (2008), 245-262

P. Yu, B. Cui & Q. Shi. Preparation and characterization of BaTiO3 powders and ceramics by sol–gel process using oleic acid as surfactant. Materials Science and Engineering: A, 473, (2008), 34-41

Q. Chen, J. M. Smith, J. Park, K. Kim, D. Ho, H. I. Rasool, A. Zettl & A. P. Alivisatos. 3D motion of DNA-Au nanoconjugates in graphene liquid cell electron microscopy. Nano Lett. 13, (2013), 4556-4561

R. D. Leapman, E. Kocsis, G. Zhang, T. L. Talbot, P. Laquerriere. Three-dimensional distributions of elements in biological samples by energy-filtered electron tomography. Ultramicroscopy 100, (2004), 115-125

R. I. Koning, and A. J. Koster. Cryo-electron tomography in biology and medicine. Annals of Anatomy - Anatomischer Anzeiger 191, (2009), 427-445

R. K. Bansal, A. Kubis, R. Hull, and J. M. Fitz-Gerald. High-resolution three-dimensional reconstruction: A combined scanning electron microscope and focused ion-beam approach. Journal of Vacuum Science & Technology B: Microelectronics and Nanometer Structures 24, (2006), 554

R. Krueger. Dual-column (FIB–SEM) wafer applications. Micron 30, (1999), 221-226

R. Leary, P.A. Midgley, J.M. Thomas. Recent advances in the application of electron tomography to materials chemistry. Acc Chem Res 45, (2012), 1782-1791

S. Dezecot, J. Y. Buffiere, A. Koster, V. Maurel, F. Szmytka, E. Charkaluk, N. Dahdahd, A. El Bartali, N. Limodin, J. F. Witz. In situ 3D characterization of high temperature fatigue damage mechanisms in a cast aluminum alloy using synchrotron X-ray tomography. Scripta Materialia 113, (2016), 254-258

S. Lanzavecchia, F. Cantele, P. L. Bellon, L. Zampighi, M. Kreman, E. Wright, G. A. Zampighi. Conical tomography of freeze-fracture replicas: a method for the study of integral membrane proteins inserted in phospholipid bilayers. J. Struct. Biol. 149, (2005), 87-98

S. Lee and D.-G. Gweon. Improvement of the axial resolution in confocal microscopy by the use of heterodyne interference. Meas. Sci. Technol. 19, (2008), 105502

S. Lück, M. Sailer, V. Schmidt, and P. Walther. Three-dimensional analysis of intermediate filament networks using SEM tomography. J. Microsc 239, (2010), 1-16

S. N. Gorb, D. Voigt, and E. V. Gorb. Visualisation of Small Fluid Droplets on Biological and Artificial Surfaces Using the Cryo-SEM Approach. Modern Research and Educational Topics in Microscopy, A. Méndez-Vilas and J. Díaz (Eds). (2007), 812-819

S. Utsunomiya and R. C. Ewing. Application of high-angle annular dark field scanning transmission electron microscopy, scanning transmission electron microscopy-energy dispersive X-ray spectrometry, and energy-filtered transmission electron microscopy to the characterization of nanoparticles in the environment. Environ. Sci. Technol. 37, (2003), 786-791

T. F. Kelly, M. K. Miller. Atom probe tomography. Rev Sci Instrum 78, (2007), 031101

T. H. Yoon. Applications of Soft X-ray Spectromicroscopy in Material and Environmental Sciences. Appl. Spectrosc. Rev. 44, (2009), 91-122

V. Protasenko, K. L. Hull, and M. Kuno. Demonstration of a Low-Cost, Single-Molecule Capable, Multimode Optical Microscope. The chemical educator 10, (2005), 269-282

V. V. Lider. X-ray microsocopy. Physics-Uspekhi 60, (2017), 187-203

V. Westphal, L. Kastrup and S. Hell. Lateral resolution of 28 nm (λ/25) in far-field fluorescence microscopy. Appl. Phys. B 77 (2003), 377-80

W. Baumeister, R. Grimm, and J. Walz. Electron tomography of molecules and cells. Trends in Cell Biology 9, (1999), 81-85

W. Denk, H. Horstmann. Serial Block-Face Scanning Electron Microscopy to Reconstruct Three-Dimensional Tissue Nanostructure. PLoS Biol 2, (2004), e329

W. Denk, J. H. Strickler, W. W. Webb. Two-photon laser scanning fluorescence microscopy. Science 248, (1990), 73-76

X. Chen, K. W. Noh, J. G. Wen & S. J. Dillon. In situ electrochemical wet cell transmission electron microscopy characterization of solid-liquid interactions between Ni and aqueous NiCl2. Acta Mater. 60, (2012), 192-198

Y. Yamamoto and K. Shinohara. Application of X-ray Microscopy in Analysis of Living Hydrated Cells. The Anatomical Record (New Anat.) 269, (2002), 217-223

Chapter 2: Experimental materials and technologies

2.1 Experimental materials

2.1.1 SBA Latex

Latexes are colloidal suspension of polymer particles, stabilized by the surfactant molecules localized on the surface of the particles *[J. Faucheu et al. (2009)]*. The surfactant molecules are either ionic or steric, and depending on the polymers involved, the particles are micrometric or submicronic. Styrene Butyl Acrylate SBA (BASF R&D lab) is a copolymer derived from styrene and metacrylic acid esters in aqueous solution, and already include a charged stabilizer (3%wt PMMA (polymethyl methacrylate)), playing the role of steric surfactant. The low glass transition temperature of SBA (soft phase, of chemical structure displayed in Figure 1a) is responsible for a good film elasticity, and high-film gloss. The high glass transition temperature of PMMA (hard phase, of chemical structure displayed in Figure 1b) provides a good blocking resistance and surface hardness to the films. The hard phase acts as transparent fillers providing block resistance, and should not be separated from the surface of the soft polymer surface *[A. K. Khan et al. (2009)]*. The hard phase has been grafted onto the soft phase during polymerization *[Y. Chevalier et al. (1997)]* and such systems are called core-shell latex. The SBA particle diameter is monodisperse and centered on 200 nm. The density of the SBA suspension is 1, the density of the film formed from SBA latex is 0.8. The dilution of the suspension is adjusted prior to each experiment, so that individual SBA-PMMA particles can be observed.

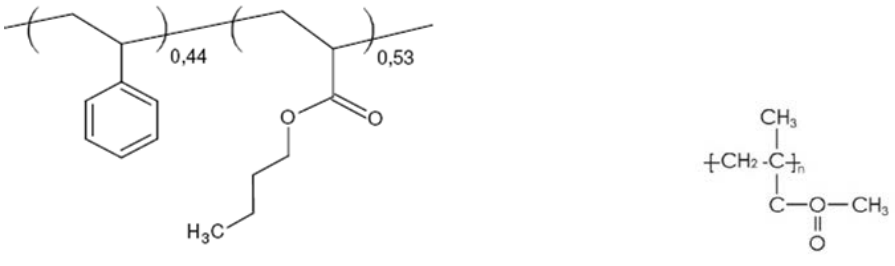

a) *b)*

Figure 1: Chemical structure of a) SBA; b) PMMA

2.1.2 Latex with surfactant

Some other surfactants can be introduced to further stabilize the latex for some specific applications *[J. Faucheu et al. (2009)]*. For the surfactants of amphiphilic composites, the nature of functional groups, molecular size, etc ... are key parameters in achieving the desired properties and keeping the robustness of its own properties during industrial production: (i) homogenous liquid suspension before use (ii) neat dense suspension while processing (iii) homogenous solid composites after drying. Two main strategies are used to achieve this purpose: either choosing the smallest available surfactant size to get a nano-structure; or designing a branch polymer with dedicated multifunctional heads so as to combine ionic and steric effects.

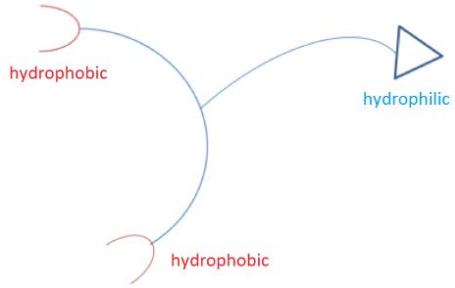

Figure 2: Chemical structure of surfactant XPCAS 803

The surfactant used in the study, in addition to PMMA, is XPCAS 803 (PCAS), which has a high molecular weight and combines three steric and ionic functional groups (two hydrophobic groups and one hydrophilic group, shown in Figure 2). XPCAS 803 is used in paints to disperse loads of latex. The morphology of the molecule leads to a considerable stiffness, which may enable to control phenomena such as cracking and shrinkage.

Table 1: Preparation of SBA with surfactant XPCAS 803

SBA (BASF)	8.393	g
H_2O	57.790	g
XPCAS 803	3.991	g
Total	70.174	g

The sample SBA with surfactant XPCAS 803 was prepared according to the proportion in Table 1, the mixture was then diluted in deionized water so as to perform ESEM experiment.

2.1.3 Gold nanoparticles

Gold has been widely used as model materials due to its superior stability. For a high quality tomographic reconstruction, the alignment of the projection series plays a very important role. Fiducial markers such as gold nanoparticles are often used as they exhibit a high contrast over the full range of tilt angles. For our research, gold nanoparticles are synthesized at Institut Lumière Matière according to a procedure described elsewhere *[C. Ziegler & A. Eychmüller, (2011)]*. Briefly, ascorbic acid is used as a reductant and sodium citrate as stabilizer, with a seeded growth approach to get gold nanoparticles with uniform spherical shape and narrow size distributions. The diameter of the gold nanoparticles is around 40 nm, and their morphology is spherical. Thus, those are suitable markers for easy and fast alignment of complex samples such as SBA described above. Moreover, the native suspension of gold is a material on its own, that can be analyzed as well as a model material.

2.1.4 Polyurethanes (PU)

Polyurethane (PU) is one of attractive electroactive polymers (EAP) with significant electrical-field strains *[B. Guiffard et al. (2006)]*, flexibility, high mechanical strength and biocompatibility with blood and tissues *[C. Putson et al. (2011)]*. The incorporation of nano-fillers, such as carbon nanotubes (CNTs), into a polyurethane (PU) matrix can greatly enhance their electromechanical properties *[D. Guyomar et al. (2009)]*. Functionalizing CNTs by grafting polymer chains onto their surfaces *[J. Zhu et al. (2003)], [H. Xia & M. Song (2006)]* can solve their poor dispersion and adhesion *[Z. M. Dang et al. (2007)]*.

The matrix is polyether-based thermoplastic polyurethane (Estane 58888 NAT021 – Lubrizol). Multi-walled Carbon Nanotubes (Cheap Tubes) exhibit a specific surface area of 60 m^2/g, with mean outer diameter 30 nm and length ranges between 10 and 20 μm. A "grafting onto technique'' was performed by Dr. Marie-Claire Dib-Jawar and Dr. Emmanuel Beyou in the lab "Ingénierie des Matériaux Polymères". It was used to ensure a good compatibility between

the grafted chains and the PU matrix. The polymer films were prepared by Mohamed Hedi Jomaa with a solution casting method (see Figure 3). After drying, the thickness of the films was about 100μm. For the tomography experiments, the films were embedded into an Epofix resin. Then, thin sections of about 600 nm were cut by Mohamed Hedi Jomaa at low temperature by cryo-ultramicrotomy.

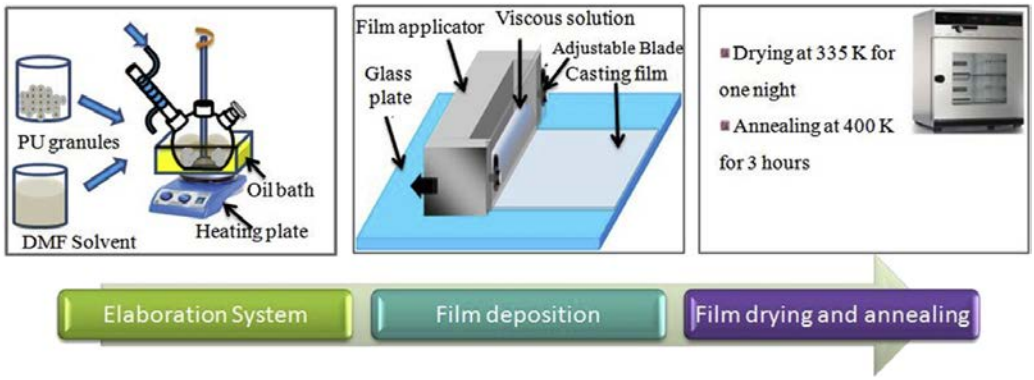

Figure 3. Elaboration protocol of polyurethane polymers [M. H. Jomaa et al. (2015)]

2.2 Experimental and simulation techniques

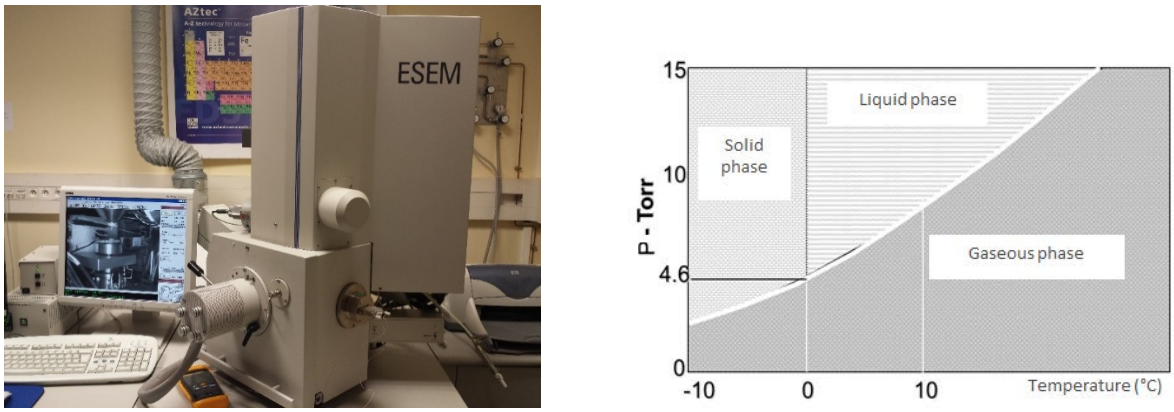

a) *b)*

Figure 4. a) XL 30 FEG ESEM from FEI; b) the (P, T) equilibrium phase diagram of water

In our research, two devices, described below, are used in a FEI XL 30 FEG ESEM (Figure 4a) from the Consortium Lyon-Saint Etienne de Microscopie (CLYM). The XL 30 ESEM is equipped with field emission gun (FEG) source. Unlike conventional SEMs which require

high vacuum in the specimen chamber, the pressure in this ESEM specimen chamber may be set equal to a wide range of values from conventional high vacuum to 10 Torr, which allows the examination of hydrated or insulating samples. Indeed in this range, the dew point (liquid-vapor equilibrium) can only be reached for samples cooled down to a few degrees, see Figure 4b.

2.2.1 2D analysis

2.2.1.1 2D device

As shown in Figure 5, a round cylindrical SEM mount with a fixed TEM sample holder is used to support the sample on a TEM grid. For liquid samples, like aqueous suspension of gold/polysiloxane nanoparticles *[M. Martini et al. (2010)]*, an eppendorf micropipette is used to put a droplet containing particles or floating objects (organic, inorganic) onto the TEM grid.

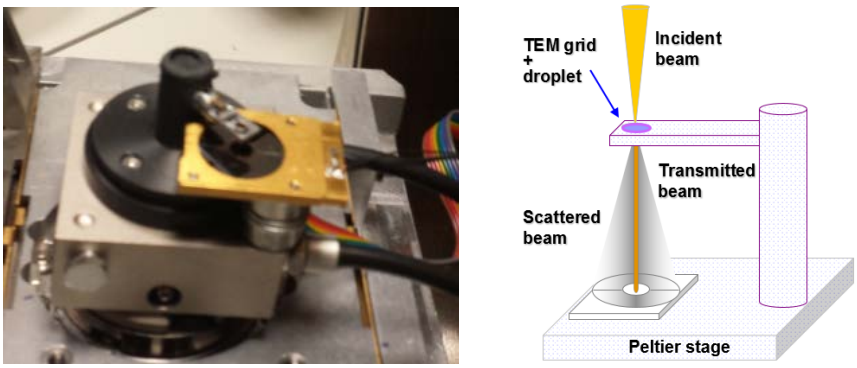

Figure 5. Schematic of the wet STEM device for annular dark-field imaging

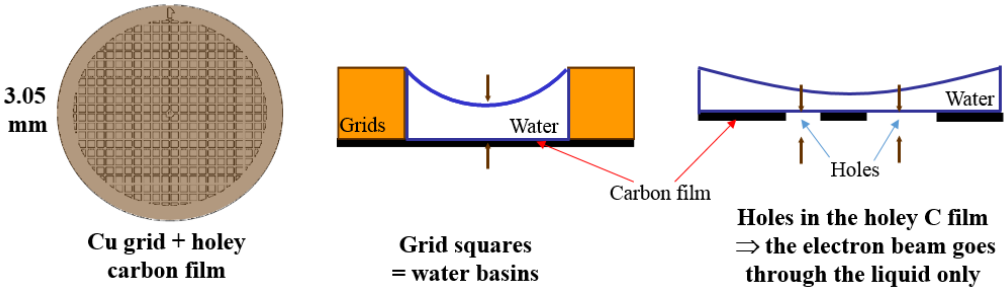

Figure 6. The copper TEM grids coated with holey carbon on one side

In this research, the 300-mesh copper TEM grids (diameter of 3.05 mm) with one side coated with holey carbon were chosen, as shown in Figure 6. The carbon layer is put underneath, so that the copper squares, with the length around 92 µm, behaves as retention basins for water *[A. Bogner et al. (2005)]*. The holes in the holey carbon film, with diameter from 1 to 20 µm, allow maintaining overhanging liquid films on some very small areas. All grids are pretreated by a "glow discharge" process before sample deposition to increase the carbon film wettability.

In this set-up, the convergent incident electron beam passes through the sample, a liquid suspension droplet or a thin solid slice. Then a solid-state backscattered electron (BSE) detector, located below the sample, is used to collect the scattered electron signal, the direct transmitted beam was not collected at all. In general, for the STEM mode in SEM, the BSE detector is a solid-state detector with two semi-annular parts A and B. With this detector, an important part of the scattered electrons available is used to form a highly contrasted image. This is of great interest for polymer and biological samples, known to give low contrasts because of their low atomic numbers. Besides, by using the sum signal, the imaging conditions are not linked to the area of the sample imaged *[A. Bogner et al. (2005)]*. The distance of sample-to-detector is set to 10 mm, which corresponds to collection angles between 250 to 700 mrad.

Regular ESEM detectors are also available to observe the sample surface in SE mode and in BSE mode with the gaseous SE detector GSED, and the gaseous backscattered electron detector GAD, respectively. These results can offer very useful information about the droplet thickness, for example to determine if the liquid layer is thin enough to allow a transmission observation.

A Peltier stage, located below the cylindrical SEM mount, is used to control the temperature of sample on the grid. The sample temperature is set by a thermoelectric stage controller (Figure 7), and the real-time temperature from the Peltier stage may be read at once on the screen of the controller.

Figure 7. Thermoelectric stage controller from FEI

Thanks to the ability of pressure variations in the ESEM chamber, evaporating a small amount of water from the initial droplet may be performed in situ. As water is withdrawn from the sample, the thickness of the suspension crossed by the electrons decreases. Below a specific threshold, electrons can pass through and thus be collected by the STEM detector to form the STEM images. Besides, in situ observations may be performed by controlling the evaporation of water for the suspension-type samples.

In the ESEM chamber, the gas introduced will however cause a broadening of the incident electron beam, which is called the “skirt effect”. In order to decrease the loss of resolution caused by this skirt effect, a gaseous annular detector equipped with a 9 mm long cone is placed below the objective lens. This, combine with a working distance between 10 and 11 mm, shortens the travelling distance of the incident electrons in the gaseous environment *[G. D. Danilatos, (1993)]*.

In order to avoid the suspension dehydration, the temperature of the Peltier stage is usually set to 2°C and the parameters of the purge sequences are carefully chosen too: 8 immediate consecutive purge cycles are performed between 6.5 and 9 Torr. Moreover, a few droplets of water are at first deposited on the stage outside the Peltier stage, to saturate the sample’ surrounding environment with water vapor, during the purge sequence. The water vapor pressure is then adjusted to evaporate water slowly from the sample, until it becomes electron transparent so as to enable observation.

2.2.1.2 Complementary analyses

Figure 8. SEM-Quanta FEG-250 of Centre Technologique des Microstructures (CTμ)

In order to gain further structural information about our samples, and compare the results from our home-made tomography device, several complementary analyses are performed using conventional ESEM and cryo-SEM.

Both experiments are conducted in a SEM-Quanta FEG-250 from FEI (Figure 8) from the Centre Technologique des Microstructures (CTμ). The microscope is equipped with a cryotransfert system Alto 2500 from GATAN. The experiments have been performed by Sylvie Descartes (LaMCoS) and Xavier Jaurand (CTμ).

- Cryo-ESEM

The cryo transfer system comprises a cryo chamber for sample preparation such as fracture or coating, and a cold stage. The temperature is controlled via the circulation of liquid nitrogen.

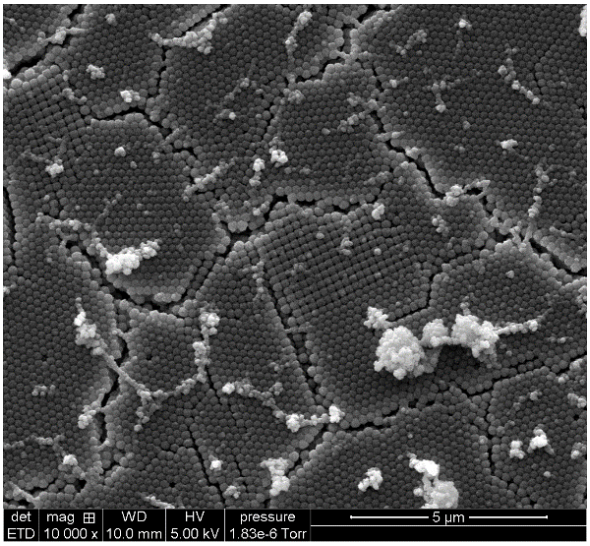

Figure 9. Image of latex SBA from cryo-experiments in SEM

The sample (undiluted SBA latex) is first mounted on a stub and then frozen by plunging into slush nitrogen. To prevent ice formation and contamination, the frozen sample is isolated and immediately transferred into the cryo-stage of a high vacuum cryogenic preparation chamber (-150°C). After gold coating, the sample is transferred onto the cold stage placed into the SEM chamber (-150°C). Even though the microscope can work in the environmental mode, all the following operations are performed under high vacuum. First, frost is sublimed off the surface by increasing the sample temperature up to -90°C during about 5 minutes. The sample was then cooled to -150°C and observed using the secondary electron detector, with the cold stage temperature, acceleration voltage and working distance set to -150°C, 10 kV and around 10 mm, respectively. Figure 9 shows a typical image of the latex suspension. Frost or impurities are still visible on the sample surface but the latex particle arrangement is clearly visible.

- ESEM with GSED detector

This mode is the most conventionally used in environmental SEM, as it is very similar to secondary electron imaging in conventional SEM. The conventional Everhart-Thornely scintillation-photomultiplier secondary electron detector cannot work at elevated pressures due to the high voltage (~ +12kV) involved in its operation *[M. R. Phillips & S.W. Morgan, (2005)]*. As a result, a special detector dedicated to secondary electrons was developed, which

performs under low vacuum conditions with the presence of gas in the specimen chamber *[G. D. Danilatos, (1983)]*. On FEI ESEM instruments, the Gaseous Secondary Electron Detector (GSED) works by measuring the current induced in the positive electrode. With the impact of the primary beam, both positive ions and additional electrons are formed from gas molecules. The positive ions can usefully suppress the sample charging, which allows direct observation without coating. The additional electrons can amplify the electron signal.

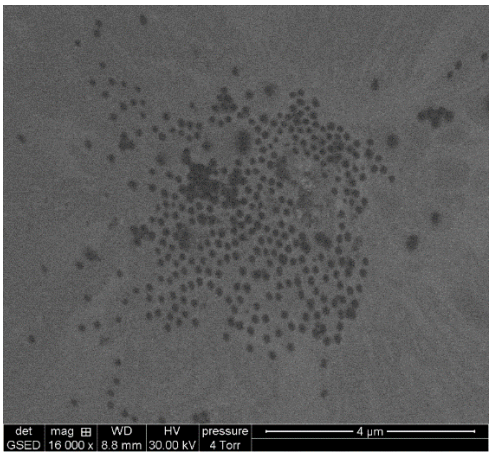

Figure 10. Image of undiluted latex SBA observed by GSED in ESEM, obtained with the chamber pressure 4 Torr, accelerating voltage 30kV and working distance 8.8 mm

A droplet of suspension (undiluted SBA latex) is deposited into the Peltier stage cooled down to 2°C. Then, the purge conditions are chosen so as to maintain the liquid stage (conditions similar to those used for STEM-in-SEM experiments). Figure 10 shows an image of SBA latex obtained using the GSED with an accelerating voltage of 30 kV and a working distance of 8.8 mm. Owing to the detection used, the grey level variations in the images can be related to topography changes.

2.2.1.3 Monte Carlo simulation

In electron microscopy, the incident beam penetrates into the microstructure of sample and interacts with both the positive atomic nuclei and the negative electrons. Elastic scattering occurs when some collisions with the atomic nuclei do not significantly change the energy of the incident electron. Elastic scattering corresponds to the interaction of the incident electron

with the atomic nucleus (Rutherford scattering), and results in a large deviation angle of the electron compared to the incident direction. Backscattered electrons are elastically scattered electrons with large deviation angles. Secondary processes due to inelastic scattering (such as emission of secondary electrons, x-rays and Auger electrons; generation of electron-hole pairs) also take place due to the energy transfer from the incident electrons to the sample. The elastic scattering and inelastic scattering happen both simultaneously and side by side in this process. Consequently, the original sharply focused electron beam spreads over a large volume. The shape and size of this interaction volume depend upon coupled parameters such as the sample composition and density, the angle of incidence and the energy of the electron beam *[R. Abargues (2006)]*. There is a common agreement in the scientific literature available, Monte Carlo calculations offer the most accurate theoretical results of the extension and shape of the scattering volume.

In this work, Monte Carlo simulations are performed with the software Hurricane® from SAMx, an off-line computation program dealing with electron-matter interaction. Hurricane has some specificities comparing the existing Monte Carlo programs: individual interactions (scattering, lost energy, production of photons and electrons) are fully computed; secondary electrons and phenomena induced by fast electrons are taken under consideration; computation are done from theoretical laws, with no averaging formula and no adjustment.

Hurricane is based on a networking of the space, and it can be divided into very small cells where events are studied. Hurricane is helpful especially when regular analytical quantitative methods are not valid, such as heterogeneous chemical samples, rough samples, particles in a different matrix, or specific geometries. Furthermore, complex geometries can be defined by combining primitives (spheres, cylinders, rhombohedra). As a result, any sample (precipitates of any form and any chemistry defined within a matrix) can be simulated.

All required parameters should be defined within the user interface. The first step is to define the chemical components and the densities of both the matrix and the precipitates. These components can be either pure or compound. In the example in Figure 11, a compound (water H_2O) and a pure material (Au) are defined, the compound being defined by the weight fraction

or the atom fraction of each element. The name of the compound (generated automatically as "compound X" by default) can also be changed according to the user.

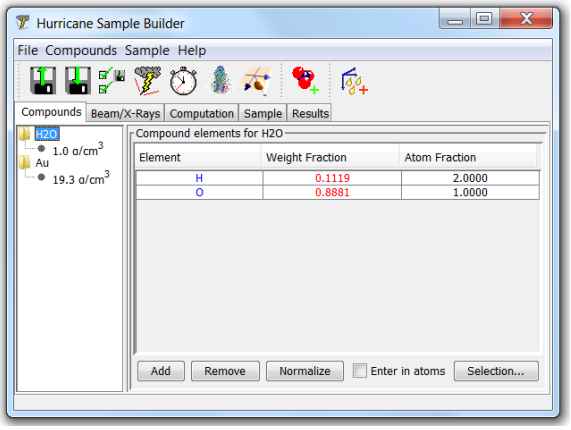

Figure 11. Definition of the chemical components of the sample (gold and water as an example) in Hurricane

The second step is to choose the experimental conditions in the section of working window 'Beam/X-ray', as shown in Figure 12: accelerating voltage, beam mode, center position and density. The default values of the origin for the beam are (0, 0) which correspond to the center of the sample.

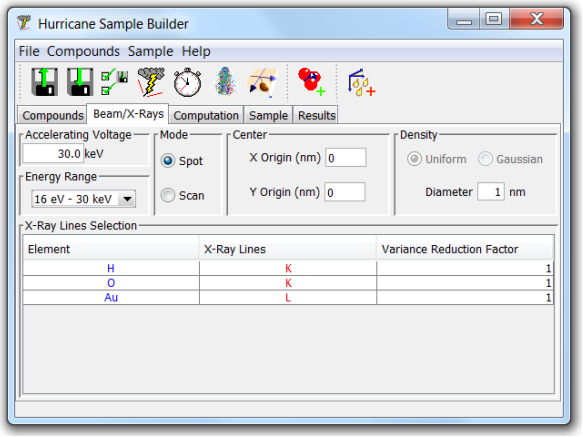

Figure 12. Definition of the beam conditions in Hurricane

The number of electron trajectories (Figure 13) used to run the simulation is the key-vault parameter, which mainly depends on the excitation conditions: a higher beam intensity indicating a greater number of trajectories. From the point of view of statistics, it should be

kept high enough to obtain a reliable result, but this also means to spend much more time to finish the simulation. This number can be reduced if scattered electrons are the only interesting feature. However if considering the emerging X-ray intensity (a less probable event), or in a situation with high absorption, more trajectories are required to obtain a good statistic. In our simulations, the trajectories of 1,000,000 electrons are calculated.

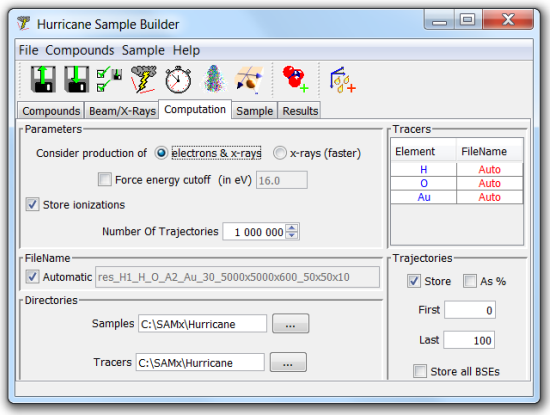

Figure 13. Definition of the computation conditions in Hurricane

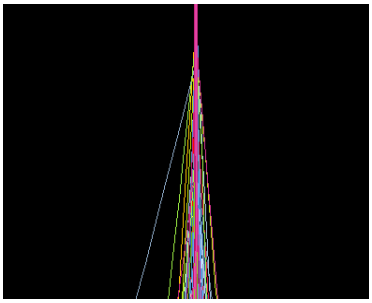

Figure 14. The simulation result of electrons trajectories for Au particle in the matrix H_2O (computation box: x = 5000 nm, y = 5000 nm)

For this simulation algorithm, all the interactions between the incident beam and the sample are contained in a three dimensional grid of cubes: the computation box (XYZ). All the interesting events are detected and stored in a unit box. In order to avoid any artefact with the borders, the computation box should be large enough comparing to the unit cell, otherwise a miss-estimation of the scattered electrons and other electron production processes will influence the results. In order to avoid electrons escaping from the x and y sides of the computation box, the values x = 5000 nm, y = 5000 nm, as shown in Figure 14, are usually chosen.

Besides, a high accelerating voltage means a high scattering volume, so a large computation box is needed for this case. Generally speaking, a small size of unit cell is required to get fine profiles of results, but this needs large amounts of memory and long calculation times. These conditions also can be adjusted according to the simulation results.

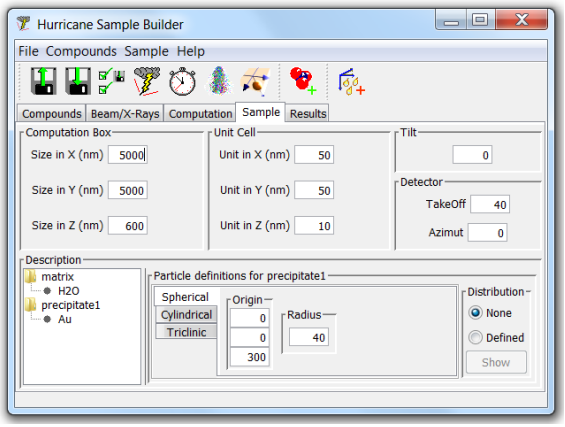

Figure 15. Definition of the sample in Hurricane, example of 40nm radius gold particle with model morphology sphere, simulated in water suspension

Once the computation box is defined, the matrix and precipitates can be determined from the compounds, which were defined in the first step. In our version of Hurricane, three model morphologies are available (sphere, cylinder and rhombohedron). An example is shown in Figure 15: taking sphere as model morphology, a gold particle (the coordinates of its center are: 0, 0, 300) with a radius of 40 nm is simulated in a H_2O matrix.

In the software Hurricane, the electrons going outside of one computation box side are automatically classified according to their direction inside six text files (positive and negative directions of x, y and z with default names as: xN, xP, yN, yP, zN and zP, respectively) . In our experiment, the STEM detector is placed below the sample and collects the scattered electrons with angles between 250 and 700 mrad. So for the simulation results, we are only interested in the number of electrons escaping with angles ranging between 250 and 700 mrad in the direction of positive Z (under the sample).

2.2.2 3D analyses

2.2.2.1 3D Device

Combining wet-STEM and ESEM, a home-made wet-STEM tomography device was designed prior to this PhD work *[C. Gauthier et al. (2006); P. Jornsanoh et al. (2011)]*, as shown in Figure 16. The device consists of five main parts:

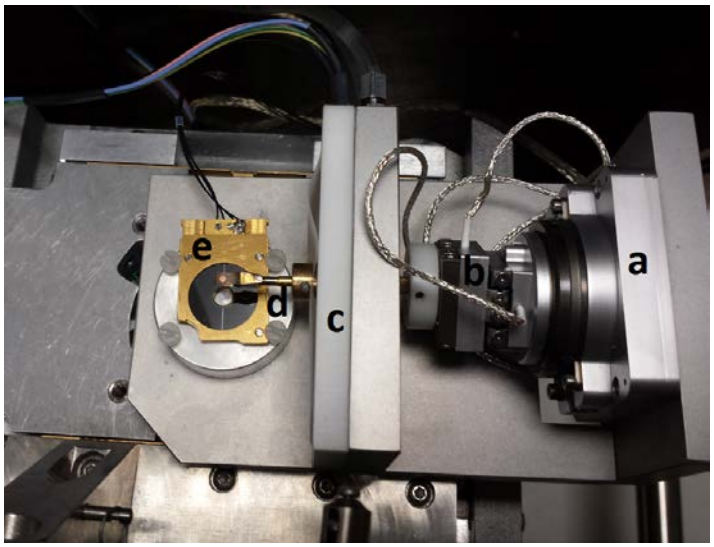

Figure 16. Schematic of the home-made wet STEM tomography device

(a) A tilting system: thanks to the large chamber in ESEM, a rotating piezoelectric system for rotation of 360° around the horizontal axis is introduced, and the accuracy of rotation reaches 0.001°.

(b) A two-translation piezoelectric system: it is used to adjust the area of interest to the eucentric position (at the intersection of the optical and the rotation axes) and/or to keep it in the field of view while tilting.

(c) A Peltier stage: as for the 2D device, a Peltier stage is used to control the sample temperature, which is compulsory to study liquid samples. In this case, the Peltier stage is placed vertically between the piezoelectric systems and the sample holder. By slight friction,

the cold is transferred from the Peltier stage to the sample holder. A thermocouple inserted inside the Peltier stage helps to control the sample temperature through the FEI thermoelectric stage controller.

(d) A sample holder: there are several kinds of sample holders for different kinds of materials. For the TEM grids, a kind of "tweezer" is available, as shown in Figure 16.

(e) A detection system: an annular dark-field detector placed under the sample is used to collect the scattered electrons, as in the case of the 2D device. The sample-to-detector distance equals 10 mm for any experiment. For such a configuration, the collection angles range between 250 and 700 mrad.

2.2.2.2 Data processing for tomography

After acquiring series of STEM images at different tilts, the image data will be processed for 3D visualization, quantification or some other exploitation. Generally speaking, the data processing for tomography incorporates re-alignment for obtained original image series and volume reconstruction. In most cases, the reconstructed volume will be further segmented for quantitative analysis *[Frangakis, (2006)]*. In our 3D characterization, resolution is also analyzed for evaluating the performance of our device. Several software and programs are combined to perform these data processing.

-Image Alignment

During the series acquisition, some drifts may happen caused by the deviations of tilt axis away from object mean plane, not perfect adjustment for eucentricity, or limited mechanical accuracy of the sample holder. Therefore, an accurate alignment of the images acquired at different tilts is mandatory. Any mismatch in image alignment will cause blurring or smearing in the volume reconstruction *[D. N.* Mastronarde, *(2006)]*. Tracking the movement of specific markers is the most useful method for alignment. The markers chosen usually are spherical particles with high contrast so as to be identified easily. Gold nanoparticle is a good choice as fiducial marker for the measurement of the positions over the full range of projection images.

A free software tool Etomo (*http://bio3d.colorado.edu/imod/doc/etomoTutorial.html*) is used to perform image alignment.

-Volume Reconstruction

TomoJ (*http://u759.curie.fr/en/download/softwares/TomoJ*) is an isotropic-diffusion plugin developed by Cedric Messaoudi et al. in ImageJ (*http://rsbweb.nih.gov/ij/*) and Fiji (*http://fiji.sc/Fiji*), specifically designed for electron tomography. It's an open source program based on the Java language. TomoJ provides various algorithms for volume reconstructions used in tilting tomography, including iterative reconstructions: ART (Algebraic Reconstruction Technique), SIRT (Simultaneous Iterative Reconstruction Technique) and SART (Simultaneous Algebraic Reconstruction Technique), as well as the commonly used approach of WBP (Weighted Back-Projection). In consideration of the properties of our samples and calculating time, volume reconstruction is performed with a 15 iteration steps implementing ART algorithm. Appropriate 3d median filters *[M. Maiorca, (2012)]* of 3 pixels are then applied on the final volumes in ImageJ.

-Segmentation

Segmentation is a mandatory step, to get quantitative information from the volume reconstruction. Usually, Trainable Waka Segmentation, a plug-in in Fiji, is used for the initial segmentation. And then 3D Slicer *(http://www.slicer.org/)* could be further used for modeling the spatial structure.

- Resolution

Spatial resolution in tomogram is studied by Fourier Shell Correlation (FSC) *[G. Harauz & M. Van Heel (1986)]*. We used the free software which can be downloaded from the Image Science web site (www.ImageScience.de). Firstly, the aligned tilt series is divided into two different subseries ("odd" and "even"), according to the image number. Then, the volume is reconstructed from either the odd or the even tilted series. By measuring the normalized cross-correlation coefficient over corresponding shells of constant spatial frequencies, the odd and

even reconstructed volumes are compared by FSC algorithm. The spatial frequency corresponding to the intersection of the FSC curve and a previously defined criterion indicated the resolution on the volumes *[M. van Heel, M. Schatz, (2005)], [K. Masenelli-Varlot et al., (2014)]*. In our case, the resolution is defined by the distance for which the FSC curve crosses the half-bit curve or sigma curve, which is attributed to the distance above which signal can be distinguished from noise. Then, the resolution on the full tomogram is roughly estimated to be equal to half the resolution determined on the even/odd volumes.

References

A. Bogner, G. Thollet, D. Basset, P.-H. Jouneau, C. Gauthier. Wet STEM: A new development in environmental SEM for imaging nano-objects included in a liquid phase. Ultramicroscopy 104**,** (2005), 290–301

A. K. Khan, B. C. Ray, J. Maiti, and S. K. Dolui. Preparation of core-shell latex from co-polymer of styrene-butyl acrylate-methyl methacrylate and their paint properties. Pigment & Resin Technology 38, (2009), 159–164

A. M. Donald. The use of environmental scanning electron microscopy for imaging wet and insulating materials. Nat. Mater. 2, (2003), 511–516

B. G. Trewyn, I. Slowing, S. Giri, H.T. Chen, V.S. Lin. Synthesis and functionalization of a mesoporous silica nanoparticle based on the sol-gel process and applications in controlled release. Acc Chem Res 40, (2007), 846–853

B. Guiffard, L. S., G. Sebald and D. Guyomar. Enhanced electric field induced strain in non percolative carbon nanopower / polyurethane composites. J. of Phys. D: Appl. Phys. 39, (2006), 3053

C. Gauthier, P. Jornsanoh, K. Masenelli-Varlot, G. Thollet. Montage pour effectuer de la tomographie électronique dans un microscope électronique à balayage et à pression contrôlée. FR Patent 06, (2006), 09–708

C. Putson, L. Lebrun, D. Guyomar, N. Muensit, P.-J. Cottinet, L. Seveyart, and B. Guiffard. Effects of copper filler sizes on the dielectric properties and the energy harvesting capability of nonpercolated polyurethane composites. J. Appl. Phys. 109, (2011), 024104

C. Ziegler & A. Eychmüller. Seeded Growth Synthesis of Uniform Gold Nanoparticles with Diameters of 15-300 nm. J. Phys. Chem. C 115, (2011), 4502-4506

D. B. Williams, C.B. Carter. Transmission Electron Microscopy—III. Imaging, Plenum Press, NewYork

D. Guyomar, L. Lebrun, C. Putson, P-J. Cottinet, B. Guiffard, and S. Muensit. Electrostrictive energy conversion in polyurethane nanocomposites. J. Appl. Phys.106, (2009), 014910

D. N. Mastronarde. Fiducial Marker and Hybrid Alignment Methods for Single- and Double-Axis Tomography. Electron Tomography, (2006), 163–185

G. D. Danilatos. A gaseous detector device for an environmental SEM, Micron Microsc. Acta 14, (1983), 307–318

G. D. Danilatos. Introduction to the ESEM instrument. Microsc Res Tech 25, (1993), 354–361

G. Harauz & M. Van Heel. Exact filters for general geometry three dimensional reconstruction. Optik 73, (1986), 146–156

H. Xia, & M. Song. Preparation and characterisation of polyurethane grafted single-walled carbon nanotubes and derived polyurethane nanocomposites. J. Mater. Chem 16, (2006), 1843–1851

J. Faucheu, L. Chazeau, C. Gauthier, J.Y. Cavaillé, M. Goikoetxea, R. Minari and J. M. Asua. Latex Imaging by Environmental STEM: Application to the Study of the Surfactant Outcome in Hybrid Alkyd/Acrylate Systems. Langmuir 25, (2009), 10251-10258

J. Zhu, J. D. Kim, H. Peng, J. L. Margrave, V. N. Khabashesku & E. V. Barrera. Improving the dispersion and integration of single-walled carbon nanotubes in epoxy composites through functionalization. Nano Lett 3, (2003), 1107–1113

K. Masenelli-Varlot, A. Malchère, J. Ferreira, H. Heidari Mezerji, S. Bals, C. Messaoudi, S. Marco Garrido. Wet-STEM Tomography: Principles, Potentialities and Limitations. Microscopy and Microanalysis 00, (2014), 1-10

L. Reimer. Scanning Electron Microscopy: Physics of Image Formation and Microanalysis, second ed, Springer, Berlin, Heidelberg, New York, 1998

M. H. Jomaa, L. Seveyrat, L. Lebrun, K. Masenelli-Varlot, J.Y. Cavaille. Dielectric properties of segmented polyurethanes for electromechanical applications. Polymer 63, (2015), 214-221

M. Maiorca, E. Hannssen, E. Kazmierczak, B. Maco, M. Kudryashev, et al. Improving the Quality of Electron Tomography Image Volumes Using Pre-Reconstruction Filtering. Journal of Structural Biology 180, (2012), 132–142

M. Martini, S. Roux, M. Montagna, R. Pansu, C. Julien, O. Tillement, P. Perriat. How gold inclusions increase the rate of fluorescein energy homotransfer in silica beads. Chem Phy Lett 490, (2010). 72–75

M. R. Phillips & S.W. Morgan, Direct Comparison of Various Gaseous Secondary Electron Detectors in the Variable Pressure Scanning Electron Microscope, Microsc Microanal 11, (2005), 398-399

M. van Heel, M. Schatz. Fourier shell correlation threshold criteria. Journal of Structural Biology 151, (2005), 250–262

P. Jornsanoh, G. Thollet, J. Ferreira, K. Masenelli-Varlot, C. Gauthier, A. Bogner. Electron tomography combining ESEM and STEM: A new 3D imaging technique. Ultramicroscopy 111, (2011). 1247–1254

R. Abargues. Conducting polymers as charge dissipater layers for electron beam lithography. Ph.D. Thesis in Chemistry, University of Valencis, (2006)

Y. Chevalier, M. Hidalgo, J.-Y. Cavaille, B. Cabane. Small angle neutron scattering studies of composite latex film structure. Progress in Organic Coatings 32, (1997), 35-41

Z. M. Dang, L. Wang, Y. Yin, Q. Zhang & Q. Q. Lei. Giant Dielectric Permittivities in Functionalized Carbon-Nanotube/Electroactive-Polymer Nanocomposites. Adv. Mater. 19, (2007), 852–857

Chapter 3: Comprehension of the contrast in Wet-STEM

For liquid samples, contrast inversions may occur with changes of water film thickness, so one of the most important thing in STEM-in-ESEM is the estimation of the water film thickness. One method to estimate the thickness of water for liquid suspensions is to compare the contrasts measured in the experimental images with the calculations using Monte-Carlo simulations. In this chapter, two kinds of suspensions (gold nanoparticles or core-shell SBA latex particles in water) described in chapter 2 are studied with Monte Carlo simulations.

Observations were carried out in an ESEM XL-30 FEG using the 2D device described in chapter 2, with the acceleration voltage 30 kV. A 1 µl droplet of suspension was deposited with an Eppendorf micropipette onto a 300-mesh TEM copper grid. The temperature of the Peltier stage was set to 2°C so as to avoid any unwanted fast dehydration, and the water vapor pressure was decreased slowly from the initial value around 6.5 Torr until transparency of the water film. A backscattered electron detector is placed below the sample to collect the scattered signal. The distance of sample-to-detector is 10 mm, which allows the collection of the electrons scattered between 250 and 700 mrad.

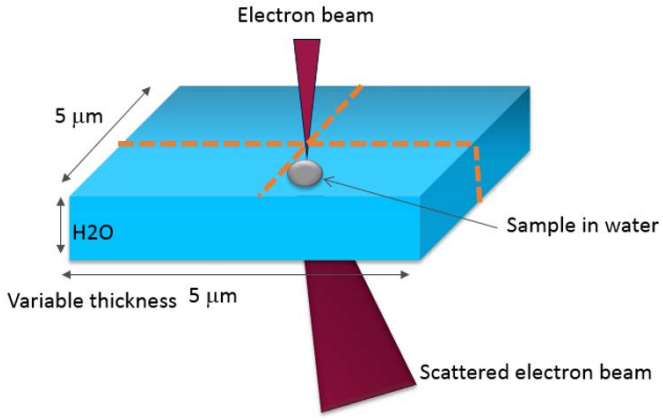

Figure 1. Sample geometry used for Monte Carlo simulations

Figure 1 displays the Monte Carlo Simulations geometry associated to this study. In this simulated model, a spherical particle was immersed into the matrix H_2O. Each spherical

particle of variable diameter represents an object in suspension. Except in several specific cases, the particle was placed at the center of the water film.

The water film of variable thickness was defined with its lateral dimensions equal to 5 µm, so that a negligible amount of electrons escape through the lateral edges (see Figure 2). Figure 2a shows the paths of the incident electrons within a water film of 500 nm thickness. Only around 0.01% electrons escape through both the x and y sides of the water film. In the ESEM experiment, the water layer becomes thinner and thinner with the water evaporation, and disappears in the end, arriving to the dry state. So the simulated thicknesses of water used were chosen to range from thousands of nanometers down to zero value. Figure 2b shows the scattered electrons paths in a large water film thickness of 5000 nm, focusing on the early life of a dilute liquid suspension. Compared to Figure 2a, more electrons are absorbed and escape from the top or the sides of the water film. But even in this case (maximum thickness value for our study), the electrons escaping by any lateral directions is still quite low and only equal 3.5%.

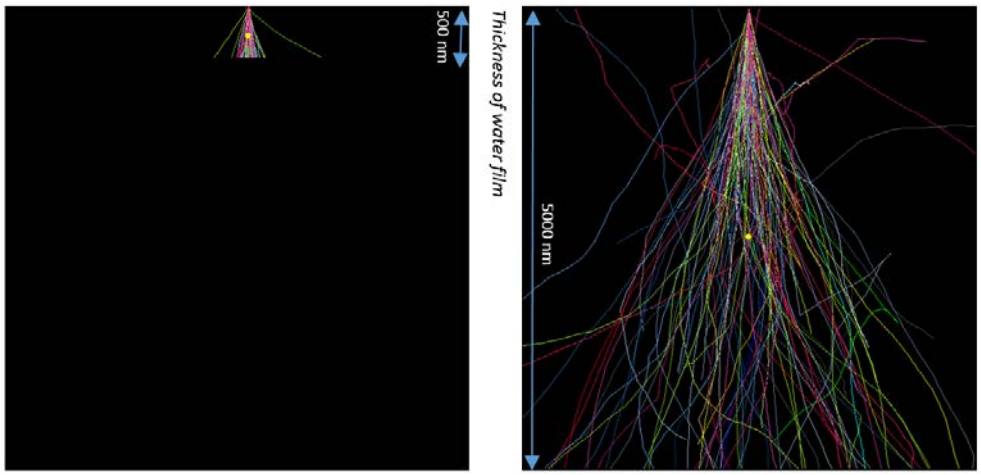

a) *b)*

Figure 2. Paths of the incident electrons within a pure water film. a) water thickness 500 nm; b) water thickness 5000 nm

Furthermore, the incident electron energy was always set to 30 keV. In the following discussion, a Weber contrast with the formula $C = \frac{n-n_b}{n_b}$ (where n and n_b correspond to the

number of collected electrons on the region of interest and on the surrounding background, respectively) was used. This contrast value was computed from the Monte Carlo simulation data in order to describe how a region of interest can be distinguished from the surrounding water film.

3.1 Gold nanoparticles in water

3.1.1 Simulations results

Figure 3 shows the number of electrons collected by the STEM detector in the case of aqueous suspensions of gold nanoparticles, as calculated with Monte Carlo simulations. The radius of the gold nanoparticles ranges between 0 (pure water) and 80 nm, while the thickness of water lies between 50 nm and 5 µm. Twelve water thickness values are simulated for nine gold nanoparticle sizes. The simulated value of collected electron number mainly ranges in the domain [100 000, 500 000].

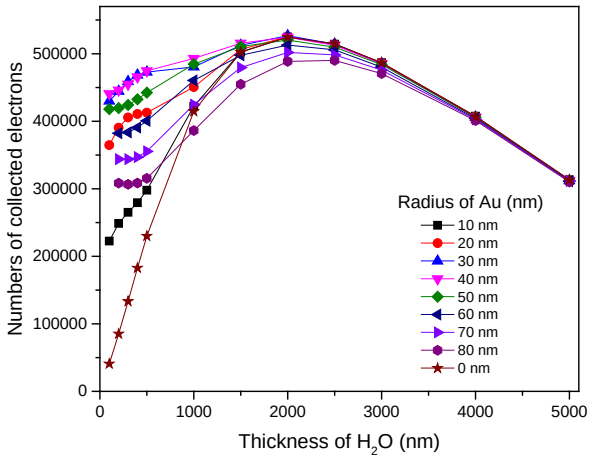

Figure 3. Number of electrons calculated from Monte Carlo simulations, as a function of the thickness of the water film for different radius values of the gold nanoparticle

For each suspension, the overall shape of the curve is similar to the one presented by A. Bogner *et al. [A. Bogner et al. (2007)]*, with a maximum occurring at around 2 µm (water film thickness). Below this value, an increase of the water thickness leads to an increase of the

number of electron-water interactions and thus to an increase of the scattering angle. As a consequence, more electrons are collected by the STEM detector. Above 2 µm, as water film thickness increased, more and more electrons are scattered with angles above 700 mrad and are not collected anymore. At the same time, the number of electrons absorbed by the water increases with the increase of the water film thickness.

Let us pay attention to the object size, for a given thickness of water, that is to say considering a vertical line in Figure 3 or a curve in Figure 4. The number of collected electrons also exhibits a maximum value. The maximum occurs for radius in the range of 30 to 40 nm, and seems less pronounced for water film thicknesses above 1000 nm.

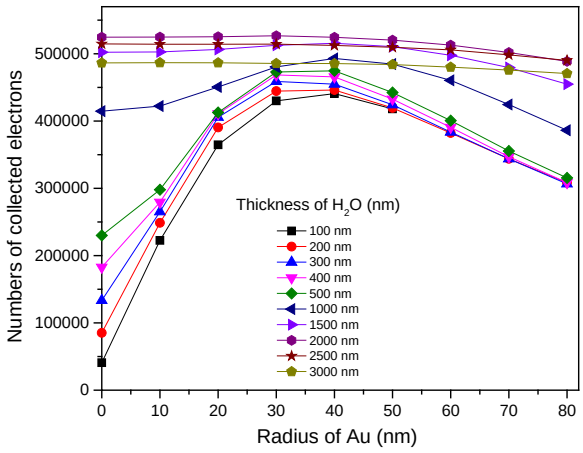

Figure 4. Number of electrons calculated from Monte Carlo simulations, as a function of the radius of the gold nanoparticle for varied thicknesses of the water film: the calculated values reach a maximum for Au radius in the range of 30 to 40 nm. The maximum is less pronounced for water film thicknesses above 1000 nm

Figure 5 represents the contrast between a gold nanoparticle and the water film for water film thinner or equal to 1 µm, calculated from the simulated electron numbers from Figure 3. Under these conditions, all the gold nanoparticles are bright, and show a very high contrast when water films are thinner than 500 nm. In addition, the contrast decreases obviously with the increase of the water film thickness from 100 nm to 1000 nm.

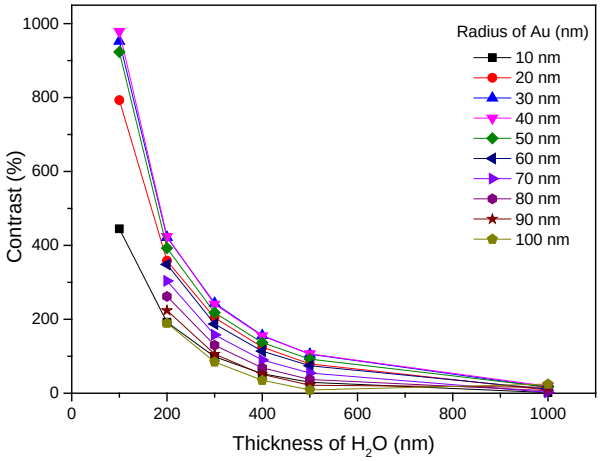

Figure 5. Weber Contrast of gold nanoparticles with varied sizes as a function of water film thickness (less than 1000 nm). In the simulations, the gold nanoparticles stand at the center of the water film

However, the results are quite different when considering a larger range of water film thicknesses between 1000 and 5000 nm, as demonstrated in Figure 6. The gold nanoparticles appear dark for water films thicker or equal to around 2000 nm, and the contrast tends to zero for very thick water films. This means that in the case of thick water films, the darkest particles are the biggest ones.

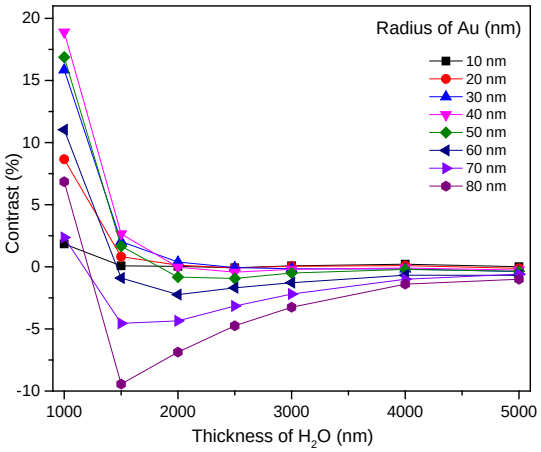

Figure 6. Weber contrast for the gold nanoparticles with respect to the thickness of water (more than 1000 nm). In the simulations, the gold nanoparticles were placed at the center of the water film

The result presented in Figure 6 actually illustrates the loss of resolution due to the top-bottom effect *[A. Bogner et al. (2007)], [U. Golla-Schindler (2004)]*. Evidence is given in Figure 7a, where the contrast of a gold nanoparticle with the radius of 20 nm, which was immersed in a water film of thickness 2000 nm, is plotted against the distance of the nanoparticle to the top surface. It can be clearly seen that gold appears very dark when placed very close to the top surface, whereas the contrast is very close to zero when the nanoparticle is placed deeper than 1000 nm. When considering the case of thin water film (less than 1000 nm), an example of water film thickness 100 nm as shown in Figure 7b, top-bottom effect is insignificant. Therefore, in the simulations of thin water film, the particles were placed in the center of the water, but results are relevant for any other position.

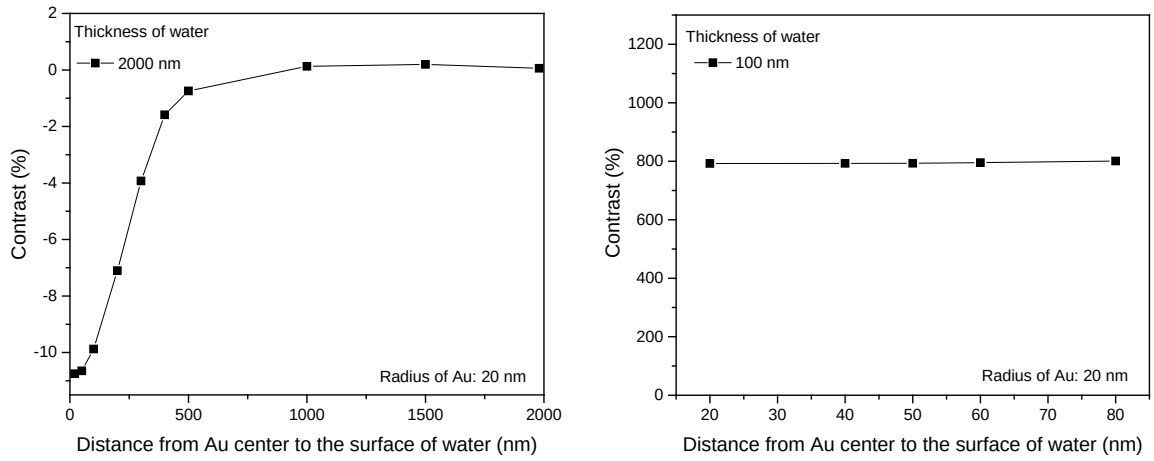

a) *b)*

Figure 7. Contrast between a 20 nm radius gold nanoparticle and the water film depending on the particle depth position. a) water film thickness of 2000 nm; b) water film thickness of 100 nm

Figure 8 displays the contrast variations of a gold nanoparticle (radius of 20 nm) with the thickness of the water film, when placed just below the top surface of the water film. As expected, the particle appears very dark in thick water films (thicker than 2000 nm). The contrast inversion, i.e. the transition between bright and dark features in the images, occurs for water films thickness about 1400 nm. The result is similar to what is shown in Figure 6 where the particles are placed in the middle of the suspension, but in the case of a gold particle with 20 nm radius, the contrast is almost zero when the water film is thicker than 1500 nm.

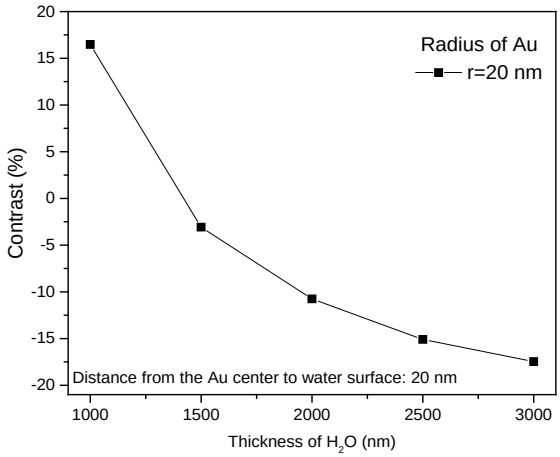

Figure 8. Contrast between a 20 nm radius gold nanoparticle and the water film, for film thicknesses ranging between 1000 nm and 3000 nm with a step of 500 nm

3.1.2 Experimental investigation and discussion

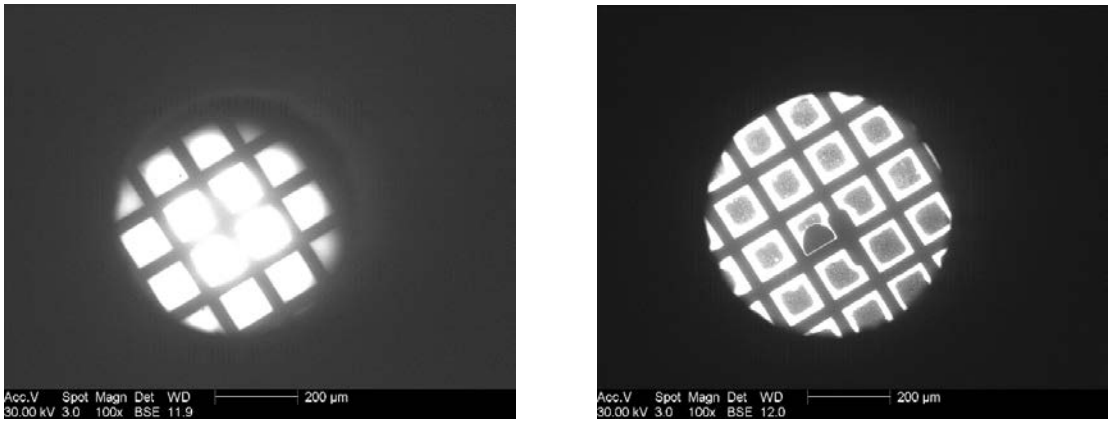

a) *b)*

Figure 9. Experimental image of a 20 nm radius gold nanoparticle with the water evaporation from image a) to image b)

During ESEM experiments on a suspension droplet deposited on a grid, all the grid squares are dark at the very beginning as they are all covered with a very thick water film. Then water begins to evaporate first slowly as pressure decreases in the chamber. The evaporation is faster within the scanned area due to the influence of the electron beam, a very bright area stands therefore in the image center (see Figure 9a). As shown in Figure 9b, dark areas appear firstly

in the center of each square as evaporation of water continues. This kind of brightness variations can be explained by the Monte Carlo simulation in Figure 3.

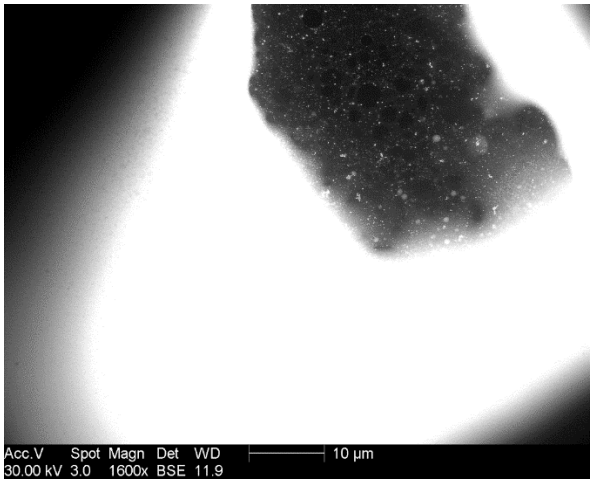

Figure 10. Experimental image of a gold nanoparticle with radius of 20 nm

A typical image acquired in one grid square is shown in Figure 10. The very bright area includes a high thickness water film, where the resolution of gold particles are lost totally. The dark area includes a low thickness water film, where bright gold particles can easily be observed.

Figure 11. Experimental image of an aqueous suspension of gold nanoparticles with radius of 20 nm (arrows show dark particles in the bottom left corner and bright ones in the top right corner of the image)

Figure 11 is an area between bright and dark zoomed in from Figure 10, which displays experimental proof of contrast inversion along the main diagonal of the image. The nanoparticles are dark in the bottom left corner and bright in the top right corner of the image, this means that the water film thickness increases from the top right corner down to the bottom left corner. Moreover, the absence of contrast between the gold nanoparticles and water, coupled with the knowledge gained from our Monte Carlo simulations, clearly suggests that the thickness of water film is here around 1400 nm.

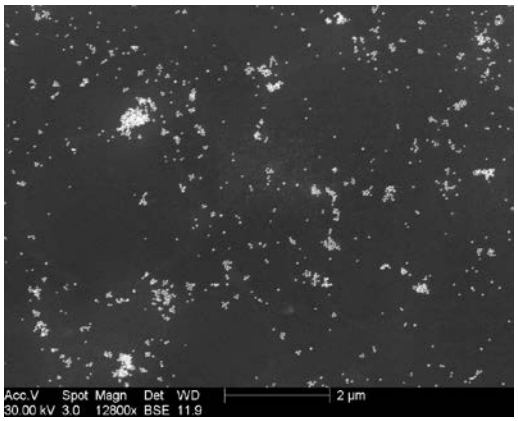

a)

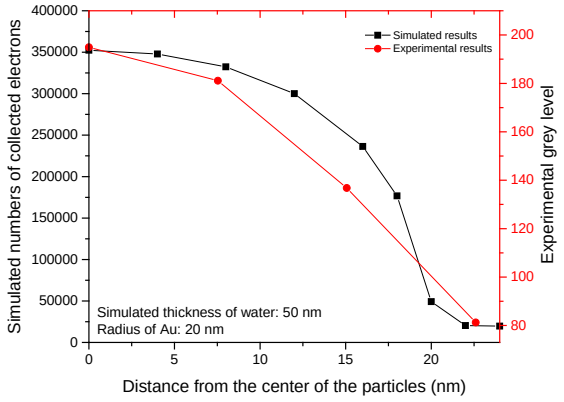

b)

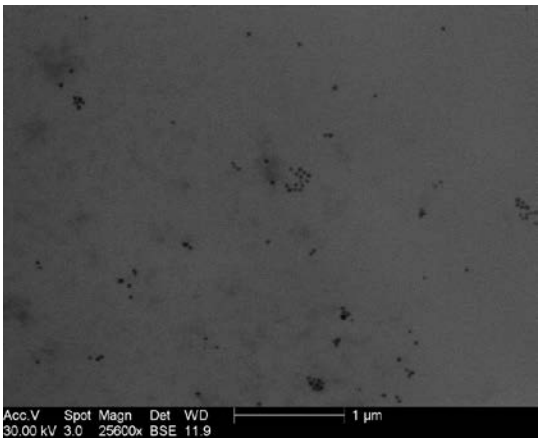

c)

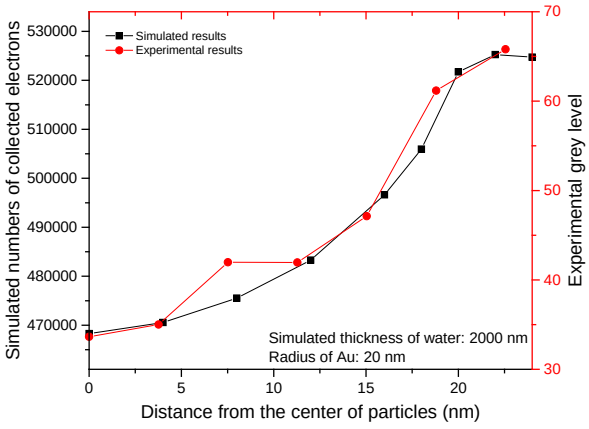

d)

Figure 12. Comparison between experimental images and Monte Carlo simulation results, on aqueous suspensions of gold nanoparticles. a) experimental image exhibiting bright nanoparticles; b) comparison of experimental and simulated profiles, indicating a thin water film (thickness ≤1000 nm); c) experimental image exhibiting dark nanoparticles; d) comparison of experimental and simulated profiles, indicating a thick water film (thickness ≥1500 nm)

Images obtained at higher magnification on aqueous suspensions containing bright and dark gold nanoparticles are given in Figure 12a and Figure 12c, respectively. According to the results of Monte Carlo simulations, the water film is thinner or equal to 1000 nm in the case of Figure 12a, whereas it is at least 1500 nm in the case of Figure 12c. A nice agreement can be found between the experimental (red curve) and simulated grey level profiles along the gold nanoparticles (see Figure 12b and Figure 12d). However, for instance in the case of Figure 12b, any simulated grey level profile with water film thickness ≤ 1000 nm could be used as long as the gold nanoparticles are brighter that water, which is represented in Figure 13. Similar grey level profiles along the gold nanoparticles can be obtained when considering the water film thinner or equal to 1000 nm.

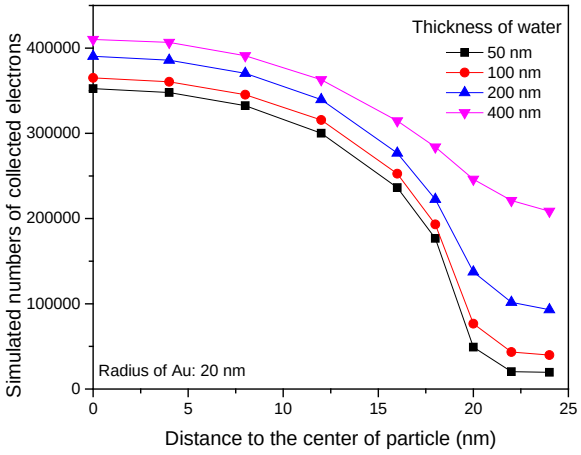

Figure 13. Simulated grey level profiles along the gold nanoparticles in thin water film (thickness ≤ 1000 nm)

Usually the particles in colloidal solutions exhibit a halo or greater contrast around the particle imaged in STEM mode. For the annular dark-field detectors, such contrast may be described as a mass-thickness inverse type *[C. J. G. Plummer]*. As a result, the thicker the particle or the higher its atomic number, the greater the contrast within the composition area, which also affects the contrasts of their surrounding and thus results in bigger sizes than the actual ones. Furthermore, particles in colloidal state are often stabilized by some ionic surfactants. These negative charges may interact with those diffused electrons and participate to create a halo around particles *[A. Bogner et al. (2005)]*. Therefore, the size of particles in suspension is

bigger according to the grey level profiles from the ESEM images compared with their own actual size and the simulated results.

This paragraph was dedicated to a simple model material, tiny spherical gold particles less than one hundred nanometers in radius. In conclusion, simulating such nanoparticles in dilute suspension within low and high thickness water film provides easy access to contrast analysis.

3.2 SBA/PMMA latex particles in water

SBA/PMMA latex is our second model material, larger than the gold one, not uniform as a surfactant partially cover its surface. It is simulated as a core-shell particle with a core and a shell of chemical compositions $C_{7.45}H_{10.2}O_{1.1}$ (density 1.07 $g.cm^{-3}$) and $C_5H_8O_2$ (density 1.18 $g.cm^{-3}$), respectively. The radius of the SBA core and the thickness of the PMMA shell were set to 85 nm and 15 nm, respectively. In the case of gold nanoparticles, the Monte Carlo simulations show a good agreement with the experimental images, even though it does not allow a better estimation of the water film thickness. It is possible to go further in the case of SBA-PMMA latex particles, partially because they have a core-shell structure. A lot of industrial processes use latex to provide functional properties for materials in the wet state, while dense suspension are formed with drying and then as solid, dry state materials. Wet-STEM in ESEM is therefore a great tool to check whether each step of the process fits the design target.

3.2.1 Simulation results

On the contrary to gold nanoparticles which exhibit a high contrast resulting from their high atomic number, the resolution for polymers, such as our sample SBA-PMMA latex particles, is lost in thick water films. Therefore, the analysis in thick water films are useless, and the simulations are only operated here with water film thicknesses between 0 (dry) and 400 nm. Besides, the latex particles are always placed at the center of the water film when the simulated water thickness is higher than the diameter of latex particles, as their position with respect to the top water surface does not have a significant influence in thin water films.

Figure 14 shows the simulated grey level profiles along SBA-PMMA (85-15 nm) particles immersed into water films up to 400 nm thickness, i.e. twice the diameter of latex particles. At a first glance, the simulated electrons number mainly ranges between 40 000 and 180 000, far less than that of gold model material. In thin films, for instance for water film thicknesses of 100 nm (red curve), the SBA core is brighter than water, whereas it is darker than water in thicker films (above 200 nm, the diameter of particles). Interestingly, for a dry particle (black curve), the grey level profile is very different compared to the wet state. Indeed in this case, the PMMA shell cannot be distinguished from the SBA core. On the contrary in the wet state, the PMMA shell seems to be always darker than the SBA core and water.

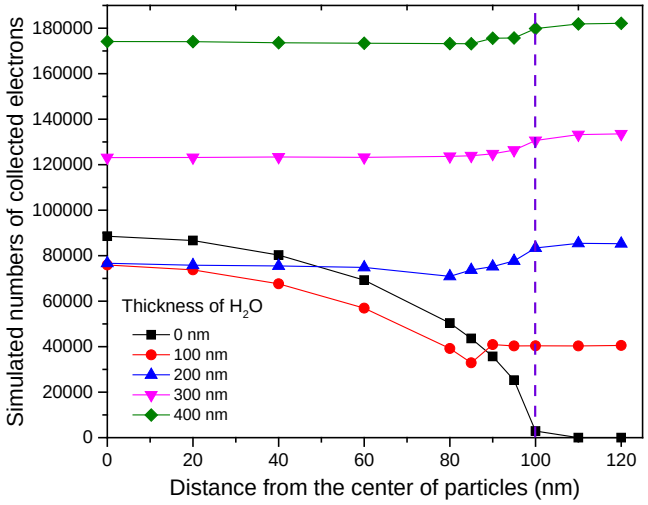

Figure 14. Simulated grey level profile along a SBA-PMMA particle in different thicknesses of water

3.2.2 Experimental investigation and discussion

At this stage, it is noteworthy to remind that polymer materials are quite sensitive to the electron beam. Irradiation may induce among other phenomena such as amorphization, crosslinking or degradation of the macromolecular chains *[L. Sawyer et al. (2008)]*. In the case of suspensions, radiolysis of water is also thought to play a major role, as a large number of reactive species are created during electron irradiation *[N. M. Schneider et al. (2014)]*. These reactive species may diffuse and react with the immersed sensitive polymers. During the experiments, contrast variations with time can be observed. Figure 15 shows a typical image obtained on a thick sample after a few scans. Although no specific contrast was

observed in the first scan, the PMMA shell is bright – even very bright in a region where a small window was used. This result confirms the reports of D. J. Stokes that scan rate may drastically change the contrast of sensitive materials in suspension mode *[D. J. Stokes et al. (2000)]*.

As the bright shell appears during irradiation and cannot be explained by Monte Carlo simulation, it is attributed to irradiation. We suggest that this contrast originates from the accumulation of charged species such as hydrated electrons at the interface between the latex particle and water. This would be more inclined to occur in the case of thick water film, where the latex particles are completely immersed into water. Indeed, in such case, the interface between latex and water would not be in contact with the gaseous atmosphere and the charges accumulated at the interface could not be compensated by the gas cations. In our case, the irradiation reverses the contrast of shell, moreover it increases quite largely the contrast. Whereas this could be an opportunity to obtain high-resolution topographic, structural, and compositional information from differences between charging and charge detrapping *[G. R. Watt et al. (2000)]*.

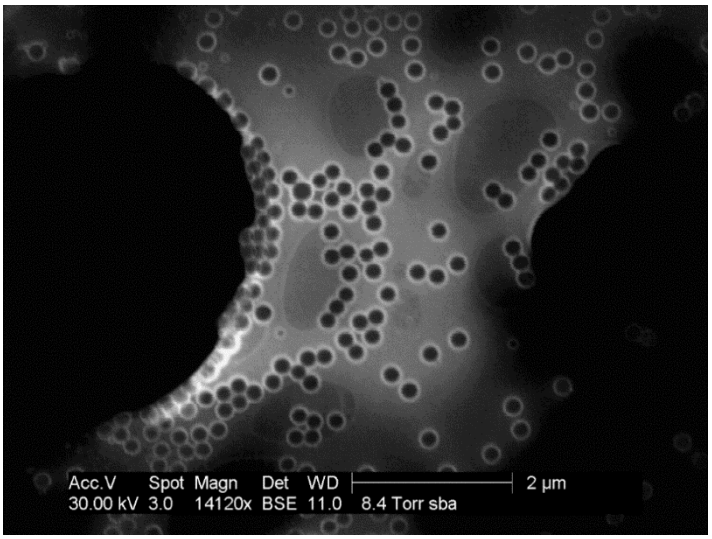

Figure 15. Effect of irradiation on the contrast (brighter shell than the core after a few scans)

Figures 16a, 16c and 16e shows 3 images of the latex particles with different contrasts, obtained before significant irradiation damage. The corresponding grey level profiles for experimental images and simulations along one latex particle are given in Figure 16b, 16d and

16f, respectively. The images have been acquired at different places and thus probably correspond to different water film thicknesses. However, no estimation of the water film thicknesses can be given from the experimental conditions or images. Interestingly, Monte Carlo simulations may provide a fair estimation of the water film thicknesses.

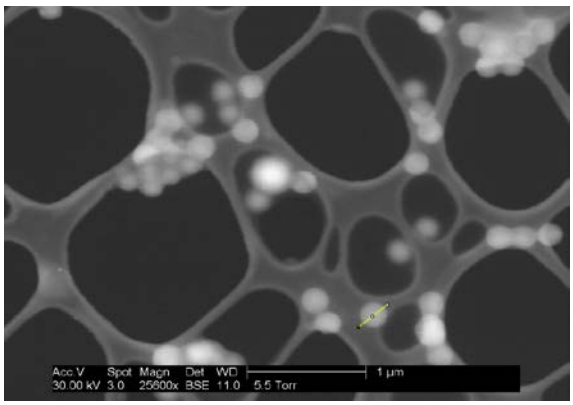

a)

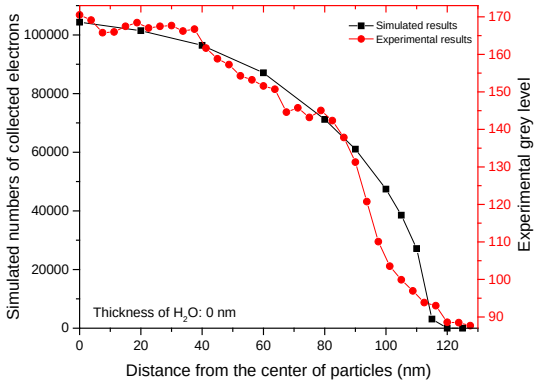

b)

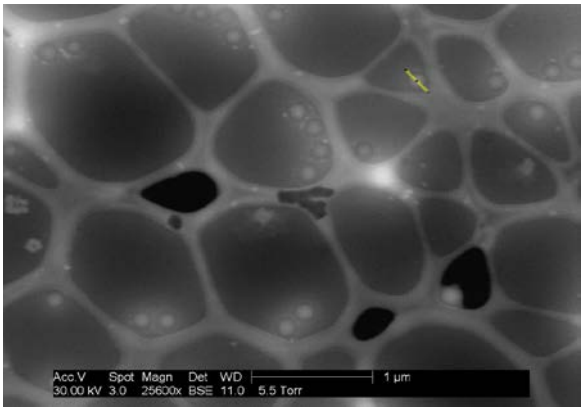

c)

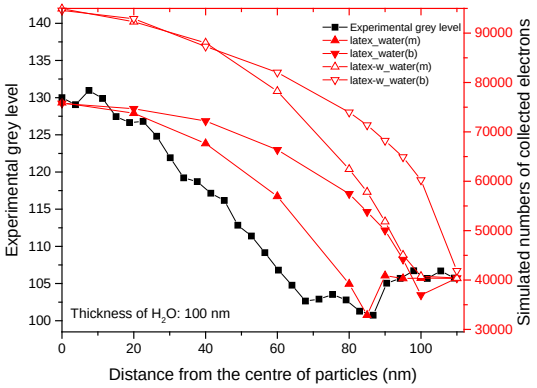

d)

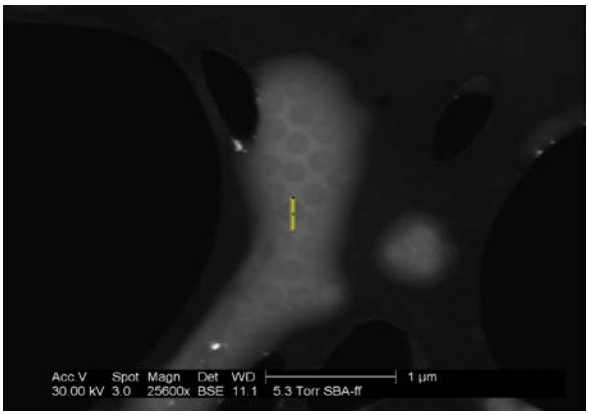

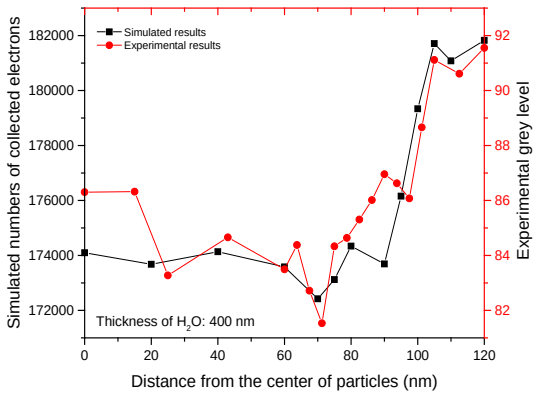

e) *f)*

Figure 16. Comparison between experimental images and Monte Carlo simulation results, on aqueous suspensions of SBA-PMMA latex particles. a) experimental image exhibiting uniform SBA-PMMA particles; b) comparison of experimental and simulated profiles, indicating a dry state (no water); c) experimental image exhibiting a dark PMMA shell surrounding the SBA core, in a dark water film; d) comparison of experimental and simulated profiles, indicating a thin water film (thickness 100 nm). Four different simulations are reported: latex particle placed at the center (◢) or on the top (◤) of a water film, latex particle with a very thin layer of water on its surface, then placed at the center (◿) or on the top (▽) of a water film; e) experimental image exhibiting a dark PMMA shell surrounding the SBA core in a bright water film; f) comparison of experimental and simulated profiles, indicating a thicker water film (thickness 400 nm)

Indeed, for the first image (Figure 16a), the SBA-PMMA latex particles seem to be homogeneous, without any core-shell structure. A very good match is found between the experimental and simulated grey level profiles when considering dry particles (Figure 16b). In Figure 16e, the SBA-PMMA particles exhibit a bright core-dark shell contrast and are immersed in a brighter water film. This corresponds to the case where the water film is thicker than the latex diameter (see Figure 14). A good match is obtained with a water thickness of 400 nm, see Figure 16f. Figure 16c is an intermediate case, with the bright core-dark shell structure immersed in a dark water film. From the simulations in Figure 14, this corresponds to water film thicknesses below 200 nm, this means that the latex particles are not fully immersed in suspension.

Interestingly, when the water film thickness is less than the diameter of the latex particle, several configurations can be simulated, depending on the way that the particles interact with water, as shown in Figure 17. The corresponding 3D models used in the Monte Carlo simulations are displayed in Figure 18. The simulated grey level profile in Figure 16d shows no shell for the model of latex particle with a very thin water layer (10 nm) on the surface. On the contrary, a dark shell is obtained for the model of a latex particle without any other covering. Although not perfect, the best match, for the ESEM image with a dark shell shown in Figure 16c, is obtained with a SBA-PMMA particle placed at the middle of a 100 nm thick water film without any thin layer wetting the latex particle (case in Figure 17b & 18b).

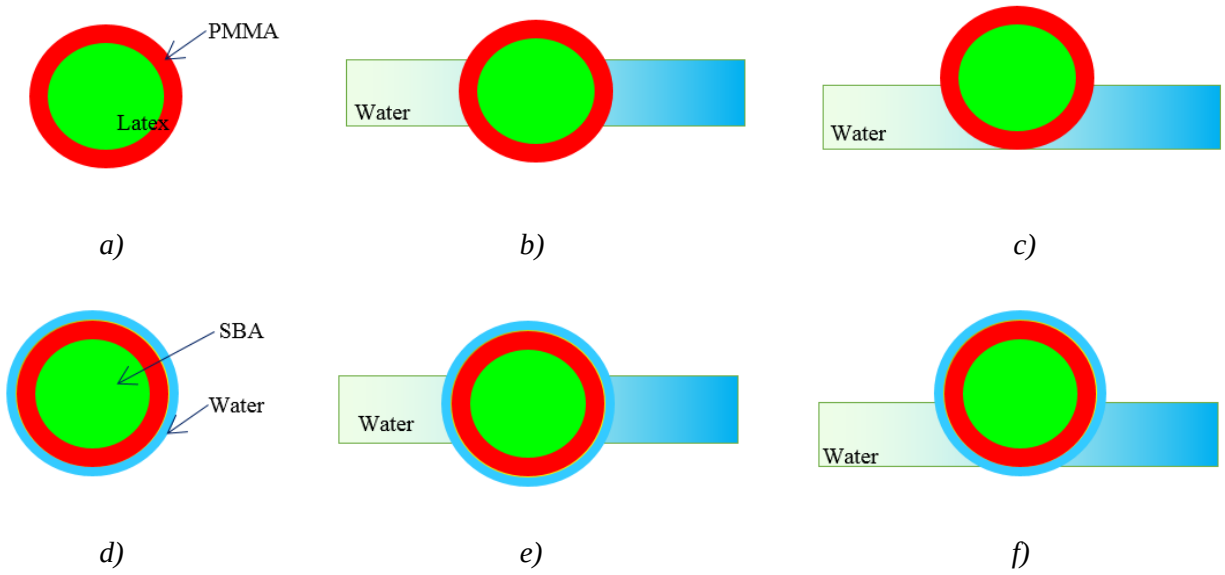

Figure 17. Several configurations simulated for a not fully immersed SBA-PMMA particle, considering a water thickness equal to 100 nm (green-SBA, red-PMMA, blue-water).a) SBA-PMMA particle; b) SBA-PMMA particle at the center of the water film; c) SBA-PMMA particle on the top of the water film; d) SBA-PMMA particle with a very thin layer of water on its surface; e) SBA-PMMA particle embedded into a very thin layer of water and placed at the center of the water film; f) SBA-PMMA particle embedded into a very thin layer of water and placed on the top of the water film

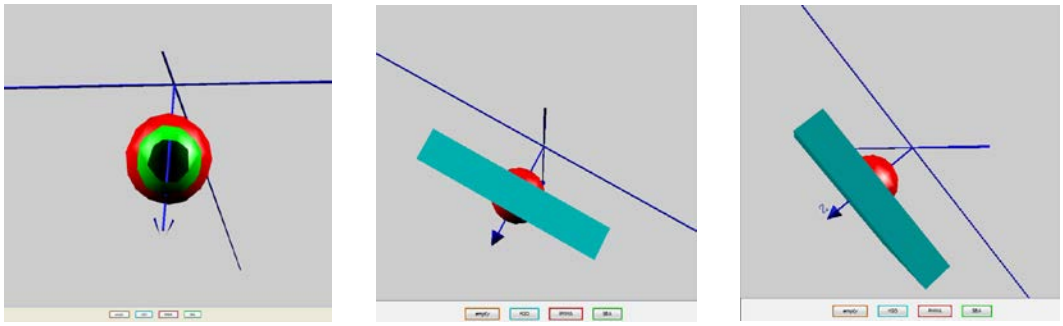

a) *b)* *c)*

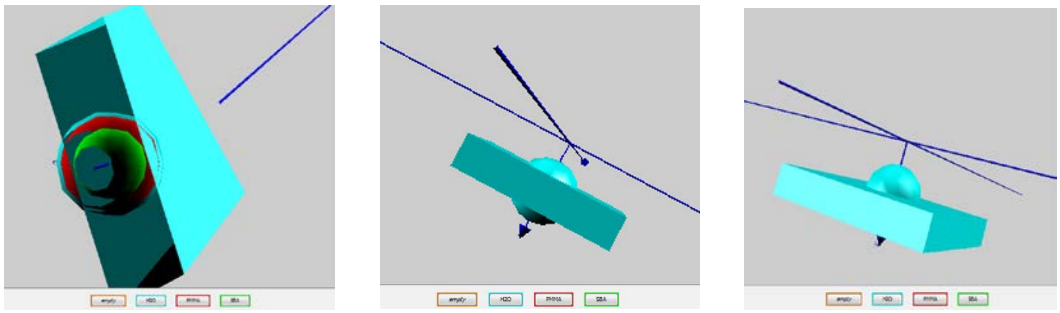

d) *e)* *f)*

Figure 18. 3D model in Monte Carlo simulation, (green-SBA, red-PMMA, blue-water)

a) SBA-PMMA particle; b) SBA-PMMA particle at the center of the water film (corresponding to Figure 17b); c) SBA-PMMA particle on the top of the water film (corresponding to Figure 17c) ;

d) cross-section of a SBA-PMMA particle with a very thin layer of water on its surface; e) SBA-PMMA particle embedded into a very thin layer of water and placed at the center of the water film (corresponding to Figure 17e); f) SBA-PMMA particle embedded into a very thin layer of water and placed on the top of the water film (corresponding to Figure 17f)

This paragraph was dedicated to the SBA-PMMA latex particles in water. In conclusion, simulating such nanoparticles in dilute suspension within low thickness water film provides access to contrast analysis, as well as an estimation of the water film thickness.

3.3 Several nanoparticles in water

From these two examples (gold nanoparticles and polymer latex suspension), a nice agreement is found between Monte Carlo simulations and experimental images obtained with the wet-STEM mode in ESEM. To further understand the relationship between the water film

thickness and the resolution in the images obtained on nano-materials in suspension, simulations were carried on twelve kinds of nanoparticles (C, PE, PBA, SBA, PMMA, PS, PP (LD), PP(HD), Si, SiO_2, Diamond, TiO_2, $CaCO_3$, Al_2O_3, Au).

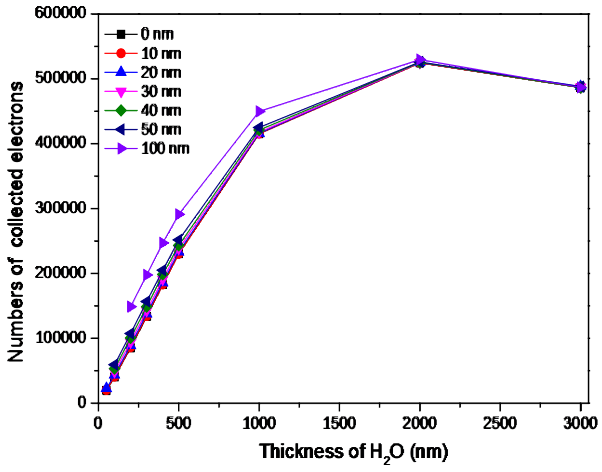

Figure 19. Numbers of collected electrons calculated from Monte Carlo simulations, as a function of the thickness of the water film for different radii of the carbon nanoparticle

Taking carbon with a density equal to 2,27g/cm^3 as an example, Figure 19 represents the simulated numbers of collected electrons for suspensions containing carbon nanoparticles as a function of the thickness of water film, between 0 nm and 3000 nm. Several carbon radii were simulated in the range [0 (pure water), 50 nm] with a 10 nm step, and a bigger size (100 nm) was considered as well.

Similarly to the simulation results of gold nanoparticles, a maximum may occur at a water film thickness around 2000 nm, which means contrast inversion. Besides, when the water film is thicker than 1000 nm, the curves are very close to each other and the contrast between the carbon particle and water is thought too low to be useful STEM-in-ESEM images. Therefore, the relationship between the contrast and the radius of particles is considered only when the water film thickness is less or equal to 1000 nm, as indicated in Figure 20. Half parabola curve may picture the variation of contrast simulated with the particle radius, where the determination coefficients R-square are higher than 99.7%. The parabola equations and the values of R-square are given in Table 1. As the water film thickness increases, the parabola branch opens, thus the value of B and C in the parabola equation decreases.

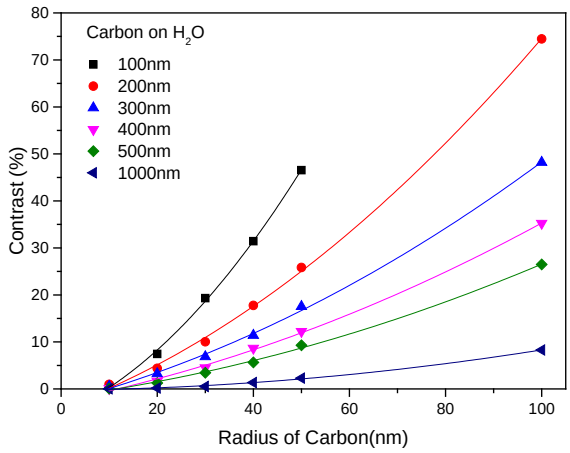

Figure 20. Contrast calculated from Monte Carlo simulations, as a function of the radius of the carbon nanoparticle [10-100nm] in different thicknesses of water film [100 to 1000nm]

When arbitrarily setting a contrast detection limit of 5%, a minimum nanoparticle radius can be defined for each water film thickness from the parabola regression curve in Figure 22. The resolution in the experimental STEM-in-ESEM images is assumed to be equal to this minimum nanoparticle radius. The values obtained with carbon and several other materials are summarized in Table 2.

Table 1. Regression parameters between the simulated contrast and the water film thickness for carbon nanoparticles

Model	Parabola			
Equation	y = A + B*x + C*x^2			
Water thickness	Adj. R-Square		Value	Standard Error
100 nm	0.99821	A	-5.31706	1.67575
		B	0.4404	0.1277
		C	0.01198	0.00209
200 nm	0.99875	A	-4.03816	1.27057
		B	0.37674	0.05796
		C	0.0041	4.95E-04
300 nm	0.99839	A	-2.86432	0.93158
		B	0.27005	0.04249
		C	0.00242	3.63E-04
400 nm	0.99796	A	-2.61586	0.77582
		B	0.20292	0.03539
		C	0.00176	3.02E-04
500 nm	0.99756	A	-1.75489	0.63963
		B	0.13533	0.02918
		C	0.00148	2.49E-04
1000 nm	0.99721	A	-0.27607	0.21957
		B	0.01045	0.01002
		C	7.53E-04	8.55E-05

Table 2. Simulated resolutions with varied water thicknesses on several materials (Contrast ≥5%)

	Water thickness (nm)							
Materials	100	200	300	400	500	1000	Linear Determination coefficient	Exponential Determination coefficient
C	16.2	19.8	24.0	29.8	35.9	77.0	0.9735	0.9996
PE	3.2	8.2	15.7	20.9	30.5	117.0	0.9461	0.9995
PBA	3.9	9.1	20.0	31.0	48.1		0.9542	0.9967
SBA	3.2	9.6	18.5	28.0	42.9		0.9677	0.9985
PMMA	3.3	13.8	28.7	45.5			0.9851	0.9983
PS	3.1	9.9	17.1	25.9	39.2		0.9718	0.9978
PP(LD)	3.7	8.2	14.6	21.0	30.2		0.9791	0.9985
PP(HD)	3.2	9.1	15.6	22.2	32.1		0.9848	0.9971
Si	4.2	7.8	10.0	14.5	17.0	43.1	0.9788	0.9977
SiO_2	5.6	9.2	12.1	15.1	18.0	43.6	0.9775	0.9982
Diamond	17.5	19.4	23.9	29.5	34.1	73.8	0.9654	0.9987
TiO_2	3.2	5.7	8.1	10.0	12.0	25.1	0.996	0.9980
$CaCO_3$	4.3	7.4	9.7	13.9	16.4	39.3	0.9843	0.9983
Al_2O_3	4.1	7.4	9.5	11.7	13.7	31.0	0.9858	0.9958
Au	0.6	1.0	1.6	2.6	3.9	14.8	0.9272	0.9992

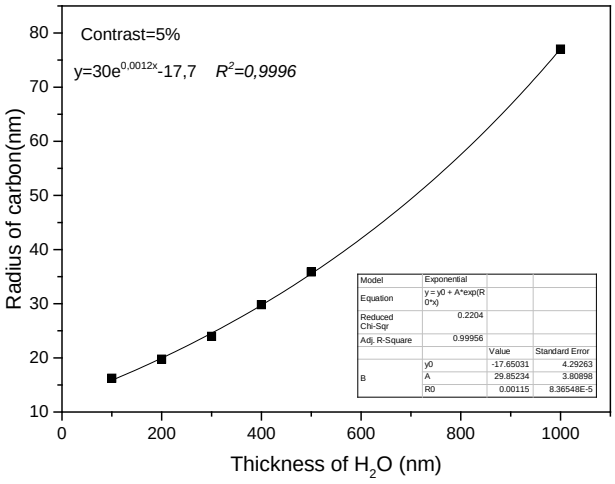

Figure 21. Minimum carbon nanoparticle radius (resolution) calculated from the Monte Carlo simulations with different thicknesses of water

Figure 21 displays the variation of the minimum carbon nanoparticle radius (resolution) as a function of the water film thickness. An exponential law can fit the experimental points, where the determination coefficient equals 0.9996. A very good agreement is also found with the other materials studied.

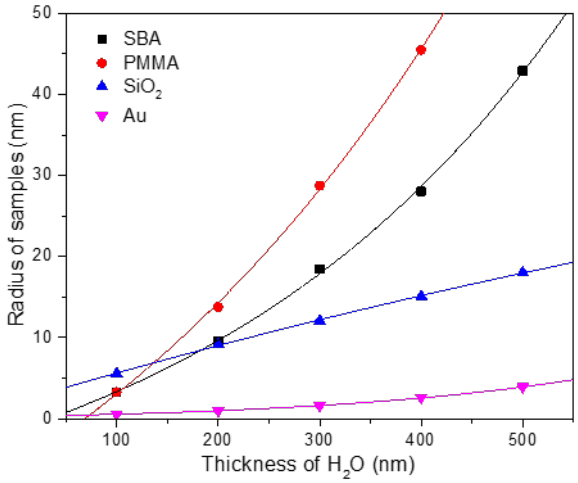

Figure 22. Exponential fits of the minimum nanoparticle radius (resolution) calculated from the Monte Carlo simulations, for four different kinds of materials: SBA, PMMA, SiO_2 and Au, in function of the water film thickness

The coefficients of the exponential law are largely different from one material to the other in our simulations. Figure 22 gives four examples of different kinds of materials, some polymers, a mineral, and a metal: SBA, PMMA, SiO_2 and Au, when considering exponential regressions of the resolution in function of the water film thickness. The regression analysis can also be carried on the resolution in function of either the densities or the effective atomic numbers Z_{eff} *[R. C. Murty (1965)]*. In these cases, the determination coefficients obtained are less than 0.4. As a consequence, from a statistical point of view (level of confidence 95%), it can be concluded that the resolution of nanoparticles totally immersed in water mainly depends on the water film thickness (exponential dependence).

In conclusion, Monte Carlo simulations extended the two first model materials to a list of 14 materials. Parabola and exponential modeling were proposed to depict simulated contrast value as function of particle radius and the minimum particle size could be calculated as function of water film thicknesses. The Monte Carlo simulations therefore allow the determination of coupled data: size range of particles together with maximum water thickness necessary to perform imaging with a fair contrast.

3.4 Conclusions

In this chapter, we presented experimental images obtained on dilute liquid suspensions of gold nanoparticles and SBA-PMMA latex particles, which were obtained with STEM-in-ESEM. These two types of model suspensions have been thoroughly studied combining the experimental images with the Monte Carlo simulations.

With gold nanoparticles, the contrast between the nanoparticles and water changes with the water thickness and the position respective to the water top surface. Gold always appears brighter than water for water film thicknesses less or equal to 1 µm, whereas it is seen darker than water when immersing in thick water film at least equal to 1.5 µm, especially placed close to the top surface. Around 1.4 µm, a contrast inversion occurs and the gold nanoparticles cannot be anymore distinguished from water. Experimentally, the thickness of the water film could be given when contrast inversion occurred but below and above this point, it is not

possible to assess a refine estimation of the water thickness by comparing the simulated and experimental grey level profiles along the gold nanoparticles.

The SBA-PMMA latex particles exhibit a core-shell structure, which is clearly interesting for the contrast analysis. Indeed, thanks to the contrast between the core, the shell and water, it is possible to give a more precise estimation of the water film thickness. Moreover, when the water film is thinner than the diameter of the latex particle, a comparison between the simulated and experimental grey level profiles suggests that the latex particle is placed at the center of the water film, its free surface being not wetted by water.

Twelve nanoparticles of interest were then studied. For each, the value of resolution could be given by determining the minimum size of a particle for which the contrast is at least equal to 5% (for a given water film thickness). Further study on several different kinds of materials using Monte Carlo simulation indicates that the resolution mainly depends on the water thickness. Hence, with the help of Monte Carlo simulation, the water film thickness can be optimized to ensure nanoparticle observation.

References

A. Bogner, G. Thollet, D. Basset, P.H. Jouneau & C. Gauthier. Wet STEM: a new development in environmental SEM for imaging nano-objets included in a liquid phase. Ultramicrosc. 104, (2005), 290-301

A. Bogner, P.H. Jouneau, G. Thollet, D. Basset & C. Gauthier. A history of scanning electron microscopy developments: towards "Wet-STEM" imaging. Micron 38, (2007), 290-401

A. M. Donald. The use of environmental scanning electron microscopy for imaging wet and insulating materials. Nature Materials 2, (2003), 511-516

C. He, and A. M. Donald. Morphology of core - shell polymer lattices during drying. Langmuir 12, (1996), 6250 – 6

C. J. G. Plummer, EPFL, Techniques de l'ingénieur AM3 282

D. B. Peckys, G.M. Veith, D.C. Joy & N. de Jonge. Nanoscale imaging of whole cells using a liquid enclosure and a scanning transmission electron microscope. PLOS one 4 (12) e8214, (2009)

D. B. Peckys, J. P. Baudoin, M. Eder, U. Werner & N. de Jonge. Epidermal growth factor receptor subunit locations determined in hydrated cells with environmental scanning electron microscopy. Scientific Reports 3, (2013), 2626

D. J. Stokes, B. L Thiel, A. M. Donald. Dynamic Secondary Electron Contrast Effects in Liquid Systems Studied by Environmental Scanning Electron Microscopy. Scanning 22, (2000), 357–365

D. Stokes. Principles and practice of variable pressure: environmental scanning electron microscopy (VP-ESEM). Wiley-Blackwell, (2008)

F. M. Ross. Opportunities and challenges in liquid cell electron microscopy. Science 350, (2015), 6267

G. R. Watt, B. J. GRIFFIN, and P. D. KINNY. Charge contrast imaging of geological materials in the environmental scanning electron microscope. American Mineralogist 85, (2000), 1784–1794

J. L. Keddie, P. Meredith, R. A. L. Jones, and A. M. Donald. Film formation of acrylic latices with varying concentrations of non- film-forming Latex particles. Langmuir 12, (1996), 3793 – 801

J. M. Grogan, N. M. Schneider, F. M. Ross and H. H. Bau. The Nanoaquarium: A New Paradigm in Electron Microscopy. Journal of the Indian Institute of Science 92, (2012), 295-308

K. Masenelli-Varlot, A**.** Malchère, **J.** Ferreira, H**.** H**.** Mezerji, S**.** Bals, C**.** Messaoudi and S**.** M**.** Garrido. Wet-STEM Tomography: Principles, Potentialities and Limitations**.** Microscopy and Microanalysis 20, (2014), 366-375

L. Sawyer, D. Grubb & G. F. Meyers. Polymer microscopy. Springer Science & Business Media, (2008)

N. M. Schneider, M.M. Norton, B.J. Mendel, J.M.Grogan, F.M. Ross & H.H. Bau. Electron-water interactions and implications for liquid cell electron microscopy. J. Phys. Chem. C 118, (2014), 22373-22382

R. C. Murty. Effective atomic numbers of heterogeneous materials. Nature 207, (1965), 398-399

U. Golla-Schindler. STEM-unit measurements in a scanning electron microscope. Proceedings of the European Microscopy Congress, Antwerpen. (2004)

Chapter 4: Improvement and calibration of 3D stage

In the previous chapter, diluted suspensions have been successfully imaged with the 2D device in ESEM and the contrast between a single particle and water has been analyzed. However, concentrated suspensions are used in most industries applications, which need 3D characterization to understand their bulk properties. Our home-made 3D device used in ESEM could be used to obtain tilt images not only on solid samples but also on some suspension.

In this chapter, the 3D reconstructed volume of dry polymer film is successfully calculated first. A 3D characterization is then performed on hydrated samples (concentrated latex suspension). Unfortunately, some technical problems were identified when performing tomography on hydrated samples. To overcome those problems, an improvement of the 3D device is proposed, and the optimization of the experimental conditions are further discussed.

4.1 Tomography of PU - carbon nanotubes nanocomposites

An ultrathin section of the Polyurethane (PU) film containing 2 vol % of either ungrafted or grafted carbon multiwalled nanotubes (CNTs), was deposited on a TEM grid, and covered by a droplet containing gold nanoparticles. Then it was placed on the 3D sample holder once the gold suspension was fully dry. As the first acquisitions revealed strong contamination during tilt series acquisition, the 3D stage with the sample was cleaned *in situ* with an Evactron system before each acquisition to avoid contamination. Furthermore, to stabilize irradiation damage before tilt series acquisition, the region of interest was irradiated during 5 minutes by the electron beam. This step is used to avoid shrinking problems during acquisition *[D. T. Grubb, (1974)]*. Although beam damage may induce chemical changes inside the polymer phase, it is thought to have no significant influence on CNTs distribution *[L. C. Sawyer and D. T. Grubb (1987)]*.

Although the sample holder of our 3D device has the ability of rotating over 360°, the tilt series was acquired with tilt angles ranging from 66° to -66° because the sample is flat. Moreover, the accuracy of the 3D device is ± 0.001°, but a constant tilt step of 2° was used to

minimize the acquisition time and thus beam damage. Figure 1 displays the images of the PU films containing grafted and ungrafted CNTs, which were acquired at tilt 0°. The contrast between the bright CNTs and the dark matrix in the images is sufficient to allow the volume reconstruction and the 3D analysis of the CNT dispersion state. The very bright particles, which are randomly dispersed on the surface of the sample, are gold nanoparticles used to help the operator to manually adjust the image focus between each acquisition. It can be noticed that the gold nanoparticles are bigger in the case of the grafted sample because of agglomeration (it is an old suspension).

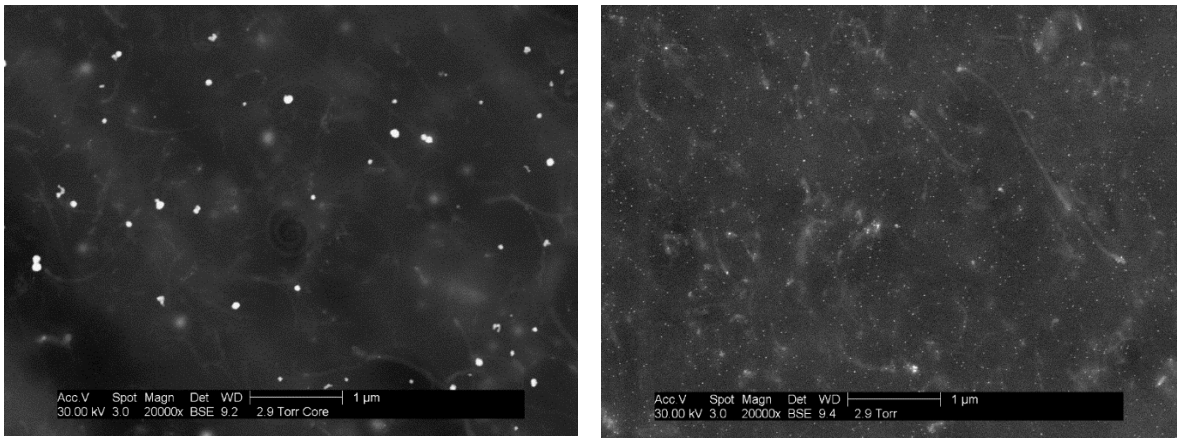

a) *b)*

Figure 1. Acquired images at zero tilt of PU film with 2vol % of a) grafted and b) ungrafted CNTs. The samples have been decorated with gold particles

After the acquisition of projections (images at different tilts), data processing for tomography was carried out by Daya Sagar Dhungana. The alignment was performed in Etomo, with the gold nanoparticles as fiducial markers *[M. Maiorca et al. (2012)]*. The volume was reconstructed using the ART algorithm *[R. Gordon et al. (1970)]* with 15 iterations by TomoJ, a plugin of ImageJ software. Figure 2 shows orthogonal cross sections extracted from the reconstructed volume, where Figure 2a and 2b represent the sample containing grafted CNTs, whereas Figure 2c and 2d correspond to nanocomposites containing ungrafted CNTs. Although limitation is observed in both Figure 2b and 2d as a consequence of the limited tilt range and the non-infinitely small tilt step *[X. Ke et al. (2010)]*, the contrast of the reconstruction results allows the identification of the CNTs within the volume of the sample.

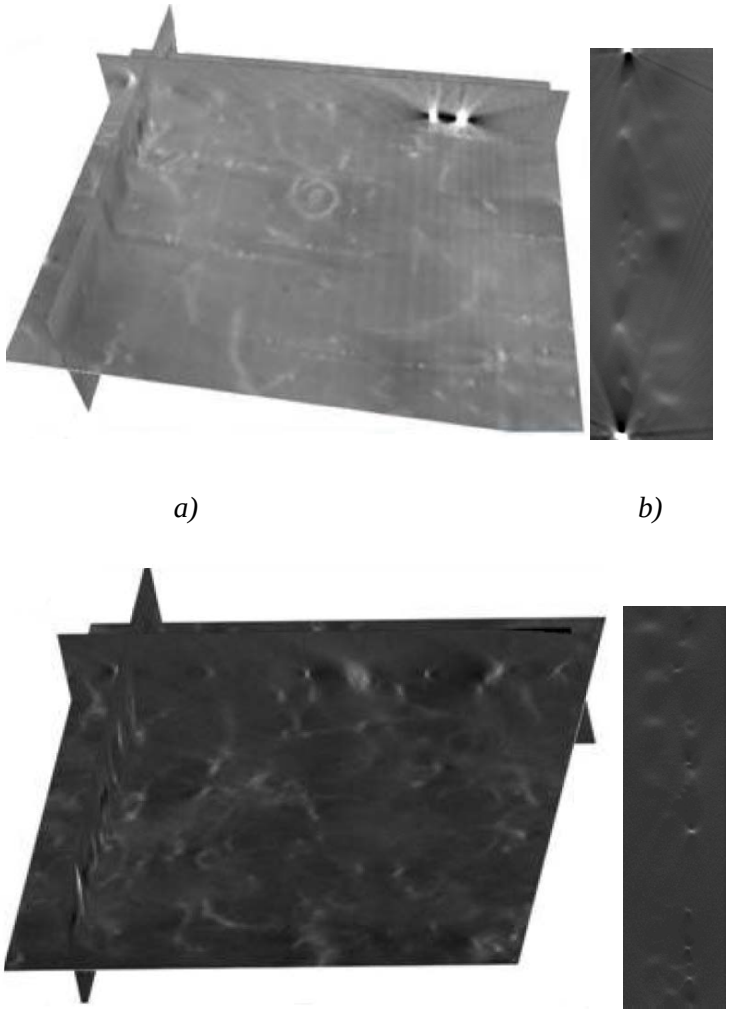

a) *b)*

c) *d)*

Figure 2. Orthogonal cross sections through the reconstructed volumes of the samples: a) and b) XY and XZ cross sections extracted from the volume of the sample with grafted CNTs, respectively; c) and d) XY and XZ cross sections extracted from the volume of the sample with ungrafted CNTs, respectively

The volume reconstruction offers qualitative information, whereas segmentation is a necessary step to get quantitative information. Segmentation was initially performed using Trainable Waka Segmentation, a plug-in in Fiji. The results are shown in Figure 3a for grafted samples and Figure 3b for the ungrafted ones. In order to properly quantify the CNT dispersion and orientation states as well as the contacts between the carbon nanotubes, 3D Slicer (http://www.slicer.org/) was further developed for modeling the nanotubes. The 3D models

after segmentation are displayed in Figure 3c and 3d for the grafted and ungrafted samples, respectively.

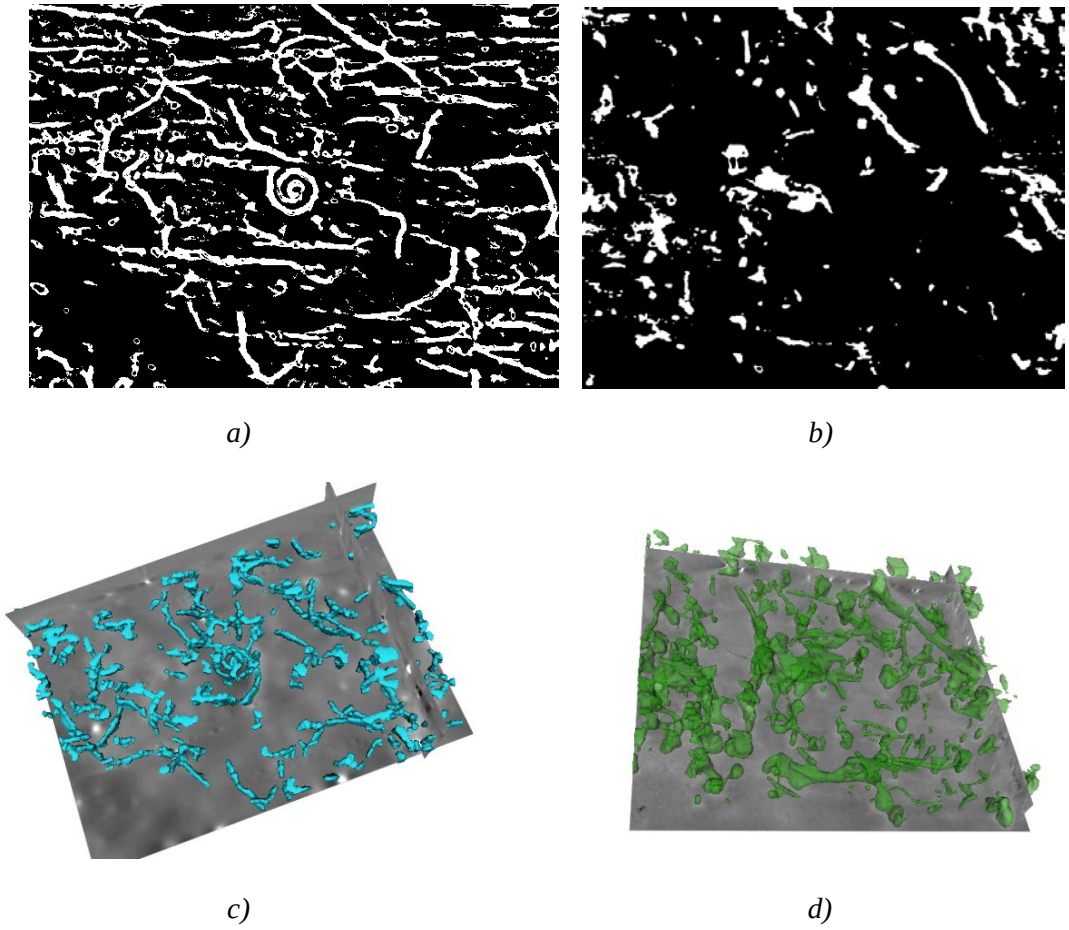

a) *b)*

c) *d)*

Figure 3. Segmentation a) grafted sample and b) ungrafted sample; three dimensional models obtained after segmentation, c) grafted CNTs in blue and d) ungrafted CNTs in green

The gold nanoparticles not only help to adjust the image focus during the acquirement of tilt series and improve the contrast in the images, but can also be successfully used as fiducial markers to align the projections. The residual error mean is only 0.7 and 0.6 pixel for the grafted and ungrafted samples. The slight difference may be caused by the different sizes of the gold nanoparticles. The smaller fiducial markers for the ungrafted samples seems to improve the alignment accuracy due to smaller error of the markers position. Therefore, the size of the marker should be chosen as small as possible in terms of alignment.

On the reconstructed volumes, the thickness of the sample is measured to be approximately equal to 350 and 450 nm for the grafted and ungrafted samples, respectively. The dispersion of grafted CNTs seems to be rather uniform and only small heterogeneities can be seen, whereas in the sample containing ungrafted CNTs, regions with different densities of CNT can be observed. This suggests that grafting has improved the dispersion of CNTs in the PU matrix. Further analysis from the reconstruction and segmentation are detailed in the dissertation of Dr. Mohamed Hedi Jomma *[M. H. Jomaa, (2015)]*.

As a conclusion, the 3D characterization of polyurethane films containing 2 vol % of either grafted or ungrafted CNTs was efficiently performed with the 3D device in the STEM mode. This is possible thanks to the anticontamination procedure, involving de-contamination with the Evactron system and an electron shower prior to the acquisition. Qualitative and quantitative information have been obtained after reconstruction and segmentation. In addition, the use of gold nanoparticles is beneficial especially for the acquisition and the image alignment but it seems that their size plays a role on the alignment accuracy.

4.2 Observation of latex suspension

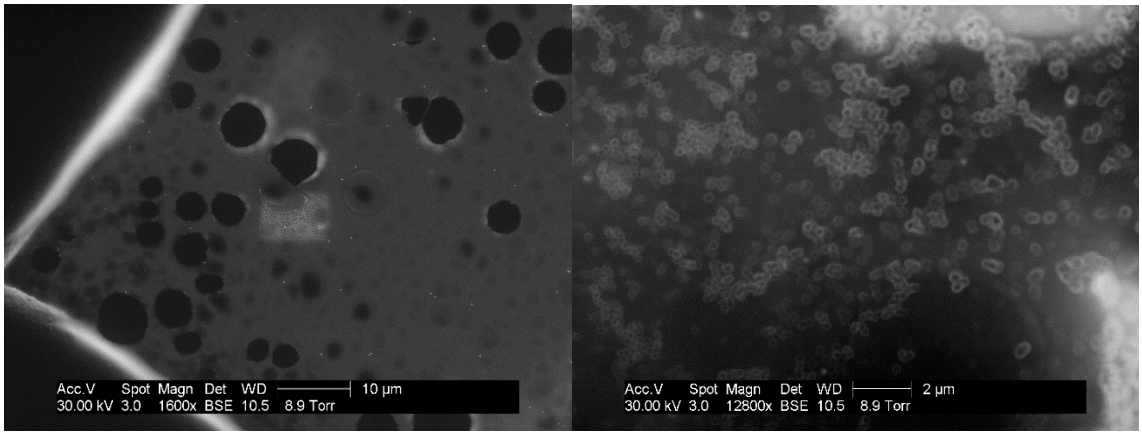

a) *b)*

Figure 4. Images of the latex SBA-PMMA with high concentration in aqueous suspensions: a) low magnification (the black circle is the large hole in the grid); b) high magnification

In chapter 3, the contrast changes between SBA latex and water of varying thickness were studied with the help of Monte Carlo simulation. For this purpose, the samples were imaged

with very low suspension concentrations so that individual latex particles could be observed. On the contrary, in industrial applications, latex is used in high concentrations. Figure 4 displays a concentrated suspension of latex particle observed in 2D. Several layers of latex particles can be distinguished but it reveals difficult to really understand the particles spatial arrangement. In such case, tomography experiments should be of great help.

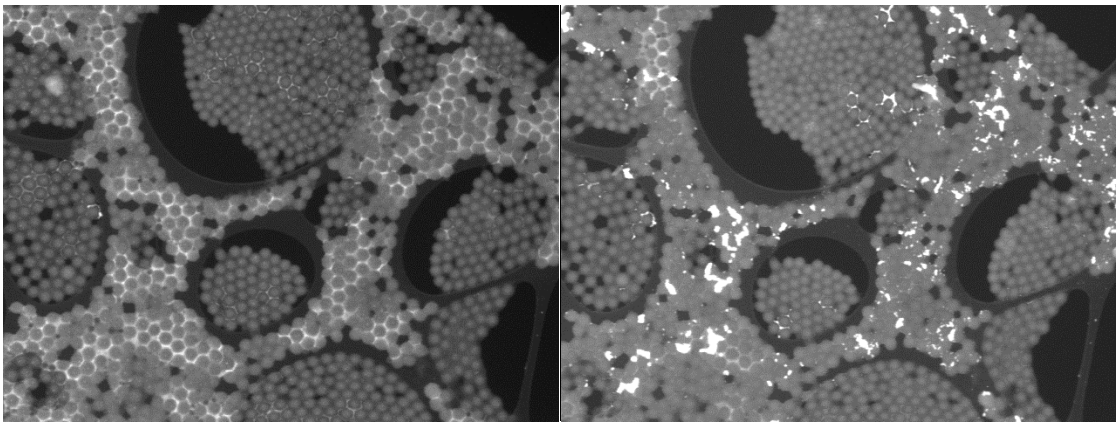

a) *b)*

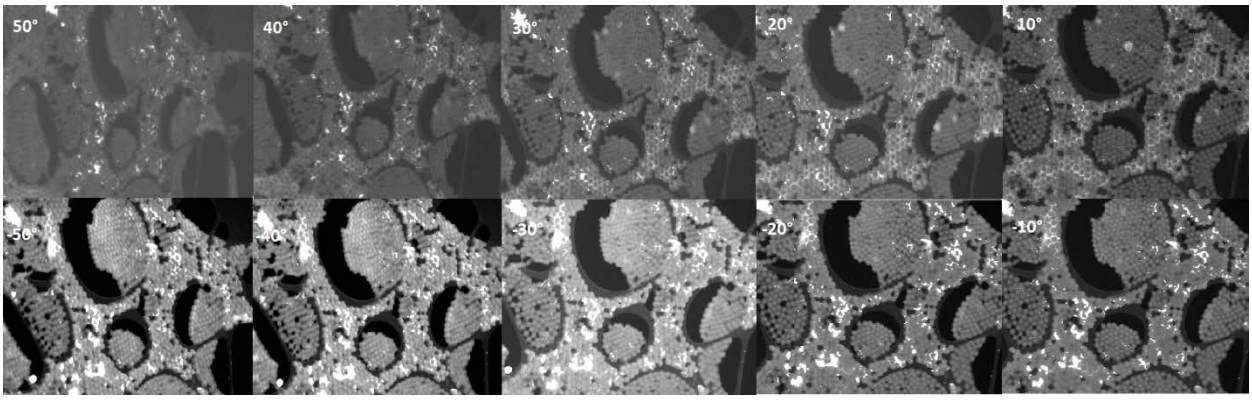

c)

Figure 5. Images obtained on the latex SBA-PMMA: a) and b) at a tilt angel of zero before and after the acquisition of the tilt series, respectively; c) several different tilt angles

The 3D experiments of latex suspensions were similar to those on polymers described before, except that the chamber pressure and sample temperature should be well controlled so as to keep the suspension in the liquid state. The samples are suspensions with nanoparticles of diameter around 200 nm, thus the particles themselves can be regarded as fiducial markers for

alignment. The projections were acquired with tilt angles ranging from 50° to -50°, with a constant tilt step of 5° (large tilt step used to minimize acquisition time, thus irradiation damage and water evaporation) at chamber pressure 8 Torr and setting temperature for sample 8 °C (water gas-liquid equilibrium condition). Figure 5 shows the images of latex acquired with STEM-in- ESEM at several tilt angles. The water between the SBA particles is very bright compared with the TEM grid and the latex particles. There are holes on the TEM grid, which are very dark in comparison with the other parts. Interestingly, the contrasts on the carbon film and in the holes are different, which suggests that it is easier to keep water on the carbon film than in the holes.

However, when comparing with the image at zero tilt before and after the tilt series acquisition (Figure 5a and Figure 5b, respectively), some changes have obviously occurred. For example, the bright water between the latex particles on the carbon film has partially disappeared. Instead, some bright dots with different sizes appeared, as can be seen in Figure 5b. There is a possibility that the surfactants of the latex migrated during water evaporation, and gathered together *[A. Tzitzinou et al. (1999)], [Y. Chevalier et al. (1992)]*. Figure 5c show the images obtained at different tilt angles. The latex particles on the holes have changed their arrangement, and they even come out of the plane of the carbon film. This can easily be observed through the tomography reconstruction.

19 latex nanoparticles were chosen as the fiducial markers for alignment, with the residual error mean 2.0 pixel, and then volume was reconstructed using TomoJ. Figure 6a, 6b and 6c display the YZ, XY and XZ slices of reconstruction volume, respectively. Although a volume could be reconstructed, the reconstruction result has too much artifacts, which could provide inaccurate information. The artifacts can be mainly attributed to water evaporation during the acquisition combined with more usual limitation (missing wedge, large tilt step), but this remains to be confirmed.

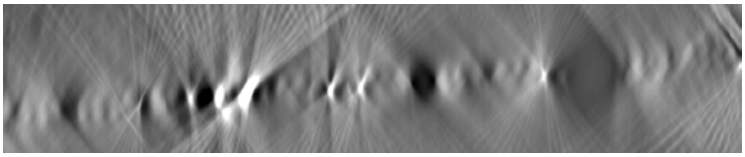

a)

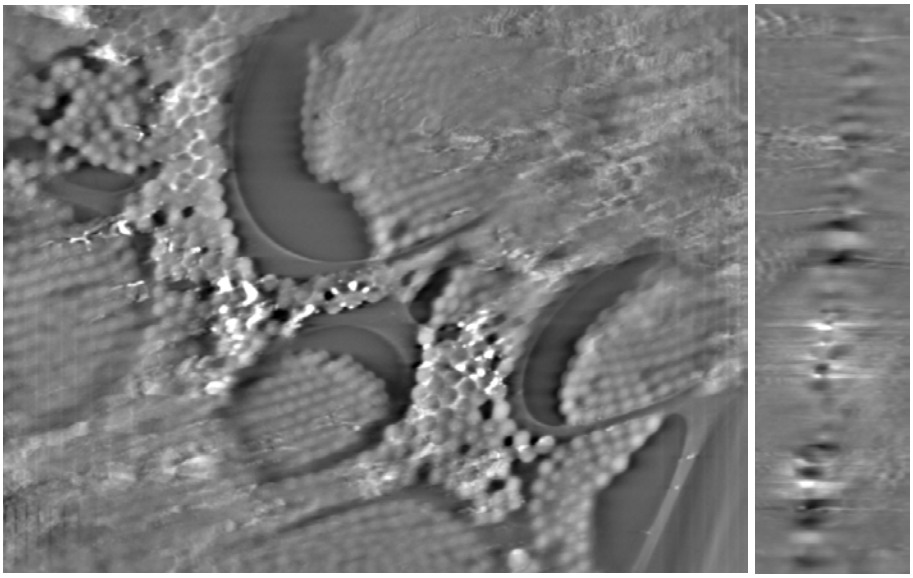

b) *c)*

Figure 6. Tomogram calculated from the projection series of latex SBA-PMMA: a) YZ slices, b) XY slices and c) XZ slices

The phase diagram of water, shown in chapter 2, indicates the requirement of certain pressure and temperature for a given set of thermodynamic conditions *[A.M. Donald, (2003)]*. The points on the curve represent thermodynamic equilibria - evaporation and condensation of water molecules happen simultaneously all the time, whereas the net liquid-vapor ratio is kept constant, which is called as 100% relative humidity (RH). Any deviations from the curve will cause either evaporation or condensation of water. During the ESEM experiments, water evaporation, condensation and keeping in equilibrium can be realized by controlling the temperature of sample holder with the Peltier stage and setting the pressure of microscope chamber. However, the first tomography experiment on suspension presented above shows that serious water evaporation happened during images acquisition even with setting temperature and pressure for 100% RH. It can also be seen on Figure 7, where images have been taken at the setting temperature, given by the controller, for sample 5°C (corresponding

to 6.5 Torr for 100% RH). The bright squares on the right of Figure 7a disappeared after several minutes, as shown in Figure 7b. This means that water evaporated even though the pressure was increased from 6.4 Torr to 6.9 Torr. As a conclusion, the equilibrium conditions are fulfilled at a higher pressure and thus the actual temperature of sample is not equal to 5°C. Hence, the improvement of the 3D device is required.

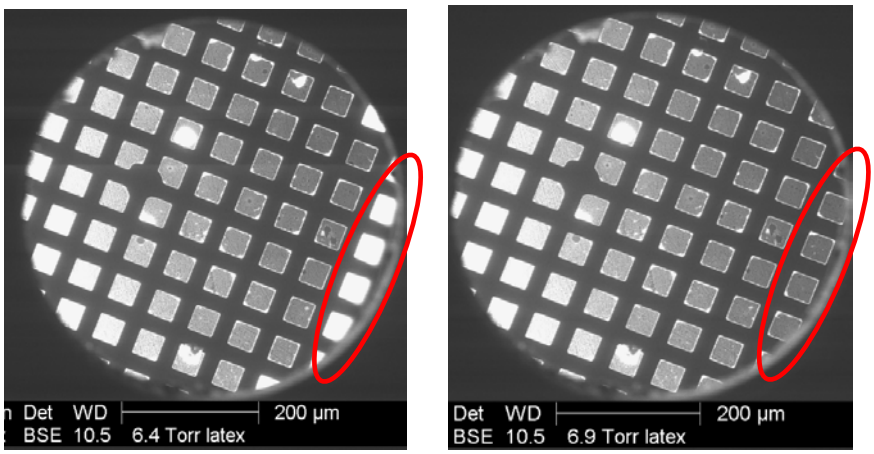

a) *b)*

Figure 7. Images of latex SBA-PMMA acquired with setting temperature at 5 °C, under different chamber pressure: a) 6.4 Torr, b) 6.9 Torr

4.3 Optimization of the experimental conditions

The chamber pressure is controlled by the microscope control system, which behaves as expected for usual experiments. Therefore, the main problem most probably comes from the measurement and/or the control of the temperature within our 3D device. During the experiments, water film and some water droplets were found on the surface of the Peltier stage, as demonstrated in Figure 8, and they remained until the end of the experiments. As described in Chapter 2, the Peltier stage placed vertically between the piezoelectric systems and the sample holder is used to adjust the temperature of sample. As water preferentially condenses on the coldest points, it is suggested that the sample temperature is higher than the Peltier stage temperature.

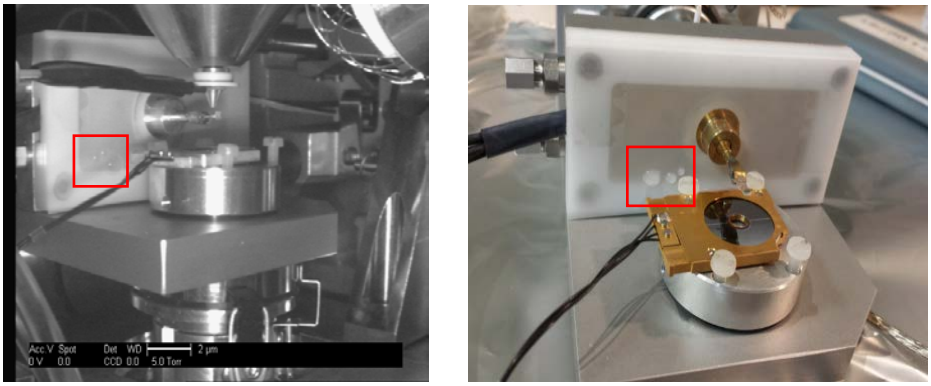

a) *b)*

Figure 8. Images of 3D device: a) during and b) after the tomography experiments

A further proof is given by temperature measurements. A thermocouple was placed directly on the Peltier stage and another one on the sample holder. Under a pressure of 2.5 Torr, it was found that the temperature of the controller was greatly different from the temperature measured on Peltier stage and that of the sample holder, as can be seen in Figure 9. There is a possibility that the measurement error increase the difference. Nevertheless, the design of the 3D device seems to be the issue as the cold is not efficiently transferred from the Peltier stage to the sample.

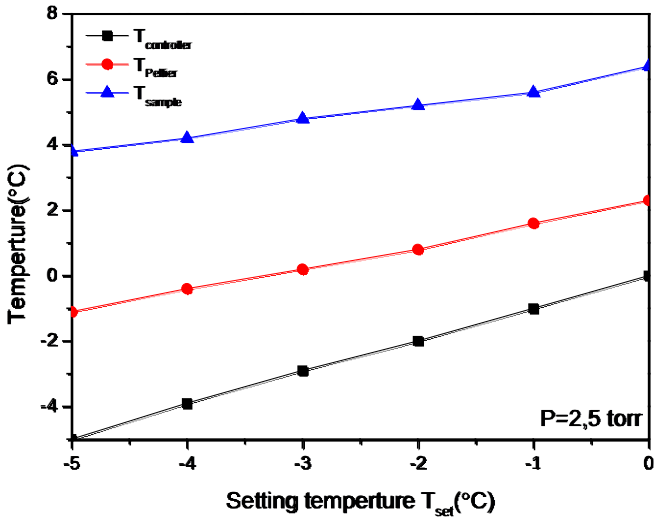

Figure 9. Three different temperatures under the pressure 2.5 Torr, $T_{controller}$ - temperature of FEI controller; $T_{Peltier}$ - temperature of Peltier stage; T_{sample} - temperature of sample holder (close to the sample)

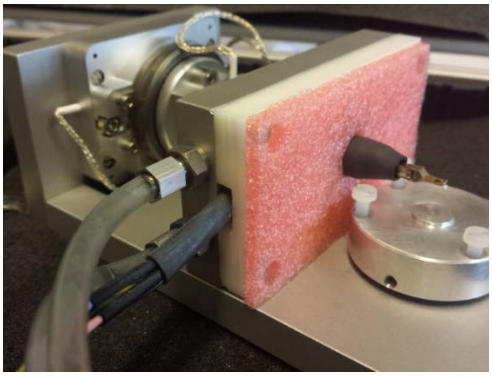

Figure 10. Images of 3D device after adding thermal insulation material on the surface of Peltier stage and the sample holder

The first improvement concerns the addition of a thermally insulating material to diminish the cold losses. It was added on the surface of Peltier stage and on the sample holder, as shown in Figure 10.

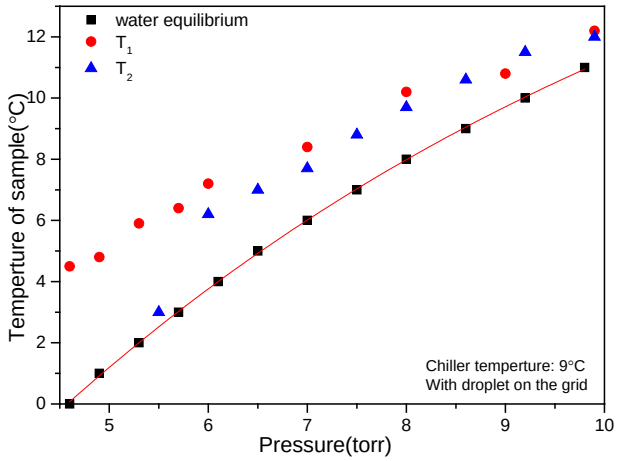

Figure 11. Comparisons of the sample temperatures with the water equilibrium temperatures under certain pressures. T_1, T_2 - temperature of sample holder (close to the sample)

Figure 11 shows a comparison of the sample temperatures with the water equilibrium temperatures under several chamber pressures after adding thermal insulation material to 3D stage. T_1, T_2 represent two measures of the sample temperature with the thermocouple placed between the tweezers. The temperature of water in the chiller, circulating into the Peltier stage, was also decreased to 9 °C instead of 15 °C. After adding the thermal insulation material on

the 3D device, the temperature of the sample holder is closer to the expected value, but still need further improvement. On one hand, the position of the sample on the holder is a little far away from the Peltier stage, the thermosteresis during conduction making the sample temperature higher than that of Peltier stage. On the other hand, the poor contact between the thermocouple and the tweezers of the holder still results in slight measurement errors (see the differences between the values of T_1 and T_2 on Figure 11). Therefore, a further optimization is still requested.

In the light of these measurements, a new sample holder was designed by José Ferreira and his team in MATEIS, as shown in Figure 12. The new sample holder was thicker and was made of materials with better heat conduction properties, which should make the temperature of sample very close to that of Peltier stage. Furthermore, a small hole very near to the position of sample in the holder is created to place a thermocouple. This will be used to get a more accurate measurement of the sample temperature.

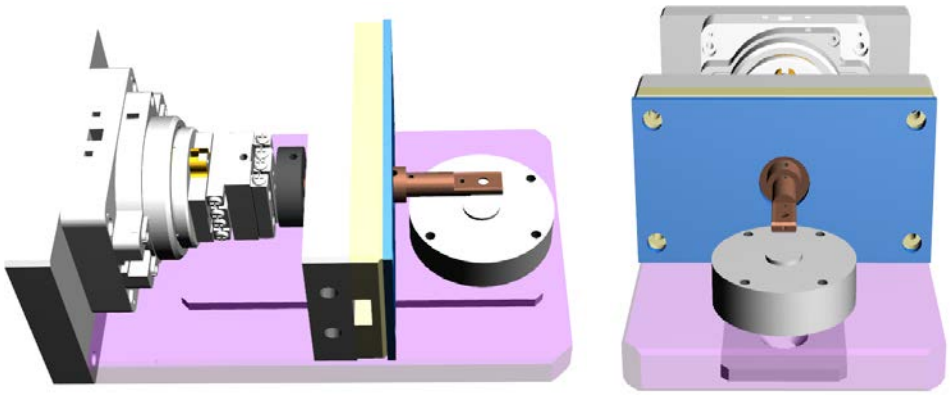

a) *b)*

Figure 12. Images of 3D device with a new sample holder: a) planform of side view; b) front view

Figure 13 compares the temperature of the new sample holder (T_1, T_2) with the relative water equilibrium temperature T_{equ} for several values of the chamber pressure. It can be seen that the measurement of the sample temperature is now fairly reproducible. Moreover, the difference between the measured sample temperature and the value of expectation is much smaller, and part of which might be a consequence of the measurement error. In addition, this

difference decreases when increasing the pressure of microscope chamber, which means the sample is prone to keep in balance between water evaporation and condensation when the experiments are performed at relative high chamber pressure and sample temperature.

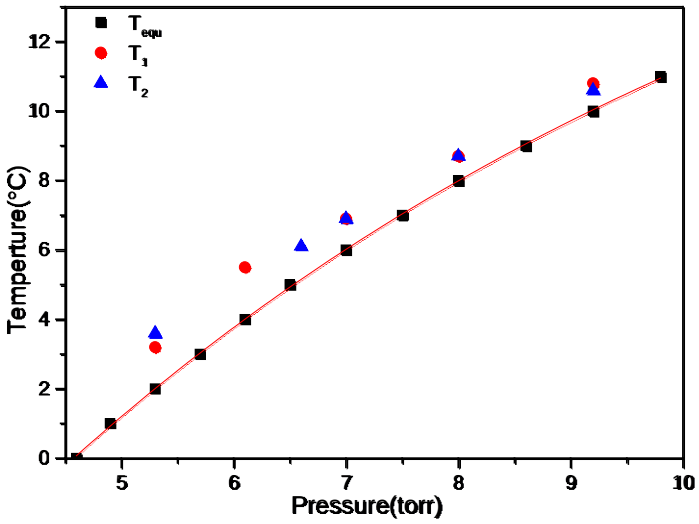

Figure 13. Comparisons of the sample temperatures, measured using the new holder, with the water equilibrium temperatures under certain pressures. T_1, T_2 *- temperature of sample holder (measured with the thermocouple inside the hole very close to the position of the sample),* T_{equ} *- Temperature of water at equilibrium state*

4.4 Tomography of latex suspension with optimized experimental conditions

With the improved 3D device and a better understanding on how to control the environmental conditions, a series of images on more concentrated SBA-PMMA suspension was acquired on a region of interest where the nanoparticles are arranged in two layers, as presented in Figure 14. The projections were acquired within one hour (total acquisition time) at tilt angles ranging from 55° to -55° with a constant tilt step of 5°. In comparison with the images obtained at a tilt angle of 0° before and after the projections acquisition, Figure 14a and 14b, no large change such as water evaporation can be observed apparently, apart from somewhat variations in the grey level. These contrast changes may be attributed to changes in the acquisition settings (brightness, contrast), but might also be caused by irradiation damage. Note that the imaging conditions were also optimized to reduce irradiation damage. For example, for each tilt angle,

the focus, contrast and brightness in the images were not adjusted directly on the region of interest but in a region located nearby, on the tilt axis. Aside from the contrast variations, a nice projection series were acquired, see Figure 14c.

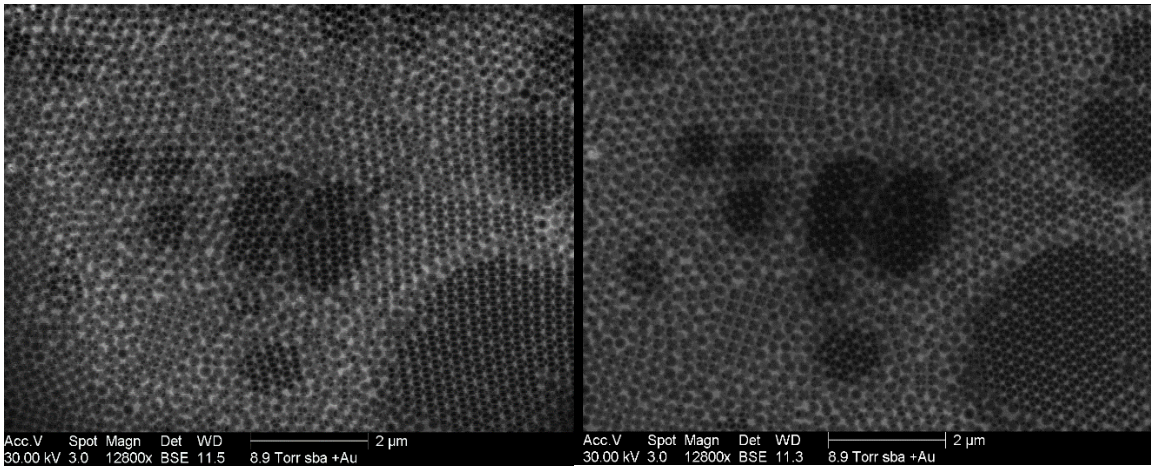

a) *b)*

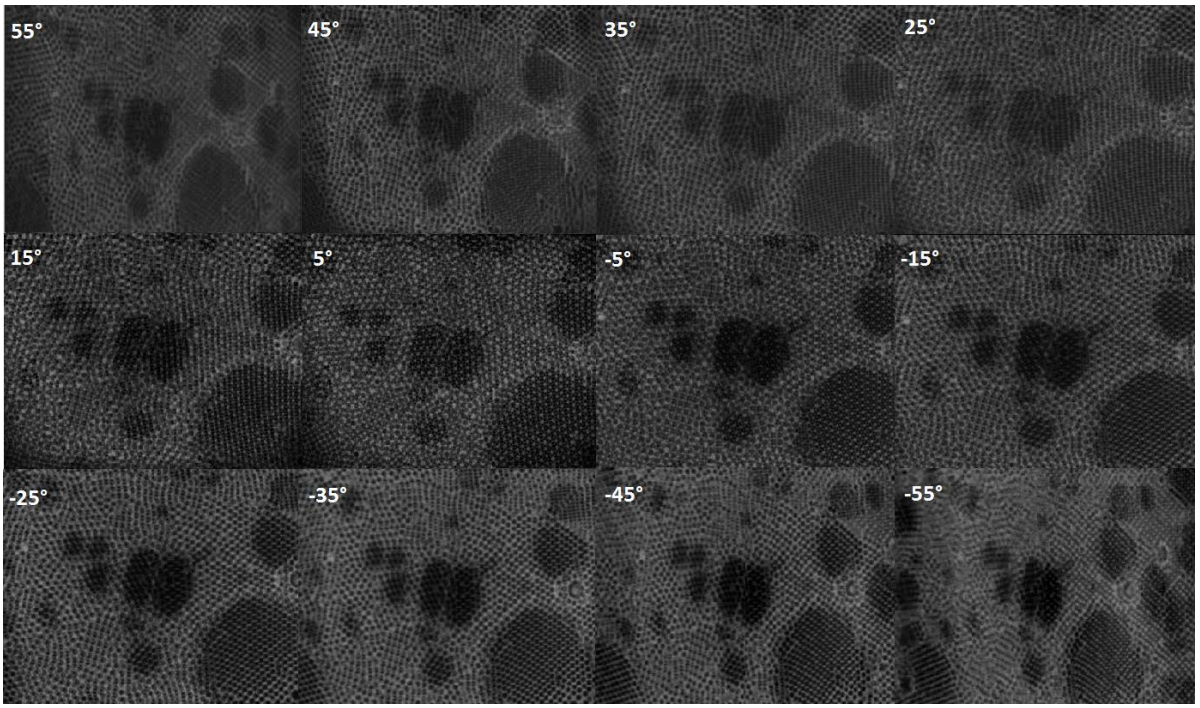

c)

Figure 14. Images obtained with optimized experimental conditions on the latex SBA-PMMA: a) and b) at a tilt angles of zero before and after the acquisition of the tilt series, respectively; c) several different tilt angles

As it has been discussed for Figure 5, the latex particles themselves can be regarded as markers to align the tilt images. Alignment with the latex particles as fiducial marker becomes however much more difficult for the more concentrated suspension, where two or more layers of particles arrange closely, as the case in Figure 14. Moreover, according to the results obtained on the PU films, the smaller markers are better for an accurate alignment, so a good choice is using gold nanoparticles as markers. In case that the suspension with gold nanoparticles influences the interaction between SBA and the surfactants in our latex suspension, the droplet with gold nanoparticles (with a diameter around 10 nm) has been deposited on the TEM grid at least one day before the tomography experiments. Figure 15a shows the image of TEM grid with gold nanoparticles before the droplet containing latex particles was placed. The pressure was set to 3.4 Torr as the grid is dry. The gold nanoparticles are brighter than the holey carbon film and it can be seen that they are randomly dispersed on the grid surface. The image in Figure 15b was obtained after the deposition of a droplet of the diluted latex suspension. The latex particles are isolated from each other, and bright gold nanoparticles can be observed.

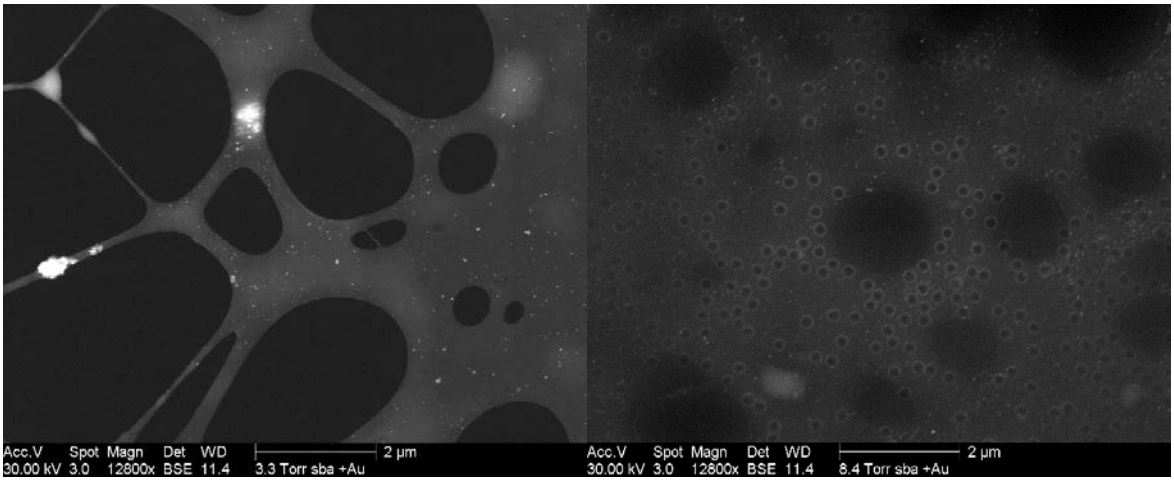

a) *b)*

Figure 15. ESEM images with gold nanoparticles deposited on the TEM grid: a) without SBA suspension on the grid; b) with SBA suspension on the grid

However, when analyzing a more concentrated suspension, the gold nanoparticles cannot be seen when there are two or more layers of SBA particles, as the case in Figure 14 (gold particles with diameter around 10 nm have already covered the grid before latex droplet being

deposited but lose resolution). As a result, small gold nanoparticles cannot be efficiently used as fiducial markers for much concentrated latex suspension. At the same time, the alignment performed with the latex particles is more difficult and time-consuming. Thanks to one way of fiducial model generation in Etomo, “use patch tracking to make fiducial model”, the tracking with a number of 850 was used to align this image series. However, this method is influenced greatly by the quality of acquired image series. The good news is that the alignment result obtained by using patch tracking is good enough for the reconstruction of this image series, with residual error mean 0.8 pixel.

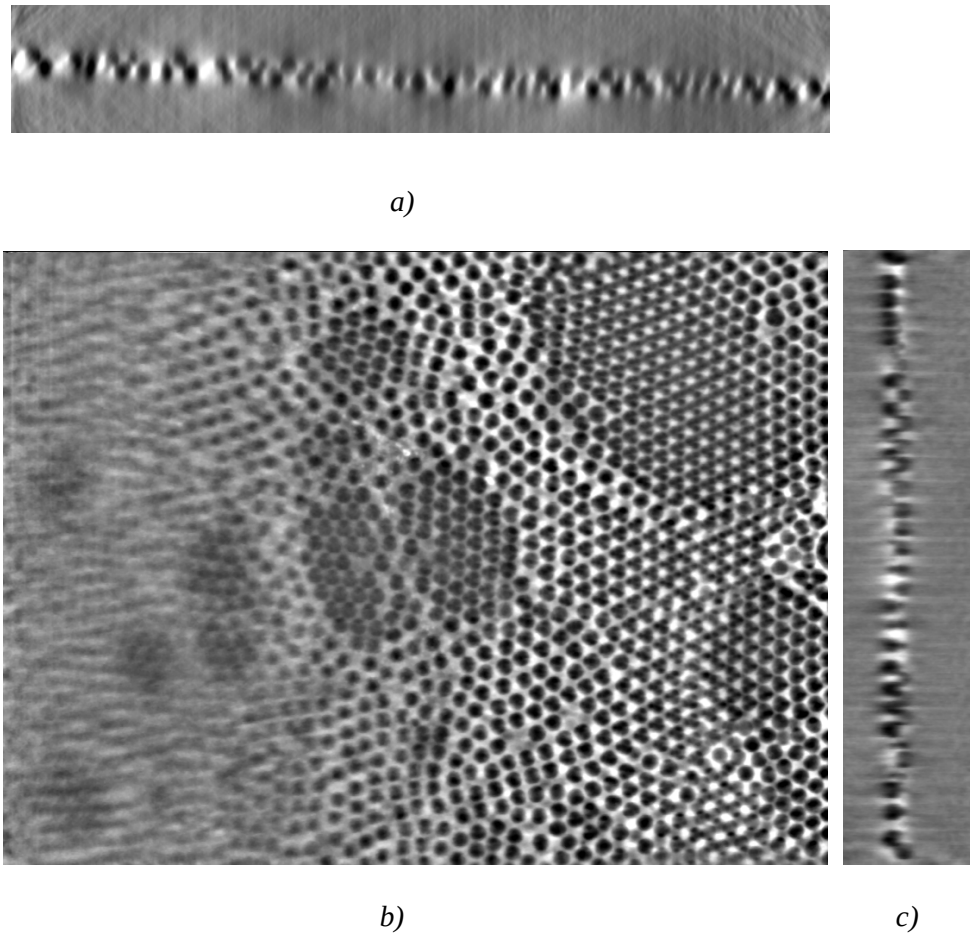

a)

b) *c)*

Figure 16. Tomogram calculated from the projection series of latex SBA-PMMA with optimized experimental conditions, the volume: X×Y×Z = 9585×7170×3000 nm^3. a) YZ slices, b) XY slices and c) XZ slices

Figure 16 presents XY, YZ and XZ slices of the tomogram calculated from the projection series shown in Figure 14 (tilt range from 55° to -55°, tilt step 5°). Despite the fact that artifacts still exist, mainly caused by the large tilt step, further analysis could be well performed to understand the arrangement of the particles within one layer and between two layers. This will be discussed in details in the next chapter.

4.5 Conclusion

In this chapter, we have shown that it is possible to characterize soft materials and hydrated samples in 3D thanks to our home-made 3D device used in ESEM. Firstly, projection series of dry polyurethane films containing either ungrafted or grafted carbon multiwalled nanotubes have been acquired. Further information was discussed from the results of volume reconstruction and segmentation.

Secondly, tomography experiments were performed on a latex SBA-PMMA suspension. Unfortunately, severe water evaporation occurred during the acquisition of tilt images, which resulted in bad tomogram results. A highly refine control of the sample temperature and environment pressure is indeed needed for hydrated materials, especially for aqueous suspensions, which may be the most critical type of sample, because water are highly prone to evaporate without correct handlings. An optimization of the experimental conditions has thus been proposed.

In the 3D device, the optimization concerned a new design of the sample holder. The temperature of the sample could be controlled more finely with the new 3D device and a proper setting of the Peltier stage chiller temperature. With these optimized conditions, a series of images on a region with two layers SBA-PMMA nanoparticles has been obtained. Despite probable irradiation damage, the volume could be efficiently reconstructed. Therefore, we have demonstrated that 3D characterization using STEM-in-ESEM was possible not only on dry materials but also on suspension including nanoparticles.

References

A. C. Nelson. Scanning electron microscope for visualization of wet samples. US Patent 4,720,633, (1988)

A. J. Kubis, G. J. Shiflet, D. N. Dunn & R. Hull. Focused ion beam Tomography. Metallurgical Mater Trans A 35A, (2004), 1935-1943

A. J. Koster, U. Ziese, A. J. Verkleij, A. H. Janssen & K. P. De Jong. Three-dimensional transmission electron microscopy: A novel imaging and characterization technique with nanometer scale resolution for materials science. J Phy Chem B 104, (2000), 9368-9370

A. L. Fletcher, B. L. Thiel & A. M. Donald. Amplification measurements of alternative imaging gases in environmental SEM. J Phys D: Appl Phys 30, (1997), 2249

A. M. Donald. The use of environmental scanning electron microscopy for imaging wet and insulating materials. Nat. Mater. 2, (2003), 511-516

A. Tzitzinou, P. M. Jenneson, A. S. Clough, J. L. Keddie, J. R. Lu, P. Zhdan, K. E. Treacher, R. Satguru. Surfactant concentration and morphology at the surfaces of acrylic latex films. Progress in Organic Coatings 35, (1999), 89-99

D. Blavette, A. Bostel, J. M. Sarrau, B. Deconihout & A. Menand. An atom probe for three-dimensional tomography. Nature 363, (1993), 432-435

D. T. Grubb. Radiation damage and electron microscopy of organic polymers. Journal of Materials Science 9, (1974), 1715-1736

E. Maire, J. Y. Buffiere, L. Salvo, J. J. Blandin, W. Ludwig & J. M. Letang. On the application of X-ray microtomography in the field of materials science. Adv Eng Mater 3, (2001), 539-546

L. C. Sawyer and D. T. Grubb. Polymer Microscopy, ISBN 0412257106, (1987), 62-70

J. J. Mancuso. Large volumes at high resolution using serial block face imaging in the SEM. Microsc Microanal 18(S2), (2012), 104-105

M. H. Jomaa. Elaboration, characterization and modeling of electroactive materials based on polyurethanes and grafted carbon nanotubes. PhD thesis, (2015)

M. Maiorca, E. Hanssen, E. Kazmierczak, B. Maco, M. Kudryashev, R. Hall, H. Quiney, L. Tilley. Improving the quality of electron tomography image volumes using pre-reconstruction filtering. J Struct Biol. 180, (2012), 132-42

R. Gordon, R. Bender & G.T. Herman. Algebraic Reconstruction Techniques (ART) for three-dimensional electron microscopy and X-ray photography. J Theor Biol A 29, (1970), 471-481

X. Ke, S. Bals, D. Cott, T. Hantschel, H. Bender, and G. V. Tendeloo. Three-Dimensional Analysis of Carbon Nanotube Networks in Interconnects by Electron Tomography without Missing Wedge Artifacts. Microsc. Microanal. 16, (2010), 210–217

Y. Chevalier, C. Pichot, C. Graillat, M. Joanicot, K. Wong, J. Maquet, P. Lindner, and B. Cabane. Film formation with latex particles. Colloid Polym Sci 270, (1992), 806-821

Chapter 5: Application to 3D characterization of latex suspensions

In chapter 4, our home-made 3D device has been improved to better control the temperature of liquid samples, and a satisfying reconstruction has been obtained from an image series of concentrated latex suspensions. In this chapter, a full 3D analysis on latex SBA-PMMA in different concentration states is first performed. The particles arrangement in the concentrated suspension gained with our 3D device is compared with the one obtained with cryo-SEM images analysis. A 3D characterization on latex with surfactant XPCAS 803 is then carried out. In the end, the influence of irradiation on hydrated samples during the acquisition of tilt series is discussed.

5.1 Tomography on latex (SBA-PMMA) suspensions

5.1.1 Dilute latex suspension

A tilt series on an angular range of 60° with projections taken every 5° was obtained from a dilute latex suspension at the pressure of 5.3 Torr and sample temperature 2 °C (Figure 1a). The total acquisition time of 25 images is 70 min, which makes that the mean acquisition time of one image is about 168s. As shown in Figure 1a, dark latex particles are dispersed in the bright water film held by TEM carbon film. The very big black holes, as holes 1 and 2 on the left part of the image, correspond to holes in the carbon film. They are very dark due to the absence of water covering the holes. Some small holes in the carbon film (as hole 4) are still covered by water film, as they appear quite bright compared with the big holes. From the contrast variation (Figure 1c), it seems that thickness of the water film is more or less constant from the side to the center of the small holes. The holes with a medium size (as hole 3) is still covered with water but since the grey level decreases from the side to the center of the hole (Figure 1b), the thickness of the water film decreases. Indeed if the water film was not continuous, it would not be stable.

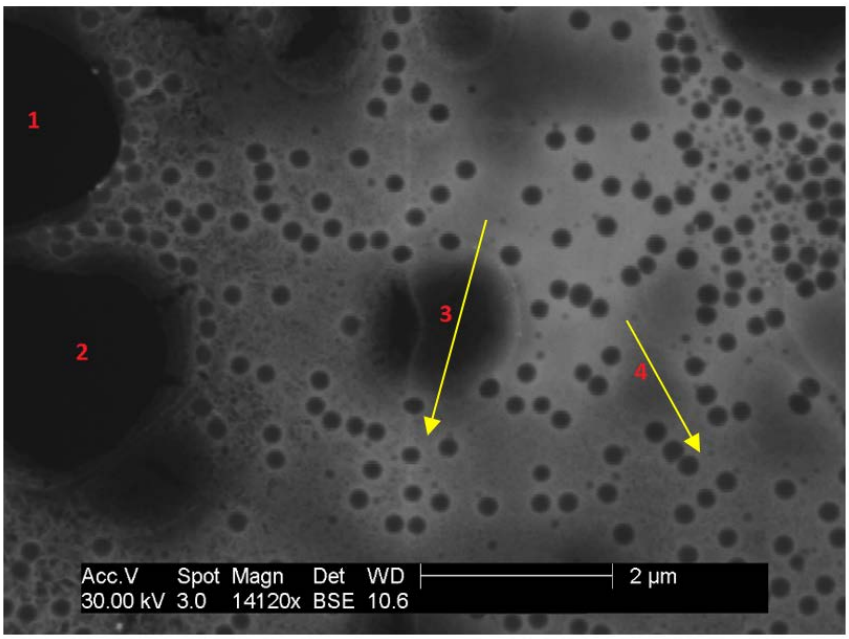

a)

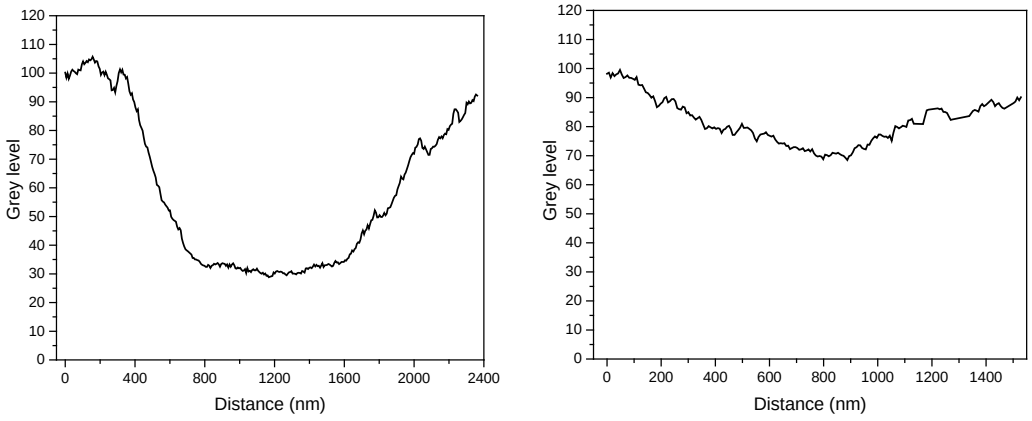

b) *c)*

Figure 1. a) Acquired image at zero tilt of dilute PMMA-SBA latex suspension. Depending on the size of the holes, they are covered with water (for medium and small holes, as 3 and 4) or not (for large holes, like 1); b) and c) the plot profiles along the yellow lines of hole 3 and 4, respectively

24 latex particles on the carbon film were chosen as fiducial markers to help the alignment of this image series. The residual error of the alignment result is equal to 1.5 pixels, which may mainly result from the large size of the fiducial markers (latex particles) as discussed in chapter 4, and from the possible movement of the water on the holes. On one hand, the water on the

holes is prone to evaporate, even if the tilted image series are obtained in a comparatively stable water gas-liquid equilibrium environment. On the other hand, the water film on the holes may tend to withdraw towards the carbon film due to surface tension. These may change the position of the particles on the carbon film, in particular those close to the holes, as consequence the residual error in alignment. Figure 2 shows XY, YZ and XZ slices of the tomogram reconstructed from projection series after alignment.

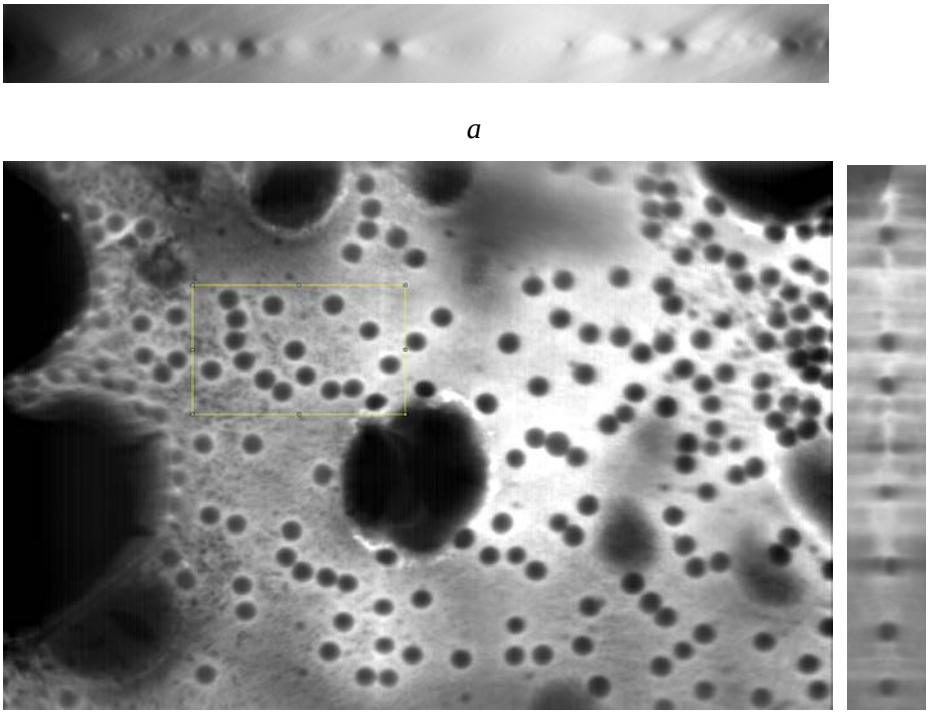

a

b *c*

Figure 2. Tomogram calculated from the tilt series of dilute latex suspension, the volume: X×Y×Z = 8656×6368×2720 nm^3. a) YZ slices, b) XY slices and c) XZ slices. The yellow box (volume: X×Y×Z = 2180×1380×1020 nm^3) is the selected region for further analysis

Segmentation was performed on the selected region in Figure 2b. Thanks to the simple spherical morphology of latex particles, we created two macros, used as a plugin in ImageJ, to segment the latex particles in the reconstructed result as spheres. 3D slicer was then used to model the 3D arrangement of the latex particles, as shown in Figure 3. There is only one layer of particles randomly dispersed on the carbon film.

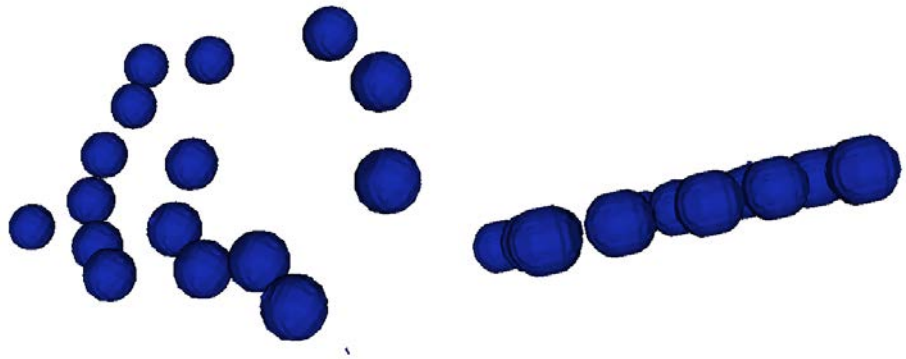

a) *b)*

Figure 3. 3D model of latex particles arrangement in the case of dilute latex suspension droplet deposited on the TEM grid, a) top view; b) side view

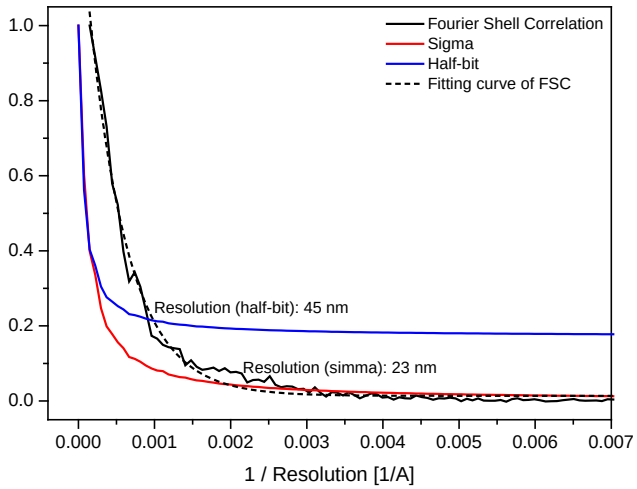

Figure 4. Results of the FSC analysis on dilute latex suspension, Resolution (half-bit criterion) ≈45 nm; Resolution (sigma criterion) ≈23 nm

Fourier Shell Correlation (FSC) *[G. Harauz & M. Van Heel, (1986)]* was used to determine the resolution in the tomogram by comparing the tomograms calculated from even and odd projections, see Figure 4. The curve can be considered to yield a meaningful result since it drops to zero at high frequencies. For a better calculation of the resolution, the FSC curve was smoothened. With the half-bit criterion, the FSC resolution (calculated from the intersection between the smoothened FSC curve and the half-bit curve) in the full tomogram is estimated to around 45 nm. When considering the sigma criterion, the FSC resolution (calculated from the intersection between the smoothened FSC curve and the sigma curve) is around 23 nm.

Both values are worse than the experimental probe size (8 nm) and the pixel size (6.8 nm). Generally speaking, the reconstruction process may result in an increase of noise and so worse resolution *[F. E. Boas & D. Fleischmann (2012)]*. Therefore, it can be considered that the resolution is not limited by microscopy capabilities, but by the tomography conditions such as 3D wet-STEM device, alignment and reconstruction of tilt image series.

5.1.2 Concentrated latex suspension

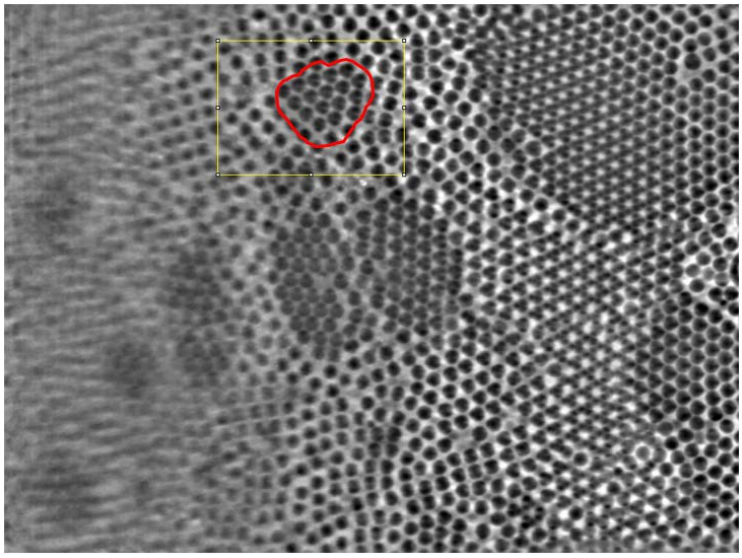

Figure 5. Tomogram calculated from the tilt series on a concentrated latex suspension: XY slice (the other slices have been presented in chapter 4, section 4.4). The yellow box (volume: $X \times Y \times Z$ = $2528 \times 1860 \times 1545$ nm^3) on the upper center of the image is the selected region for further analysis, and the red region is a hole in the carbon film covered by latex particles

The particles distribution in dilute suspension is a simple model and tomography experiments are not very useful in this case. On the contrary, the study of concentrated latex suspension is more meaningful in consideration of industrial applications. In chapter 4.4, a nice tomogram of concentrated latex suspension has already been presented. As it has been explained, the tilt series for 23 images was obtained in one hour, which gives a mean time per image equal to 156 s. Further segmentation was performed on the selected region shown in Figure 5. There is a hole (circled in red) covered by latex in the center of this selected region, which could be recognized according to its darker contrast. The latex particles on the carbon film are

surrounded by water, which appears bright. Due to the weaker ability of holding water on the hole than carbon film, there is less water surrounding latex particles on the hole, as a consequence, the particles are closer to each other in the hole than on the carbon film. The resulting 3D models are shown in Figure 6, under different views. From the top view (Figure 6a), the particles in the center arrange in well order and more closely than on the edge (that is on the carbon film). From the side view (Figure 6b), it can be clearly seen that the particles are in two layers. There is still some space between both layers, which could be attributed to the presence of water.

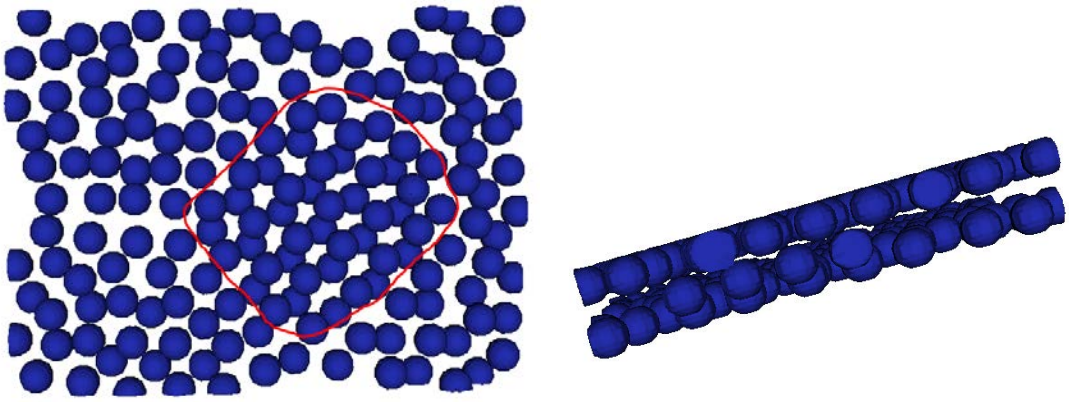

a) *b)*

Figure 6. 3D model of latex particles arrangement in the case of concentrated latex suspension droplet deposited on the TEM grid, a) top view(the well-order particles in a hole is marked in a red box); b) side view

The tomogram resolution analysis from FSC is shown in Figure 7, where the curve drops to zero at high frequencies. The smoothened FSC curve is used to calculate resolution on the basis of its intersection with either the half-bit curve or the sigma curve. With the half-bit criterion, the FSC resolution in the full tomogram is around 35 nm, while it is equal to 17 nm with the sigma criterion. Both values are again bigger than the experimental probe size (8 nm) and the pixel size (7.2 nm). This is similar to the result obtained on the dilute latex suspension, but slightly smaller, which may result from a better alignment result (residual error 0.8 pixel, smaller than 1.5 pixels in dilute suspension).

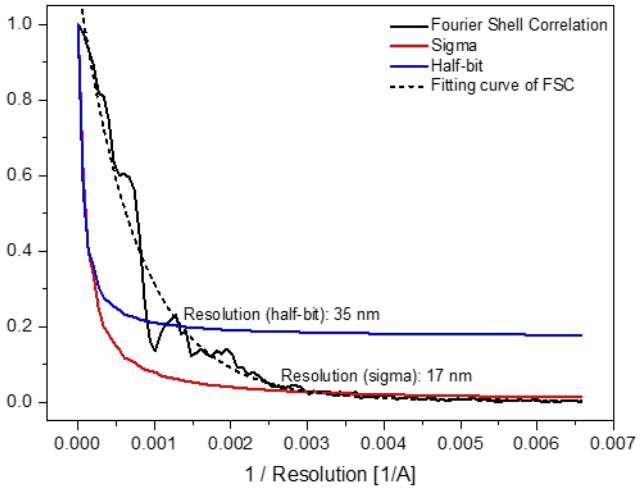

Figure 7. Results of the FSC analysis on concentrated latex suspension, Resolution (half-bit criterion) ≈35 nm; Resolution (sigma criterion) ≈17 nm

An even more concentrated latex suspension was further experimented to study the packing ability of latex particles, and the way this latex forms a film. A tilt image series (25 images) was obtained in 62 min (total acquisition time) at tilt angles ranging from +60° to -60° with a constant tilt step of 5°, so the average acquisition time for one image is 149 s.

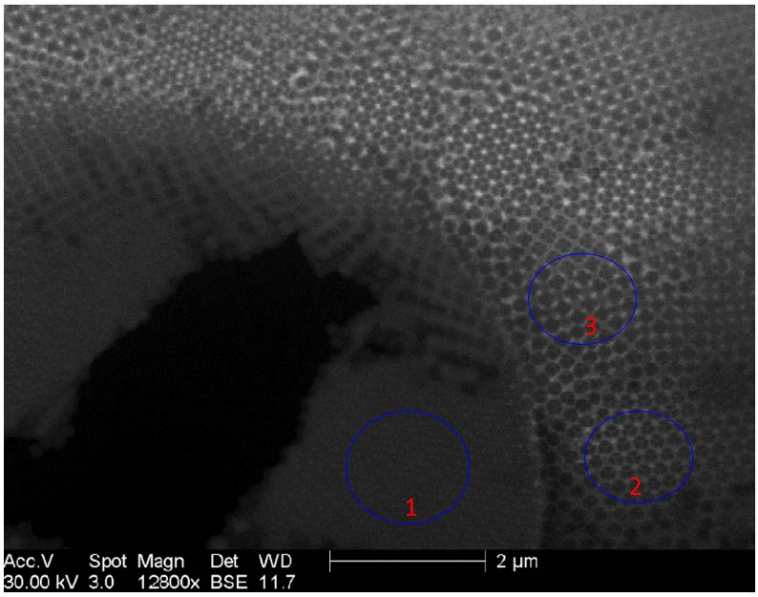

Figure 8. Acquired image at zero tilt of more concentrated PMMA-SBA latex suspension. Three representative regions: 1. dense latex on the hole; 2. honeycomb arrangement of particles on the carbon film; 3. cubic arrangement of particles on the carbon film

Figure 8 shows the image acquired at zero tilt, where two different parts can be found, a hole, and numerous fully connected particles. A quarter of the big hole (with a diameter around 12 microns) is at the bottom left of the image. Its center is fully black, which means that it is empty, without anything (water or latex particles). The other part of this hole (region 1 for instance) is grey, which suggests that no water is remaining among the close-packed latex particles. In the narrow area near the boundary between the hole and the carbon film, some bright water spots can still be noticed. Besides this big hole, the rest of this image corresponds to the carbon film fully covered by a dense packing of latex particles. In this region, the latex particles are surrounded by bright water but when analyzing the grey levels, it seems that the water thickness is lower than that in the case presented in chapter 4.4. Two types of arrangements are noticeable over the particles on the grid, region 2 and 3 with honeycomb and cubic arrangements, respectively.

This configuration is similar to the latex drying model shown in Figure 9. Water evaporates more rapidly from the boundary region than from the water surface above the wet dispersion, thus creating a kind of slight water flux and particle movement from the wet portion to the edge *[N. D. Denkov et al. (1992)]*. As drying proceeds, the dry edge grows in size and the wet dispersion contracts in area. Voids remain at the dry side of the boundary *[J. G. Sheehan et al. (1993)]*, *[J. L. Keddie et al. (1995)]*. The time scale for full densification of the dry film can be hours or days *[M. A. Winnik. (1997)]*. Although close-packed latex particles are held by the hydrophilic carbon film, the dry edge may still accelerate water evaporation from the carbon film, which may cause artifacts in the tomogram.

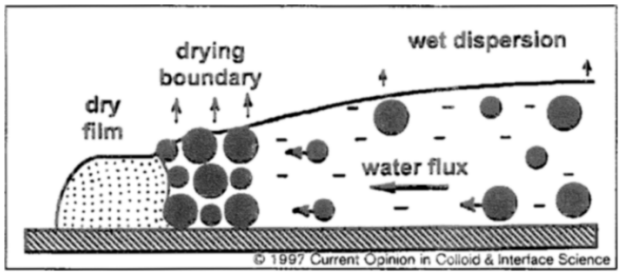

Figure 9. Representation of the drying model for a latex dispersion, the dry film at the edge is separated from the wet dispersion by a transition or boundary region [M. A. Winnik. (1997)]

The latex particles are initially spherical, as seen in the dilute case (Figure 1). Interestingly, from the 2D image at zero tilt in Figure 8, there are other three kinds of latex particles when considering their shape and distribution, as circled in three regions. On the hole, the interfaces have disappeared and the latex film seems to be quite homogeneous (as region 1). Between these two states, when the particles are brought close enough to each other, they can form specific structures, either by aggregating in some way or by staying a little way apart, as in region 2 or 3 on the carbon film. A similar behavior can be observed in the cryo-SEM image shown in Figure 10. These structures can be explained by the film formation process in Figure 11. As water continuously evaporating and the suspension concentrating during film formation, the movement of particles inside a very thin water film may be limited by the adhesive force from carbon film. Therefore the different regions with different latex concentrations on the TEM grid can be considered as different stages of the process of film formation. Even on the same image, the particles density may however vary, perhaps due to differences in hydrophily between the carbon film and the hole.

In the model shown in Figure 11, the latex particles contain a surfactant which covers the particle surface forming a swollen hydrophilic layer (Figure 11a). Several groups of particles can gather together, while there are still some particles separated from these groups. From the top view, this refers to region 1 in the cryo-SEM image (Figure 10). When the dispersion concentration increases, the particles become closely packed and deform themselves (Figure 11b), as can be observed in chapter 4.4. When increasing further the latex concentration, water is expelled from the interstitial voids (Figure 11c) and polyhedral cells are formed, divided by hydrophilic layers of surfactant (membranes) *[A. du Chesne et al. (1997)]*. Though broadly accepted, the model is partially misleading, as some experiments have shown that particle deformation to polyhedral cells may take place prior to close packing *[T. Crowley et al. (1992)]*, *[M. A. Winnik & J. Feng (1996)]*. Therefore the particles may be considered as intermediate states between sphere and polyhedral cells. This could be the case of region 2 in Figure 10 and region 2 in Figure 8 as well, where the difference might come from two observation models, SEM and STEM. Besides, a well-ordered structure as cubic cells is observed in both Figure 8 and Figure 10 (region 3). Particles are very concentrated in both cases, and their movements are not free as in water, but limited by the adhesive force from

carbon film (Figure 8), or by rapid freezing (Figure 10). When particles gather and get close-packed, the nearby particles are dragged by attractive forces from two or more close-packed regions, and finally form a special structure with particles a little way apart due to the space left by those aggregated particles. The coalescence of dry particles on the hole (like region 3 in Figure 8) results from the collapse of surfactant membranes after further dehydration, as illustrated in Figure 11d.

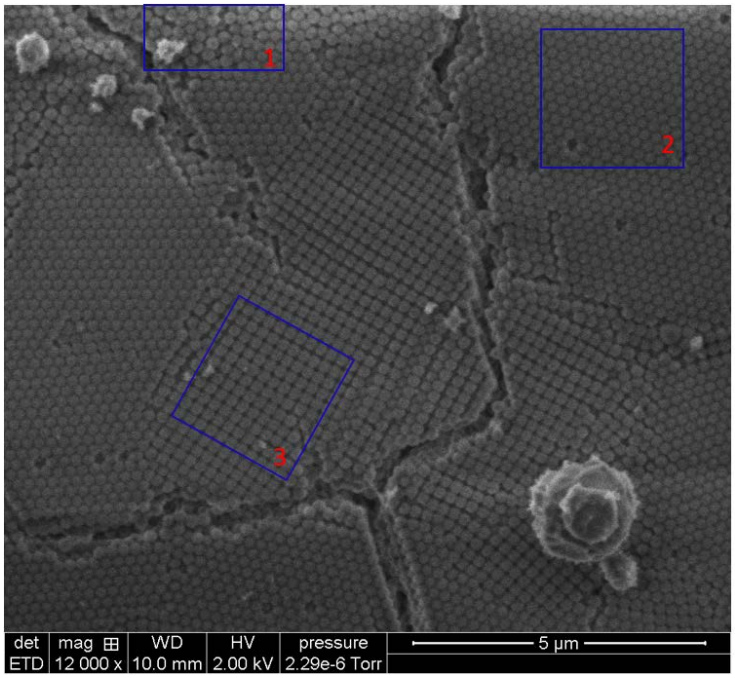

Figure 10. Image of undiluted latex suspension from cryo-experiments in SEM

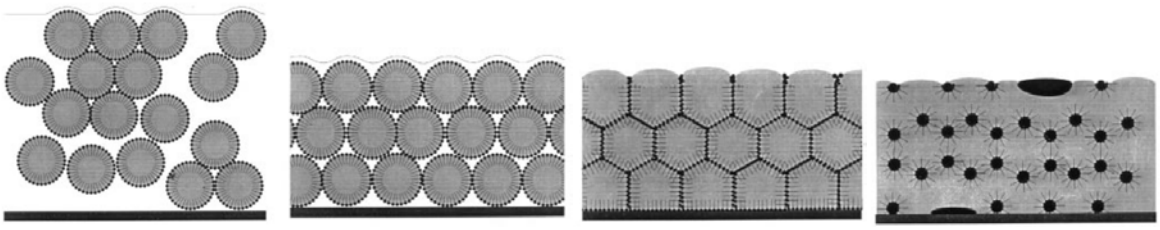

a) *b)* *c)* *d)*

Figure 11. Schematic representation of the process of film formation from latex dispersion arbitrarily divided into four steps: a) dispersion ; b) latex particles form a close packing; c) latex particles deform in order to fill the volume and expel water; d) the surfactant membrane disrupts and coalescence occurs. The surfactant is drawn as a dash line, with black dots symbolising the hydrophilic end-group. The polymer is shown by grey shading [A. du Chesne et al. (1997)]

Besides the characterization on the surface, tomography further offers information on the 3D structure. Before reconstruction, patch tracking is used to make a fiducial model for the alignment of the tilt images with Etomo. Similarly to what was obtained in the alignment presented in chapter 4.4, the number of trackings equals 850. The residual error is 1.4 pixels, which may partly result from the processes involved in the acquisition of tilt series, caused by factors such as movements of particles or region of interest. The tomogram is obtained after aligning the projections. It is shown in Figure 9. Some artifacts can be found. Apart from "missing wedge" artifacts *[P. A. Midgley & M. Weyland, (2003)]*, the fanning and elongation effects are possibly caused by the error in the alignment, or by irradiation damage. Segmentation using the spherical particle model avoids the fanning and elongation effects in the 3D models.

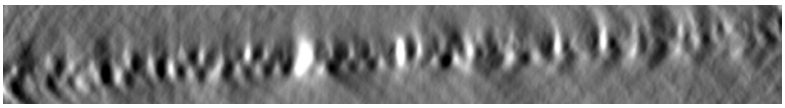

a)

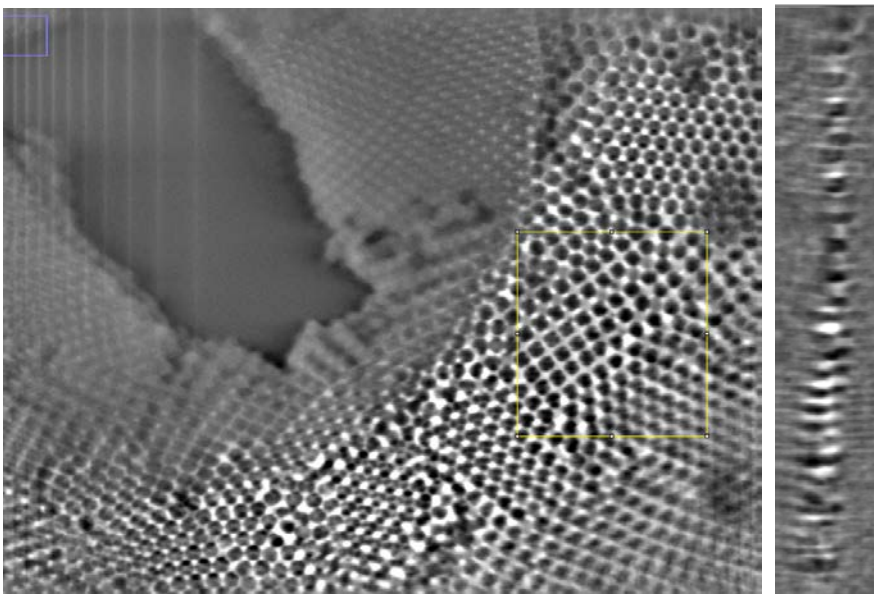

b) *c)*

Figure 12. Tomogram calculated from the tilt series of a dense latex suspension, the volume: X×Y×Z = 9488×7163×3000 nm^3. a) YZ slices, b) XY slices and c) XZ slices. The yellow box (volume: X×Y×Z = 2220×2430×1560 nm^3) on the right of the image is the selected region for further analysis

Although specific structures (polyhedrons or cubes) are formed as discussed above, latex particles are considered as spheres in order to simplify the analysis of their spatial arrangement. As seen from the 3D model in Figure 13, a left region is composed of two layers of well-ordered particles. The spacing between both layers is much lower than in Figure 6b, which means a lower amount of water and a higher density of latex particles. This layered structure is similar to that observed on the undiluted latex suspension by cryo-SEM, and is accordance with the model in Figure 11b or 11c.

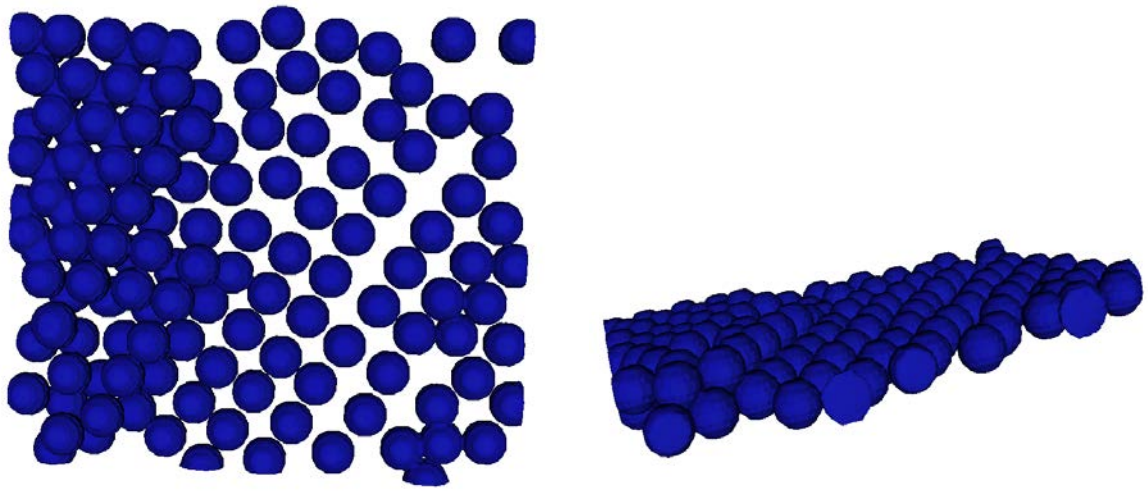

a) *b)*

Figure 13. 3D model of latex particle arrangement in the case of a concentrated latex suspension droplet deposited on the TEM grid, a) top view; b) side view

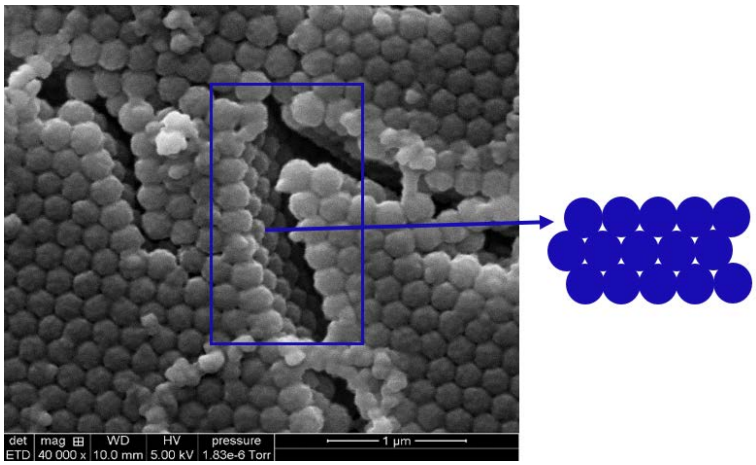

Figure 14. Image of undiluted latex suspension from cryo-experiments in SEM

The FSC resolution analysis is shown in Figure 15. The curve drops to zero at high frequencies, and is fitted to a smooth curve. With the FSC half-bit or sigma criterion, the full tomogram FSC resolution is respectively around 62 nm or 31 nm, much more than the experimental probe size (8 nm) and the pixel size (7.2 nm), and the calculated FSC resolution of the other two tomograms discussed above. The poor resolution is most probably because of vibrations arising from water evaporation, leading to noise in the images, and error in the alignment as well (with residual error 1.4 pixels).

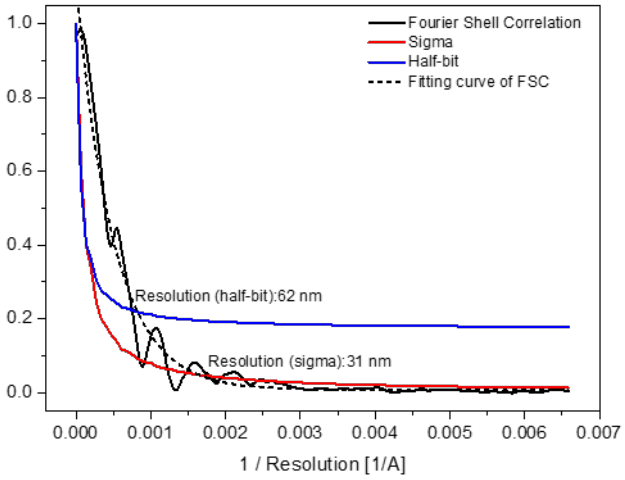

Figure 15. Results of the FSC analysis on a concentrated latex suspension, Resolution (half-bit criterion) ≈ 62 nm; Resolution (sigma criterion) ≈ 31 nm

As a conclusion, all the calculated FSC resolution values in full tomogram of three latex suspension with different concentrations are not ideal, higher than both the experimental probe size and the images pixel size. This may mean imperfection during the process of series acquisition or data treating. Nevertheless, the tomography results successfully provide the spatial structure information, Table 1 gives a summary of the tomography on these three suspension. The structure of concentrated latex suspension well corresponds to that in the images acquired with cryo-SEM and literature. Therefore, tomography performed with STEM mode in ESEM can be considered as fully representative of the bulk.

Table 1. Summary of tomography on latex suspension with different concentration

Sample (latex suspension)	Dilute	Concentrated	Dense
Numbers of tilt images	25	23	25
Mean ac. time per image *(s)*	168	156	149
Alignment residual error *(pixel)*	1.5	0.8	1.4
FSC Resolution *(nm)*	Half-bit criterion:45 Sigma criterion: 23	Half-bit criterion:35 Sigma criterion: 17	Half-bit criterion:62 Sigma criterion: 31
Analyzed volume X×Y×Z *(nm^3)*	2180×1380×1020	2528×1860×1545	2220×2430×1560
Particles arrangements	Single (mainly) or several gathered particles dispersed in one layer	Tightly arranged particles gathered in two layers (still some space between layers)	Particles tightly gathered in two well-order structures and in honeycomb between layers

5.2 Tomography on a suspension containing latex and surfactant

The type of surfactant plays an important role on the latex particles distribution, in particular during the process of film formation. Membranes (described in Figure 11) built up from low molecular weight ionic surfactant generally collapse quickly. While higher molecular weight or non-ionic membranes could keep the structure for a longer time. Especially, when such surfactant is in large excess, or when the surfactant is grafted to the polymer, membranes will be better maintained at the boundary between the particles and may prevent their coalescence *[K. W. Evanson & M. W. Urban (1991)]*, *[Y. Chevalier et al. (1992)]*. In our SBA latex

suspension, 3% PMMA has already been grafted as a steric surfactant, but cracking has been observed in the ESEM images. Hence, latex suspensions are now further studied, a second surfactant (XPCAS 803) is added. This surfactant is widely used in the industry, it exhibits a high molecular weight, long ramified structure and combines three steric and ionic functional groups to help the dispersion of fillers, reinforce and additives involved in material formulation.

Patch tracking has been used to make a fiducial model for the alignment of the tilt images in the tomography of two concentrated latex suspension discussed above. But high residual error occurs in the case of imperfect acquisition, such as unwished movements of sample or 3D stage during tilting process, or man-made errors when obtaining the images (may leading to images not exactly the same region of interest at different tilts). Bad alignment may result in artifacts in volume construction and thus low tomogram resolution. Gold nanoparticles could also be reconsidered as fiducial markers, as in the tomography of PU. Taking into overall consideration the roles of gold nanoparticles as both fiducial markers for a lower residual error in alignment and as focus-helper for the latex particles with diameter of 200 nm, the gold nanoparticles should be neither too small nor too big. After comparison of several sizes of gold nanoparticles, those with a diameter around 40 nm, the same as in Chapter 2, are chosen as markers.

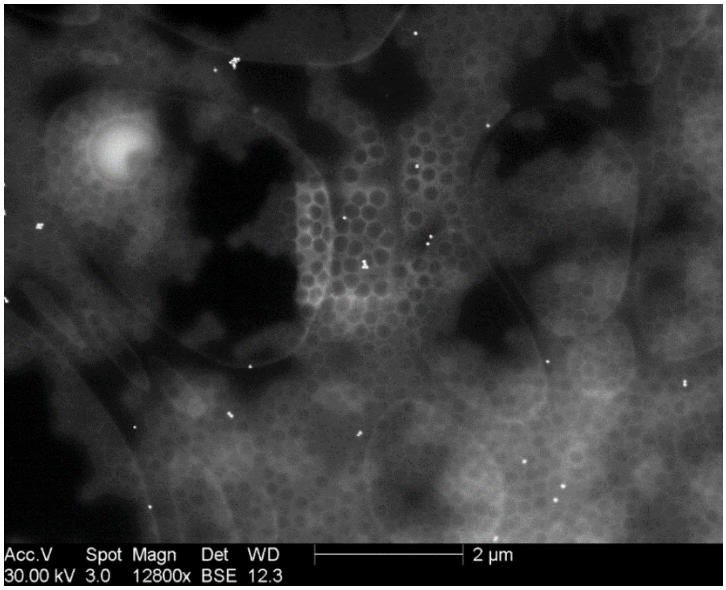

Figure 16. Acquired image at zero tilt of latex suspension with surfactant XPCAS 803

A tilt series over an angular range from 45° to -65° with projections taken every 5° has been obtained. The total acquisition time of 23 images is 60 min, making the mean acquisition time of one image about 155s. As we can see from the image at zero tilt in Figure 16, the randomly dispersed gold nanoparticles are very bright, as expected. They are nicely isolated, although a few ones are gathered together. The dark latex particles exhibit a bright shell which can be attributed to the surfactant XPCAS 803. The latex particles surrounded by the surfactant are dispersed in a water film. The center of this image is brighter, with a more pronounced contrast, which is most probably the consequence of irradiation damage after scanning in a small window. The black area, mainly on the holes, is empty without any latex or water coverage.

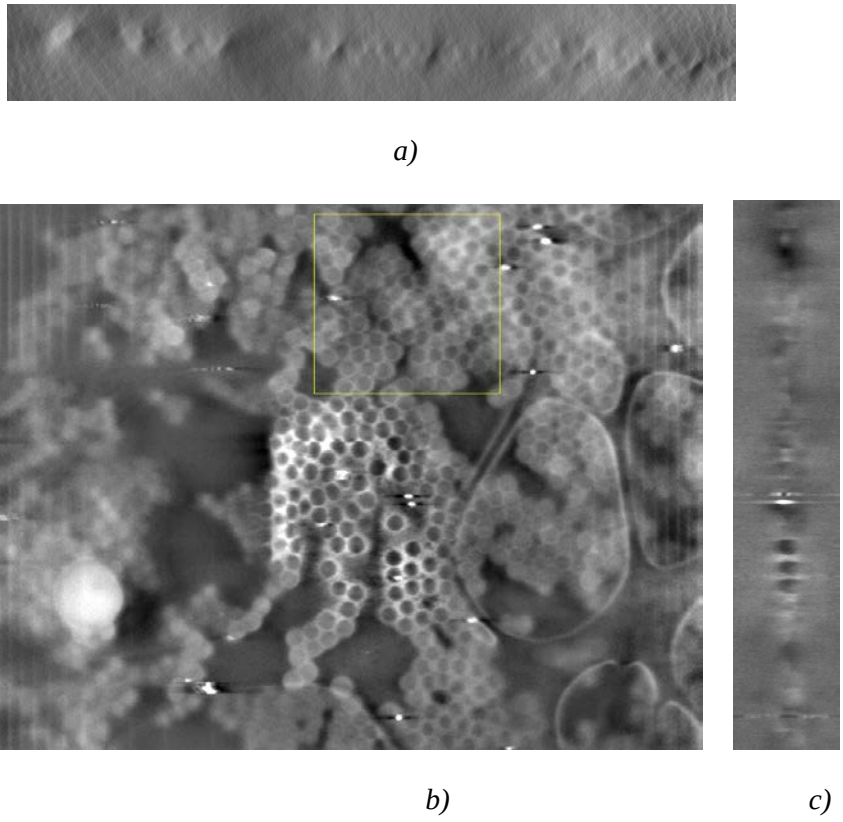

a)

b) *c)*

Figure 17. Tomogram calculated from the tilt series of latex suspension with surfactant XPCAS 803, the volume: X×Y×Z = 9593×7133×3000 nm^3. a) YZ slices, b) XY slices and c) XZ slices. The yellow box (volume: X×Y×Z = 2400×2325×1395 nm^3) on the upper center of the image is the selected region for further analysis

After the acquisition of tilt images, 19 gold nanoparticles are chosen as fiducial makers for alignment. The residual error is around 0.6 pixel, much better than the alignment for

aforementioned latex suspension. This can be attributed to the fact that we used gold nanoparticles as fiducial markers. Then the reconstruction is performed with a 15 iteration step ART algorithm.

As can be found from Figure 17, a tomogram is obtained with a nice latex distribution even though elongation effects are visible, which may be caused by missing wedge. The region chosen for segmentation and for further 3D models is shown in Figure 17. It does not include the irradiation damage area and contains no hole. The obtained core-shell model of latex-surfactant is represented in Figure 18. The surfactant thickness is 15 nm. Moreover, one part of this region contains only one layer of particles in a non-compact arrangement, whereas the other part is made of two layers of particles close to each other. The particles arrangement between two layers is similar to the concentrated latex suspension without surfactant XPCAS 803, and corresponds to the model in Figure 11.

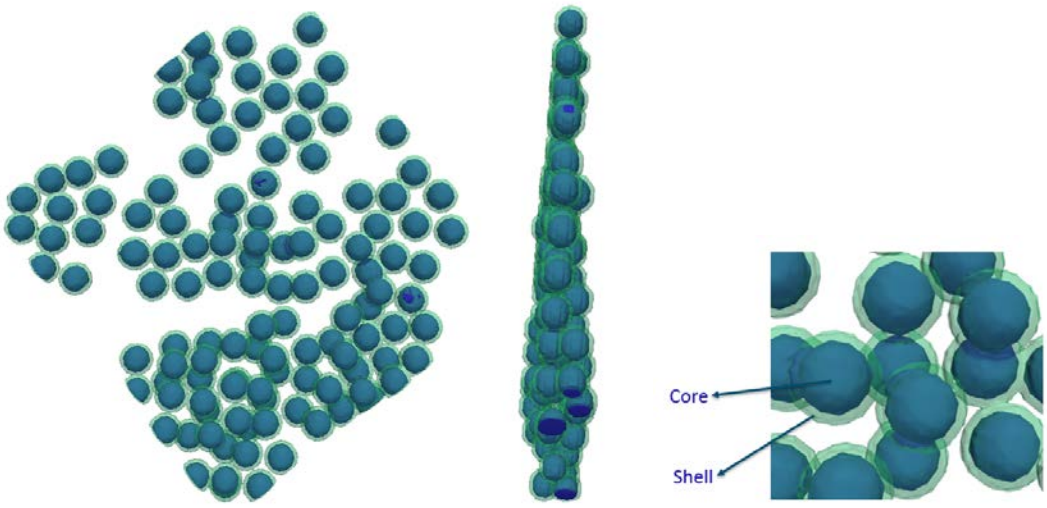

a) *b)* *c)*

Figure 18. 3D model of latex particles arrangement in the case of latex with surfactant XPCAS 803. a) top view; b) side view c) zooming in a small region of top view (blue core: latex particles; green shell: surfactant XPCAS 803)

The full tomogram resolution is studied with FSC analysis as well, see Figure 19. The Fourier Shell Correction curve drops to zero at high frequencies, and is fitted to a smooth curve as

well. The FSC halt-bit resolution calculated from the intersection is 50 nm, and 26 nm for sigma resolution, while the experimental probe size 8 nm and the pixel size 7.2 nm. In consideration of the surfactant thickness 15 nm, it is concluded that this calculated FSC resolution in the full tomogram is unpersuasive. It is possible that the noise results from the center area with irradiation damage or too many holes in which there are possible particles or water movements. Nevertheless, it can be concluded that the resolution of our home-made 3D device with this suspension is at least equal to 15 nm.

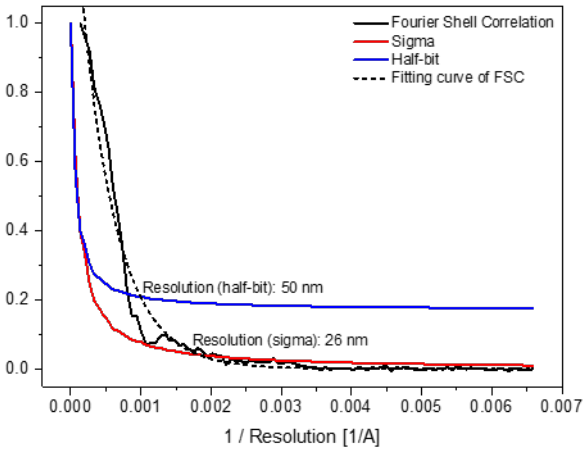

Figure 19. Results of the FSC analysis on latex with surfactant XPCAS 803, Resolution (half-bit criterion) ≈ 50 nm, Resolution (sigma criterion) ≈ 26 nm

5.3 Influence from irradiation damage

Irradiation damage is a usual problem in electron microscopy. In particular, organic materials and water are especially susceptible to the effects of radiation damage imaged in ESEM. There are two main reasons: no coating is used to protect samples from the electron beam and evacuate the charges in excess; the presence of water vapor as an imaging gas increases the formation of free radicals, known to be a major cause of radiation damage *[D. J. Stokes (2008)]*. Indeed, water vapor can be dissociated by the beam while absorbed, which may result in oxidation and some material losses. While considering liquid samples, the chemical transformations induced by radiation are much more serious than considering solid ones.

The most striking influence during the acquisition of images on latex suspensions is the changes in contrast, which has been discussed in chapter 3 and combined with the Monte Carlo simulation results. In each tilt series, contrast changes can be observed between the first projection and the last one. A more serious influence is the appearance of bubbles. In the experiment shown in Figure 20, after having acquired 20 images on the same region of interest, two bright dots appeared. The big dot fractures when decreasing the chamber pressure, as can be seen from Figure 20d and 20e, and may be considered as bubbles. Bubbles have also been observed in liquid cell used in TEM *[J. M. Grogan et al. (2012)]*, *[J. M. Grogan et al. (2014)]*. However, they are attributed to H_2 release. It could be the case here but the presence of a residual membrane suggests the presence of a polymer film which formation remains unexplained. Fortunately in ESEM, this phenomenon is quite rare and all the tomograms presented above do not contain any bubble.

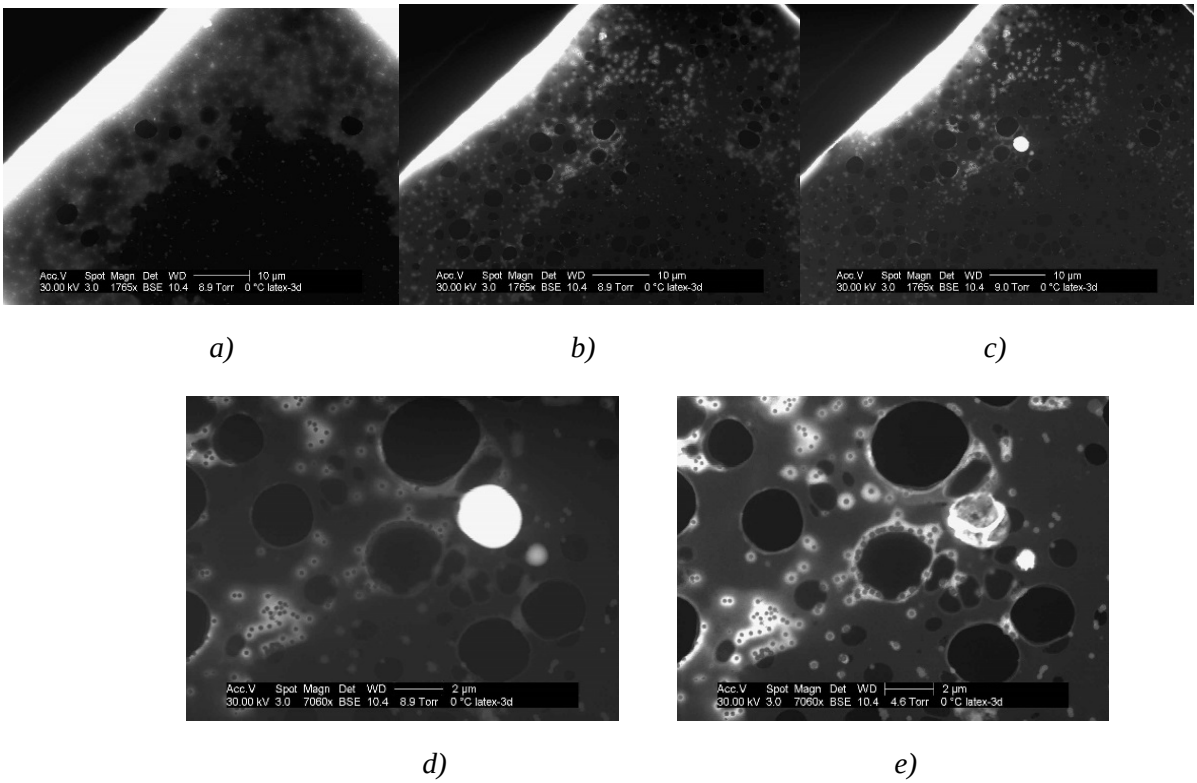

Figure 20. Changes in a latex suspension images during scanning : a) first scan; b) second scan; c) after 20 scans; d) zoom of image c); e) same area after drying

Damage effects can be reduced by minimizing the exposure time and the cumulated dose. For tomography, a series of images at different tilt angles needs to be obtained. In our experiments, the tilt series have usually been acquired in one hour, with an angular range of 60° and a constant tilt step of 5. This is considered as a good compromise between a good-quality reconstruction and the minimization of radiation artifacts. In addition, focus, astigmatism, wobblers, contrast and brightness readjustments are done not directly on the region of interest but in a nearby region on the tilt axis, the beam then being moved on the region of interest just for the acquisition. This procedure prevents beam damage on the area prior to the image acquisition, thus largely shortens the dwell time. Even so, the influence of irradiation damage can still not be avoided effectively. Damage from electron beam on liquid materials is a complicated problem, and reducing irradiation damage is still challenging and should be studied in the future.

5.4 Conclusions

In this chapter, tomography experiments have been performed on liquid nano-samples with our optimized home-made 3D device in ESEM. Firstly, series of tilt images have been obtained on latex SBA-PMMA from a dilute suspension to a very concentrated one. After reconstruction, segmentation has been performed by considering latex particles as perfect spheres on several selected regions. The obtained 3D models have revealed the spatial arrangement of latex particles. The structure of concentrated latex suspension corresponds to that in the images acquired with cryo-SEM and therefore electron tomography in ESEM can be considered as fully representative of the bulk. Resolution has been calculated for each tomogram from the intersection between the FSC curve and the half-bit curve/sigma curve. The values obtained are very dependent on several parameters among which the alignment residual error.

A further study has then been carried out in presence of a high molecular weight surfactant - XPCAS 803 - which combines two hydrophobic groups and a hydrophilic one, as steric and ionic functional groups. A gold nanoparticle (diameter around 40 nm) suspension was used to help finding the focus in the images and aligning the tilt series. The reconstruction has been

performed with a well aligned tilt series, and a selected region has been segmented and modeled. The 3D models clearly showed the core-shell structure and spatial arrangement of latex-XPCAS 803. The FSC resolution with half-bit and sigma criterion has been calculated respectively as equal to 50 nm and 26 nm in the full tomogram. However, it can reasonably been considered that the resolution is at least equal to the surfactant shell thickness, 15 nm.

Finally, the influence of the electron beam on latex suspension images has been discussed. Although some efforts have been made to minimizing the irradiation damage during the acquisition of tilt series, it is still a challenging work in the future.

References

A. du Chesne, B. Gerharz & G. Lieser. The Segregation of Surfactant upon Film Formation of Latex Dispersions: an Investigation by Energy Filtering Transmission Electron Microscopy. Polymer International 43, (1997), 187-196

D. J. Stokes. Principles and practice of variable pressure: environmental scanning electron microscopy (VP-ESEM). (2008)

F. E. Boas & D. Fleischmann. CT artifacts: Causes and reduction techniques. Imaging Med. 4, (2012), 229-240

G. Harauz & M. Van Heel. Exact filters for general geometry three dimensional reconstruction. Optik 73, (1986), 146–156

J. G. Sheehan, K. Takamura, H. T. Davis, L. E. Scriven. Microstructure development in particulate coatings examined with cryogenic scanning electron microscopy. Tappi J 76, (1993), 93-101

J. L. Keddie, P. Meredith, R. A. L. Jones, A. M. Donald: Kinetics of film formation in acrylic latices studied with multiple-angle-of-incidence ellipsometry and environmental SEM. Macromolecules 28, (1995), 2673-2682

J. M. Grogan, N. M. Schneider, F. M. Ross, H. H. Bau. The Nanoaquarium: a New Paradigm in Electron Microscopy. J. Indian Inst. Sci. 92, (2012), 295−308.

J. M. Grogan, N. M. Schneider, F. M. Ross, H. H. Bau. Bubble and Pattern Formation in Liquid Induced by an Electron Beam. Nano Lett. 14, (2014), 359−364

K. W. Evanson & M. W. Urban. Surface and interfacial FTIR spectroscopic studies of latexes. I. Surfactant–copolymer interactions J. Appl. Polym. Sci. 42, (1991), 2308

M. A. Winnik & J. Feng. Latex blends: an approach to zero VOC coatings. J. Coatings Technology 68, (1996), 39

M. A. Winnik. Latex film formation. Current Opinion in Colloid & Interface Science 2, (1997), 192-199

N. D. Denkov, O. D. Velev, P. A. Kralchevsky, I. B. Ivanov, H. Yoshimura, K. Nagayama. Mechanism of formation of two-dimensional crystals from latex particles on substrates. Langmuir 8, (1992), 3183-3190

P. A. Midgley & M. Weyland. 3D electron microscopy in the physical sciences: The development of Z-contrast and EFTEM tomography. Ultramicroscopy 96, (2003), 413–431

T. Crowley, A. R. Sanderson, J. D. Morrison, M. D. Barry, A. J. Morton-Jones, & A. R. Rennie Formation of bilayers and plateau borders during the drying of film-forming latices as investigated by small-angle neutron scattering. Langmuir 8, (1992), 2110

Y. Chevalier, C. Pichot, C. Graillat, M. Joanicot, K. Wong, J. Maquet, P. Lindner & B. Cabane. Film formation with latex particles. Colloid Polym. Sci. 270, (1992), 806

Conclusions

The aim of this PhD was to develop electron tomography on hydrated samples with nanometer resolution. After a review of different microscopies using on the observation of liquid materials, several tomographic techniques with different resolution abilities were introduced in chapter 1. In light of this review, we focused on the 3D characterization of liquid suspensions using wet-STEM in ESEM. This technique indeed gives a good contrast even on thick samples, and the large ESEM chamber is convenient for the use of a rotating stage. Moreover, as the temperature of the sample and the water pressure can be adjusted during the experiment, water can be evaporated *in situ* and changes in the 3D structure might be followed.

Chapter 2 firstly gave details of the selected model nano-materials used in this work: a latex SBA-PMMA suspension eventually with a high molecular weight surfactant, a gold nanoparticles suspension, and PU-carbon nanotubes nanocomposites. The first two are liquid with spherical particles, the last one is solid film with nanotubes. Then, the 2D analysis methods used were introduced, namely wet-STEM and GSED mode in ESEM, cryo-SEM, as well as Monte Carlo simulations. In the end, our home-made 3D device using wet-STEM mode in ESEM was presented, as well as the methods used for 3D data processing.

The relationships between contrast and water film thickness was studied in chapter 3. Firstly two different types of model suspensions, gold nanoparticles and SBA-PMMA latex particles, were thoroughly studied by comparing ESEM images with some Monte Carlo simulations. With gold nanoparticles, the contrast between the nanoparticles and water changes with the water thickness and the position respective to the water top surface. A contrast inversion occurs when the thickness of water film is around 1.4 µm. Therefore, the water film thickness could be measured when contrast inversion occurred, but it is not possible to give a refined estimation below and above this point. Fortunately, it is possible to provide a more precise estimation of the water film thickness thanks to the core-shell structure of SBA-PMMA latex particles, by comparing the simulated and experimental grey level profiles. A further study on twelve kinds of nanoparticles was also performed using some Monte Carlo simulations. For each one, a value of resolution was assessed by determining the minimum size of a particle

for which the contrast was at least equal to 5% (for a given water film thickness). The result indicated that the resolution mainly depends on the water thickness. Hence, Monte Carlo simulation helps to better understand the behavior of nano-materials within a liquid phase, which provides useful information for 3D characterization of liquid materials.

Chapter 4 first presented the tomography results obtained on our pre-existing home-made 3D stage. A satisfying result of volume reconstruction and segmentation was obtained with projection series obtained on dry polyurethane films containing ungrafted or grafted carbon multiwalled nanotubes. On the contrary on a latex SBA-PMMA suspension, a bad tomogram was obtained mainly as a consequence of severe water evaporation during the acquisition of tilt images. Therefore, an improvement of the 3D device was needed to achieve a highly refine control of the sample temperature. In our 3D device, the design of the sample holder was changed, with better heat-conduction materials and structure. With this new tip, the sample temperature could be measured more accurately and was found to be closer to the target temperature. Besides, some other experimental conditions have been optimized as well, like proper settings of Peltier stage. With these new conditions and stage, a series of images on a region with two layers SBA-PMMA nanoparticles was obtained and the volume could efficiently be reconstructed in spite of probable irradiation damage. Therefore, we showed that it was possible with our home-made 3D device used in ESEM to perform a 3D characterization not only on dry materials but also on aqueous suspensions of nanoparticles.

In chapter 5, we presented several tomography experiments carried out on liquid nano-samples with our optimized home-made 3D device in ESEM. Firstly, series of tilt images were acquired on latex SBA-PMMA from a dilute suspension to a very concentrated one. After reconstruction, segmentation was performed by considering latex particles as perfect spheres on several selected regions, then the spatial arrangement of latex particles was revealed by obtained 3D models. The structure of a concentrated latex suspension is in good agreement with that deduced from cryo-SEM images. The resolution was calculated for each tomogram from the intersection between the FSC curve and the half-bit curve or sigma curve and the value was found to depend on several experimental parameters. A further study was then carried out in presence of surfactant XPCAS 803. In this case, gold nanoparticles (diameter around 40 nm) were used to help finding the focus in the images and aligning the tilt series. A

selected region in the obtained tomogram was segmented and modeled, revealing the core-shell structure and spatial arrangement of SBA-PMMA latex with XPCAS 803. The resolution was calculated to be equal to 50 nm and 26 nm in the full tomogram with the half-bit FSC criterion and sigma criterion, respectively. However, it can reasonably been considered that the resolution is at least equal to the thickness of the surfactant shell, 15 nm. Finally, the influence of the electron beam on the images and the efforts to minimize the irradiation damage were discussed.

Perspectives

In this work, we developed electron tomography on liquid suspensions using STEM-in-ESEM. The successful results led to the conclusion that electron tomography in ESEM can be considered as fully representative of the bulk. From its resolution and field of view, it is fully complementary to existing tomography techniques. Nevertheless, there are still some works needing to be considered in the future.

Firstly, ESEM tomography may be further performed on some complicated liquid nanomaterials. In this PhD work, we used only nanoparticles with a spherical structure. They were easy to segment and model in spite of the artifacts in the tomogram. Thus, in terms of samples with asymmetric complicated structures, our 3D device used in ESEM needs to be further evaluated.

Secondly, more attention should be paid to the influence of the electron beam during the observation of liquid materials. At the end of chapter 5, a brief discussion was given on this topic and efforts have been made to minimize irradiation damage during tilt series acquisition. However, the detailed irradiation processes and results are complicated. Simulations have been carried out to explain irradiation damage when using liquid cells in TEM. The concentration of radiolysis products, and the effects of irradiation such as pH of solution, aggregation of nanoparticles, formation of bubbles have been detailed and discussed *[N. M. Schneider[1] et al. (2014)] [N. M. Schneider[2] et al. (2014)]*. Wet-STEM in ESEM differs from the use of liquid cells in TEM by the energy of the electron beam. Moreover, a dynamic water liquid/vapor equilibrium is kept thanks to the gas pressure and sample temperature, which is not the case in the closed environment in the sealed liquid cell. As a consequence, the electron beam influence in ESEM may be different and so needs future study.

TEM imaging on latex suspensions in sealed liquid cells could be still be used to draw a comparison with STEM-in-ESEM. In chapter 5, the structure of latex nanoparticles acquired from images in STEM-in-ESEM showed a good agreement with that from cryo-SEM. The comparison with TEM, the predominant analysis technique on liquid materials, may be

interesting. In particular, it would be interesting to compare the contrasts between the different phases (water, latex particles, surfactant). Irradiation damage could also be compared.

References

N. M. Schneider[1], M. M. Norton, B. J. Mendel, J. M. Grogan, F. M. Ross, and H. H. Bau. Radiolysis during Liquid Cell Electron Microscopy**.** Microsc. Microanal. 20, (2014), 1516-1517

N. M. Schneider[2], M. M. Norton, B. J. Mendel, J. M. Grogan, F. M. Ross, and H. H. Bau. Electron-Water Interactions and Implications for Liquid Cell Electron Microscopy. J. Phys. Chem. C 118, (2014), 22373-22382